ARO 15284.1-MS

B.S.

12

ARPA Order No. 3397

LEVEL II

Contract No. DAAG29-77-C-0028

AD A061951

6 RAPID CYCLE CASTING OF STEEL.

12 222p.

10 Principal Investigators: Drs. Diran Apelian and George Langford
(215) 895-2327 (215) 895-2330

Contractor: Drexel University, Philadelphia, PA 19104

9 Rept. for 1 Jul 77-30 Jun 78

11 30 Jun 78

Reporting Period:

Effective date of Contract: 1 July 1, 1977

Contract expiration date: December 31, 1979

DDC RECEIVED DEC 8 1978 A

18 ARO

19 15284.1-MS

7 per other reports

DISTRIBUTION STATEMENT A
Approved for public release;
Distribution Unlimited

Sponsored by

Defense Advanced Research Projects Agency (DoD)

ARPA order No. 3397

15 Monitored by Dr. Phillip Parrish under Contract No. DAAG29-77-C-0028, new ARPA Order-3397

The views and conclusions contained in this document are those of the authors and should not be interpreted as necessarily representing the official policies, either expressed or implied, of the Defense Advanced Research Projects Agency or the U. S. Government.

DDC FILE COPY

78 11 13 062

405 723 mt

RAPID CYCLE STEEL CASTING, FIRST PROGRESS REPORT

SUMMARY

We are developing a rapid-cycle casting process for steel. Solidification takes place by carbon redistribution between iron-saturated high-carbon liquid iron and low carbon pre-existing solid iron in a refractory mold. That is, a mold is first filled with steel shot, heated, and then quickly infiltrated with molten cast iron at its liquidus temperature. Since no heat need be rejected to the surroundings during this diffusion solidification (SD) process, the solidification time is shorter and the economic scaling law is less dependent on the size of the casting than in conventional casting processes; i.e. $t_{SD} \alpha L^{6/5}$ instead of L^2. Furthermore, no riser is necessary because of the large fraction (60% or more) of pre-existing solid, and shrinkage porosity can be controlled by lowering the total oxygen content of the casting components. There is little or no thermal shock to the mold because the process is essentially isothermal and the casting temperature is reduced by 150 to 200°C. Hence, it may be possible to achieve production rates for steel casting analogous to die casting but without the material problems normally associated with the high melting point of steel.

During the first contract year we have concentrated on those parameters which control process economics: attainable heating rates and efficiencies, liquid and solid metal handling and purification, and mold preparation. We have established two techniques for uniformly heating the shot-filled mold to process temperatures without interface or size-controlled heat transfer. These are low frequency electrical induction heating and forced, inert gas infiltration. Heating efficiencies are 15% and 40%, respectively. We have shown that a coarse bed of non-wetting refractory particles can dependably and predictably isolate and support a metallostatic head of low to high carbon liquid iron, and yet quickly let that liquid pass through when necessary. This "particle valve"

78 11 13 062

greatly simplifies the liquid-cast iron infiltration on which SD casting depends and also simplifies our bottom-pour atomization furnace for making the controlled-quality spheroidal low carbon steel shot. We have completed the construction of the necessary experimental SD casting and atomization furnaces and have proven their utility. We have also constructed a decarburization/deoxidation apparatus for treatment of commercially available steel shot, so that a wide range of shot quality and composition is now attainable at Drexel University.

In the second contract year we will evaluate and develop glazed investment (nonrecyclable, non permanent) molds in order to gain control of their permeabilities to deoxidation products and the melt-transfer pressurization gas. We will begin studies of techniques of making vacuum process (recyclable) molds and permanent molds. We will determine the strength of SD castings as a function of the fraction of remaining liquid by high temperature in situ tensile tests to determine the process cycle rate limiting solidification time. We will measure the rate of liquid metal infiltration during SD casting. We will begin an experimental program to determine the metallurgical advantages and structure sensitivities to the parameters of this unique casting process. We will make representative castings of the important alloys to which the SD process can be applied: ultra high carbon high speed steel, high carbon die steel, high strength low alloy steel, and aluminum-lithium, which is the most promising candidate system among nonferrous substitutional alloys.

TABLE OF CONTENTS

		Page
I.	Introduction	1
II.	Heating Methods in Manufacturing diffusion solidified steel Castings - Task 1	5
III.	Performance and operating characteristics of the particle valve - Task 2	113
IV.	Provision of controlled quality low C steel shot and construction of the research SD casting furnace - Task 3	155
V.	Work in Progress	181
V.A	Introduction	184
V.B	Use of investment molds for SD process	186
V.C	Experimental verification of the infiltration equation (mass, momentum, and heat transfer during infiltration)	200

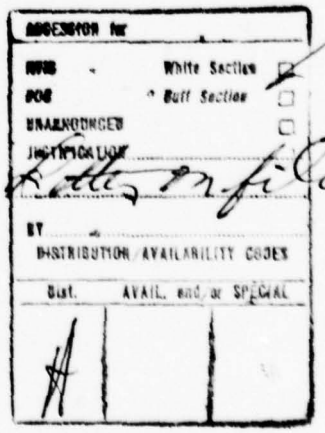

I. INTRODUCTION

In the SD (diffusion solidification) casting process* high carbon liquid iron is brought into contact with low carbon solid iron isothermally, and the liquid solidifies by rejecting carbon to the solid. The solidification mechanism is controlled by mass transfer rather than heat transfer as is the case in conventional castings. Advantages of the SD process over conventional casting processes and products result from (1) lower casting temperatures; (2) elimination of the need for a riser; (3) more rapid solidification; (4) plane-front as opposed to dendritic solidification; and (5) complete solidification under isothermal conditions. Diffusion solidification in the iron-carbon system can produce castings with greater than 99% of the theoretical density; solidification times typically range from a few seconds to several minutes, even for ingot sized castings; and tensile strengths as high as 185,000 psi with 15% reduction of area to break have been attained.

Diffusion solidification may make die casting of steel a commercially useful process because solidification takes place isothermally at lower-than-normal temperatures in a hot refractory mold, so that there is no contact between hot liquid steel and a cold mold. Since most of the casting can be made to solidify without rejecting heat to the surroundings, pieces with small surface-to-volume ratios or with drastic changes in cross section should be relatively easy to produce by diffusion solidification.

In the SD process solidification proceeds simultaneously throughout the casting, consequently both hot tearing and macrosegregation of impurities and alloying elements are minimized. The more uniform microstructure of diffusion solidified steels is especially useful for extremely heavy castings such as

---

* G. Langford, R. E. Cunningham: Met. Trans. B, Volume 9B, March 1978, p. 15.

tank bodies, and steam turbine or generator rotors, for example. The concept of diffusion solidification combined with new molding concepts such as the V-process results in a new approach to rapid cycle casting of steel parts.

Our initial proposal* called for a series of critical experiments to be performed to determine the extent to which the process economics are controlled by the advantages and limitations imposed on the process variables. The statement of work to be done, shown below, attacks the program of rapid cycle steel casting from two viewpoints: (i) investigation of parameters controlling the process economics, and (ii) investigation of parameters controlling the product quality:

Statement of Work to be Done

(i) The investigation of parameters controlling the process economics will include:

1. Measurement of the attainable rate of heating of low-carbon steel shot in a refractory mold, which may control the process cycle time.

2. Establishment of the operating characteristics and reliability of the quick-acting valve for controlling liquid metal flow into the shot-filled mold.

3. Development of a method of controlling mold permeability to waste gases, pressurizing gas and liquid metal.

4. Measurement of the tensile properties of partially frozen SD castings to establish the fraction solidified at which it is safe to remove the casting from the mold.

5. Demonstration of control of chemical activity of liquid high-carbon iron with respect to solid iron to avoid channeling of the solid during infiltration.

6. Checking the validity of the theoretical expression for infiltration pressure.

---

* D. Apelian, G. Langford: Rapid Cycle Steel Casting, proposal submitted to ARPA, January 24, 1977.

7. Working out the detailed techniques for making suitable non-permanent molds.

8. Establishing the specifications and methods of manufacture of permanent molds.

9. Casting of selected engineering parts by the diffusion solidification process combined with the selected molding process.

(ii) The investigation of parameters controlling the product quality (and, indirectly, the process costs as well) will include:

1. Establishment of process variables affecting quality of atomized shot, including inclusion removal rate, atomization efficiency, solidification distance of shot in free flight, shot size distribution, rate of reoxidation after solidification, and recycling the purification gas.

2. Establishment of process variables affecting ductility of finished casting, including the kinetics and stoichiometry of solid-state, vacuum-carbon deoxidation of the shot during heating to the process temperature.

3. Provision of selected parts or billets made from SD cast steel for use tests to establish performance data and to uncover unforseen problems; failure analyses on these parts.

During the first year (7/1/77 - 6/30/78) of the program several of these objectives or tasks were completed and are reported here.

Suitable methods for heating the components of the SD casting to process temperatures are evaluated and reported in Section II (Task I). The attainable rate and efficiency of heating are important process parameters since they ultimately control the process cycle time in certain SD process logics.

Work on the performance, reliability and operating characteristics of the quick-acting valve for controlling liquid metal flow into the shot filled mold is reported in Section III (Task 2). The required breakthrough pressure is derived and experimentally confirmed using Sn/Al_2O_3, Hg/Al_2O_3 and Fe/Al_2O_3 systems.

Details of the newly designed and built atomization unit to produce the low-carbon iron shot, and the casting furnace to produce steel castings via the SD process are given in Section IV (Task 3).

Work in progress, such as the mold permeability problem, the infiltration kinetics, as well as specific alloys that are being investigated are described in Section V.

II. Heating Methods in Manufacturing Diffusion Solidified Steel Castings - Task 1

H. Sreshta
G. Langford
D. Apelian

SUMMARY

Various heating methods for manufacturing SD castings are described: electrical heating (direct and indirect), direct gas heating and radiative heating. The advantages and limitations of the heating methods are discussed. The economic SD variables (heating time and efficiency) are estimated for direct electrical induction heating and radiative heating of shot. One kg of unbonded shot can be heated to SD process temperatures (1400°C) in 100 to 200 seconds at heating efficiencies of 10 to 15 percent by direct induction heating. The electrical resistivity of unbonded steel spheroids is an important parameter which influences the economic variables for direct induction heating. The electrical resistivity is extremely high up to 200°C, causing the "incubation period" previously observed but above 200°C the resistivity is controlled by the surface oxides on the particles permitting electrical conduction in the bed at temperatures of about 400°C. The incubation period can be circumvented by preheating the powders. One kg of unbonded shot can be heated to process temperatures in 2000 seconds at heating efficiencies of 5 percent by the radiative heating method. The heating time is controlled by the heat transport rate in the bed which again appears to be controlled by electronic conductivity. Theoretical estimates of the SD economic variables are made for gas heating of shot. A process efficiency of 50 percent is expected and one kg of shot can be heated to process temperatures in 100 seconds using a 1 kW compressor to pump the gas. The heating rates and efficiencies could be greatly increased if the shot could be electrically bonded (by a pre-sintering or mechanical treatment, for example) before the start of the casting cycle. Direct induction heating and radiative heating methods are applicable to SD casting manufacture using a batch process. A semi-continuous process is required for manufacturing SD castings using the direct gas heating method.

TABLE OF CONTENTS: Section II. Heating Methods in Manufacturing Diffusion Solidified Steel Castings

II.A Introduction 9

II.B Heating Time 10

II.C Heating Methods 10

II.D Evaluation Criteria for Heating 12

1. Temperature Control 12
2. Economic Analysis 13

II.E Specific Heating Methods 15

1. Resistance Heating 15
   a. Advantages 15
   b. Disadvantages 15
2. Gas Heating 16
   a. Gas Heating of Shot in Molds 16
      i. Advantages 17
      ii. Disadvantages 17
   b. Heating Particles Individually by Hot Gas 18
      i. Advantages 18
      ii. Disadvantages 19
3. Radiative Heating 19
   a. Theoretical Considerations of Radiative Heating of Shot in a Mold 20
   b. Experimental Results on Radiative Heating of Shot 21
   c. Radiative Heating of All Three SD Charge Components in a Mold 22
   d. Advantages 23
   e. Disadvantages 23
4. Direct Induction Heating 24
   a. Induction Heating of Low Carbon Particles 25
   b. Use of Direct Induction Heating for Manufacturing SD Castings 26
      i. Frequency of Induction Heating 27
      ii. Resistivity of Packed Beds 29
      iii. Incubation Period 31
      iv. Effect of Magnetic Transformation 32
      v. Induction Coils 32
      vi. Mold Geometry 33
      vii. Power Input to Packed Bed 33
   c. Problems of Direct Induction Heating for Manufacturing SD Castings 33
      i. Cracking of Packed Bed During Heating 33
      ii. Preferential Coupling 34

iii. Heating of Particle Valve 34
iv. Mold Limitations 35
d. Advantages..... 35
e. Disadvantages..... 35

II.F Conclusions 36

II.G Future Work 37

References 37

Tables 38

Figures 39

Appendices 43

II-A Heating of Low Carbon Steel Particles by Forced Gas Infiltration 43

II-B Radiative Heating Experimental Results 52

II-C Energy Requirements for Manufacturing SD Castings using a Batch Process 56

II-D Induction Heating Experimental Results 61

II-E Induction Heating Characteristics of a Packed Bed of Low Carbon Steel Particles 87

II-F. Critical Packed Bed Diameter and Frequency for Induction Heating of Particles 91

II-G Room Temperature Resistivity of Powder 98

II-H Powder Characterization 105

II-I Cracking Phenomena in Induction Heated Packed Beds 110

II.A INTRODUCTION

Suitable heating methods are evaluated with emphasis on the economics of heating the SD components (cast iron shot, particle valve and mold) to process temperatures. The heating times and efficiencies are estimated for direct and indirect heating methods. The advantages and limitations of some specific heating methods for manufacturing SD castings are discussed.

The heating time for SD casting batch processes is an important economic variable. A batch process for SD casting involves the following steps: transfer of the SD components to the furnace inside the pressure vessel, heating the components to casting temperatures, pressurization of the furnace chamber to infiltrate the cast iron liquid into the porous solid, and, finally, removal of the casting from the furnace after solidification is complete.

The cycle time for an SD batch process includes three main components:

- heating time
- solidification time
- idle and reloading time

The idle and heating times must be comparable to the solidification time to benefit economically from the rapid solidification attained in the SD process.

The heating time for an SD batch process using indirect heating methods follows the same relationship as the solidification time for conventional castings. The cycle time has one of its components obeying an ℓ^2 scaling law and so will be no better than comparable to the solidification time for conventional castings. Under such circumstances, the SD process must rely on superior casting quality to be competitive with the conventional casting process.

The heating time for SD batch process using direct heating methods is inversely proportional to the power input to the SD components. The heating

time is controlled by the power rating of the heating equipment. Direct heating makes it possible to attain heating times comparable to or less than the SD solidification time. The cycle times using direct heating methods are expected to be less than the solidification times for the conventional process, giving the SD process an economic edge over the conventional casting process.

A semi-continuous SD casting process, wherein the SD components can be separately heated to casting temperatures and then combined, offers better utilization of the heating methods at the expense of increasing the complexity of the casting machine. The cycle time is controlled by the slowest indivisible step in the process, making it possible to take maximum advantage of the weaker dependence of SD process solidification time on casting size compared to that of a conventional casting process. To use a semi-continuous process for SD casting manufacture requires that the economic gains resulting from low cycle times must offset the increased capital cost for equipment.

II.B HEATING TIME

An economic rapid cycle casting process for steel must achieve the correct casting temperature in a time comparable to the solidification time, or it must do so in such a manner that the heating time does not control the cycle time. The former would be a batch process in which the heat transfer to the casting components controls the cycle time, the latter would be a continuous or semi-continuous process in which the components are heated in a separate (low cost) furnace before being transferred to the casting machine itself.

II.C HEATING METHODS

Since we are being purposefully vague about the details of the casting logic at this early stage in the development of the SD process, our investigation

of the heating routes makes no limiting assumptions about the specific arrangements or even the necessity of the key parts of the apparatus, which include the mold, low carbon steel solid, particle valve and liquid cast iron.

The heating routes considered are grouped into two main categories: direct and indirect. The direct methods dissipate energy throughout the mass of the casting components and include:

- induction heating of metallic components
- heating of individual particles by gas
- heating of shot in a mold by gas

The indirect methods involve heat transfer from an external source to the outside surface of the individual (or grouped) casting components, followed by conductive and radiative heat transfer within the bulk. The indirect methods include:

- radiative heating using a graphite susceptor heated by induction
- radiative heating using a high temperature resistance winding
- radiative heating using a tubular furnace heated by gas.

The direct routes are considered separately from the indirect routes. The reason for this distinction is that we are comparing the SD process and its $(\ell^{6/5})/(P^{2/5})$ scaling law for solidification time to a conventional thermal solidification process which obeys an (ℓ^2) scaling law.[1,2] The conventional casting process time is controlled by heat transfer from the bulk of the casting, whereas the SD process economics ought to be controlled by short-range carbon diffusion, not by so mundane a consideration as bulk heat transfer.

The last stage of either category of heating route involves equalization of internal temperature of the components to attain control of the casting temperature. In both categories the equilibrium time is controlled by the diffusion of heat in the bulk, which again involves an (ℓ^2) scaling law, if the temperature gradients are on a scale comparable to the scale of the casting.

Clearly the distinction between indirect and direct heating methods will be only a matter of degree unless the direct route is so accurate that no temperature equalization is required at all.

II.D EVALUATION CRITERIA FOR HEATING

1. Temperature Control

Steel casting by SD requires that the two main components of the casting be at nearly the same temperature before being brought together. The temperature limits have been defined by Langford and Cunningham:[1] the high carbon liquid must be saturated with respect to iron when it first contacts the solid. The liquid must therefore be at or slightly below the liquidus so that the actual carbon content of the iron-saturated liquid will be higher than the average composition of the liquid component; if the liquid is above the liquidus, the low carbon solid will be partially dissolved by the advancing superheated liquid - an undesirable situation from the point of view of casting quality. Conversely, the low carbon steel shot must be neither too hot, which would reduce the fraction solidified adiabatically, nor too cold, which would cause excessive thermal solidification of the liquid, adversely affecting the casting quality.

The range of temperature control for the liquid should not cause more of an error in the final carbon content than the rest of the casting process (where the time taken for infiltrating the liquid through the solid low carbon steel determines the macrosegregation of carbon - ±0.15 percent carbon at most[1]). Since the carbon content of the liquid is about 2.5 times the overall carbon content for a casting made with a mold filled with low carbon steel shot and the liquidus slopes downwards 100°C per weight percent increase in carbon content for plain carbon steel, the temperature of iron-saturated liquid should be kept within ±40°C of the intended casting temperature at the very worst.

Concerning the low carbon solid particles, the allowable casting temperature range is less easily defined, since both casting time and casting quality are influenced by errors in the casting temperature. Overheating the shot by 50°C, for example, will reduce the degree of adiabatic solidification by about half; this may necessitate waiting even longer for the excess heat to be lost to the surroundings, or it may not; to find out we must await the results of the tensile tests on partially solidified SD castings to see how rapidly the mechanical properties are developed after the shot has been infiltrated with liquid. Underheating the shot by as much as 50°C will probably reduce the effectiveness of the infiltration and reduce casting quality as well; Langford and Cunningham[1] found that the strength and ductility of SD castings were adversely affected by excessive underheating or by inadequate infiltration pressure.

Therefore, we can state somewhat categorically that the temperatures of SD castings and components must be controlled within ±50°C, perhaps as closely as ±10°C; there is no reason to expect to have to achieve accuracy greater than ±10°C.

2. Economic Analysis

The economic variables are: heating efficiency, heating time, cost of heating equipment and product quality. The influence of heating route on product quality will be discussed later.

It is desirable to operate the process at a high heating efficiency to minimize the operating costs. The heating efficiency could be enhanced by using more complex equipment and increasing the furnace insulation to reduce heat losses. This however increases the capital cost of furnace and equipment.

The heating time is an economic variable depending on the heating route taken to manufacture SD castings. If all the SD components are heated in the pressure vessel as assumed in the original proposal[2], the heating time will

control the cycle time. An approximate relationship for cycle time derived in reference (2) is given by Eq. [1]

$$t_c = 2100\ d_p^{\,2} \qquad [1]$$

where

t_c - cycle time, seconds

d_p - particle diameter, mm

Table I gives the cycle time as a function of particle size. The strong dependence of cycle time on particle size may not be a realistic assumption. The cycle time for 0.25mm particles is 130 seconds compared to 3280 seconds for 1.25mm particles. The main contribution to the difference in cycle times for the above cases comes from the heating time. Beside particle size the heating time is also influenced by the geometry and size of the casting. The method of heating is also an important variable controlling the heating time.

The heating route decision criteria can be summarized by a function 'P' given by Eq. [2]

$$P = C_1 qW - C_2 t_c - C_3 \eta E - C_4 \qquad [2]$$

where, C_1, C_2, C_3 are constants which must be evaluated for each route

q - product quality factor; q = 1 for an ideal casting

W - weight of casting

t_c - cycle time

E - theoretical energy requirements for making a casting

C_4 - capital cost of equipment

P - a measure of the profit.

η - heating efficiency

The function 'P' given by Eq. [2] will ultimately serve as the basis for evaluating the optimum heating route for manufacturing SD castings.

II.E SPECIFIC HEATING METHODS

1. Resistance Heating

a. Advantages

Resistance heating has been successfully used in several applications. Its advantages are:

- the operation principle is simple
- the equipment costs are lower than for the other heating methods. The heating apparatus involves high temperature furnace winding elements and a power supply.

b. Disadvantages

The disadvantages for using resistance heating for manufacturing SD castings are listed below:

- Resistance heating can be used as a direct heating method only when the heating element is the work piece itself. The problem of obtaining electrical contact to the components of the casting are considered insurmountable in the present context. However, an induced electrical current can achieve the same effect. This is discussed later.

- Resistance heating can be an indirect heating method using an external resistance element. In this case, the mold wall acts as a resistance to heat transfer, requiring that the winding temperature be much higher than the SD casting temperature. To attain SD casting temperatures in the range of 1250°C to 1400°C requires the furnace winding to be at 1600°C to 2000°C. These furnace temperatures require the use of expensive winding elements.

- Resistance heating will be applicable only to manufacturing castings using investment molds.

As an indirect heating method, resistance heating can be used for manufacturing SD castings provided it is possible to attain temperatures in the range of 1600°C to 2000°C. The heating time will be proportional to the square of the casting dimensions and will control the cycle time. The economic disadvantage resulting from higher cycle times is offset to a certain extent by the lower capital investment costs for the heating equipment. Low capacity SD casting plants may find the resistance heating route most economical for manufacturing castings.

2. Gas Heating

Gas heating could be used as a direct heating method by passing the gas through the porous solid contained in a mold. The method cannot be used by itself to manufacture SD castings using a batch process. At process temperatures the gas path is obstructed by the liquid charge on top of the particle valve. Gas heating is therefore limited either to heating the shot and particle valve in the mold or heating the individual shot particles to process temperatures.

a. Gas Heating of Shot in Molds

Appendix II-A outlines the gas heating of shot in a mold. The analysis has been done from an economic viewpoint. Table II-A-III, Appendix II-A, summarizes the general relationships between the economic variables controlling this method of heating. At these temperatures sintering of the particles is predominant and it is not possible to transfer the particles as they would have agglomerated. The mold used must be impermeable to gas to prevent gas from escaping during the heating period. The gas used must be inert to the particles.

This method of heating can be effectively used for manufacturing SD castings with permanent molds. The particles are first heated in the mold by gas. The mold is then evacuated and infiltrated with liquid cast iron. Fig. 1 shows a flow sheet for such a process.

i. Advantages of Gas Heating of Particles in Mold

- The heating time is dictated by the gas flow rate in the packed bed. The heating time for a 1.5 kg casting is 100 seconds if a 1 kW compressor is used to pump the gas (Appendix II-A).

- The packed bed can be heated to uniform temperatures, i.e. the temperature gradient problem in the bed and in the particle valve as well can be avoided.

- The heating efficiency can be increased by recuperating the sensible heat of the gas leaving the mold. Without this feature only 63 percent of the gas inlet energy is utilized in heating the particles (Appendix II-A).

ii. Disadvantages of Gas Heating of Particles in a Mold

- The manufacture of castings involves a two stage process. The shot is heated by gas and then infiltrated by liquid cast iron. The apparatus necessary for shot heating includes a gas compressor, heat exchanger, and recuperator. The melting of cast iron must be done in a separate furnace. The infiltration of cast iron liquid into the heated shot must be done in an inert atmosphere. The different steps involved in the casting process makes such an SD casting machine very complex. The capital costs will be greater than for an

SD batch process.

- High temperature seals between the mold and gas inlet port must be used to prevent gas leakage.

b. Heating Particles Individually by Hot Gas

If it is possible to heat the particles to casting temperatures such that they do not make contact with each other above the sintering temperature, then the heated particles could be used to fill all the types of molds cited in [2]. Such a method of gas heating is illustrated in Fig. 2. The operation closely approximates countercurrent drying of solids by gas. In this case, however, the chamber is vertical. The particles could be made to fall with a very low velocity in the heating chamber by maintaining a suitable upward gas flow rate. The method permits the transfer of particles at the SD casting temperatures to molds.

i. Advantages of Gas Heating by Semi-Fluidization Techniques

- It is a versatile technique imposing no restriction on the type of mold that can be used for manufacturing the casting.
- A high heating efficiency can be attained if the sensible heat of the gas leaving the chamber is recovered.
- The mold wall acts as insulation, reducing heat losses from the hot particles to the surroundings.
- The particles and particle valve can be heated uniformly to SD casting temperatures.

ii. Disadvantages of Gas Heating by Semi-Fluidization Techniques

- The casting machine will be more complex than gas heating of particles in a mold, requiring higher capital investment for heating and mechanical equipment.
- A number of heating chambers will be required to ensure that if there is a breakdown in one chamber, the plant is not shut down.
- Some types of molds must be preheated to withstand thermal shock resulting from the contact of hot particles with the mold.

Gas heating as a direct method is not adaptable to SD batch processes and must be considered as a semi-continuous process for manufacturing castings. The cycle time is controlled by the slowest indivisible step in the process, i.e., either the heating time for shot, the infiltration of cast iron liquid into the shot, or the SD solidification time. The economic advantage gained by low cycle times is partly offset by the higher investment costs for the process. In cases where high production rates are desired, the gas heating route is favored over SD batch process for casting manufacture.

3. Radiative Heating

Radiative heating is an indirect method for heating SD charge components to process temperatures. The charge is contained in mold and is surrounded by a hot source maintained at high temperatures. At high temperatures, radiation is the predominant mode of heat transfer.

A hot source can be provided in several ways, for example by a high temperature silicon carbide resistance winding. We shall choose a graphite susceptor heated by audio frequency induction. A graphite susceptor couples

efficiently to the induction flux and can be rapidly heated to high temperatures (1800°C to 2000°C). The susceptor could be maintained at these temperatures with power inputs of about 10 kW for manufacturing SD castings of diameter 2 to 3 in. (50 to 75 mm) and height of 4 in.(100 mm). Fig. 3 shows the setup for manufacturing SD castings using the radiative heating route.

a. Theoretical Considerations of Radiative Heating of Shot in a Mold

Fig. 4 illustrates a typical radial temperature distribution in a cylindrical mold containing shot when placed in a heated susceptor at a temperature, T_H. The temperature distribution is at an arbitrary time during the heating process.

The heating of shot is an unsteady state process. The rate of heat transport from the susceptor to the mold is given by Eq. [3]

$$Q_1 = (T_H^4 - T_m^4)\ \varepsilon_m \qquad [3]$$

Across the mold wall, heat is transported by conduction and is given by Eq. [4]

$$Q_2 = k_m \frac{(T_m - T_s)}{t_m} \qquad [4]$$

The heat transfer rate in the packed bed is given by Eq. [5]

$$Q_3 = k_{PB} \frac{(T_s - T_c)}{d_{PB}} \qquad [5]$$

where

Q_1 - rate of heat transfer to the mold

Q_2 - rate of heat transfer across mold wall

Q_3 - rate of heat transfer in the shot

T_H - susceptor temperature

T_m - mold wall temperature

t_m - mold wall thickness

T_s - temperature at the interface between mold wall and packed bed

T_c - temperature at the center of the packed bed

ϵ_m - thermal emissivity of mold surface

k_{PB} - effective thermal conductivity of the packed bed

The slowest rate of heat transport given by Eqs. [3, 4 and 5] will control the heating time.

b. Experimental Results on Radiative Heating of Shot

Appendix II-B gives the experimental results for heating RESD powder* contained in an alumina mold. The results indicate that during the early stages of heating the packed bed heats at a very slow rate. The surface of the packed bed attained casting temperatures in about 1200 seconds while the interior temperature increased by 100°C during the same period. The large driving force for heat flow is offset by the low thermal conductivity of the bed during this period. After 1200 seconds, the temperature of the packed bed interior increased from 400°C to 1350°C in just 1000 seconds. This period is characterized by an enhanced thermal conductivity of the bed resulting from sintering of the particles. The increase in thermal conductivity offsets the slower heat flow here. Radiative heat transport may also be a contributing factor for increasing the radial heat flow in the packed bed during the later stages of radiative heating.

A packed bed containing 1.2 kg of particles was heated from 350°C to 1350°C in 2200 seconds. The heating time can be reduced by increasing the susceptor temperature. A higher susceptor temperature would raise the packed bed surface temperature to casting temperature more rapidly promoting sintering at the

* The nomenclature and characterization of the powder are covered by Appendix II-H.

packed bed surface and accelerating the radial heat flow into the bed. The heating efficiency was estimated to be only 4.2 percent. It can be increased by using a thicker susceptor and by shielding the opening at the top of susceptor to reduce radiation losses.

c. Radiative Heating of All Three SD Charge Components in a Mold

Since radiative heating is an indirect method, the heat must be transported across a surface. The theoretical energy density of a 1 kg casting has been estimated in Appendix II-C for all the components. The particle valve requires the lowest energy density. Using a higher energy density at the location of the particle valve may locally raise its temperature above the casting temperature requiring additional time for heat transfer from the particle valve to the cast iron liquid and shot for temperature equilibration.

It is desirable to heat the cast iron and shot simultaneously to process temperatures for manufacturing SD castings. High susceptor temperatures can be attained in a short time. Lowering the temperature of a susceptor that is well insulated in an evacuated chamber will take a much longer time. Hence if one of the components attains process temperature before the other it will be difficult to prevent it from superheating while the other attains process temperature. This will occur in the case where the susceptor has a uniform temperature in the axial direction. The cast iron charge requires a higher energy density than the shot and so if a susceptor with a uniform temperature is used, the shot would be preheated when the cast iron reaches process temperatures.

The problem of supplying different energy densities to the cast iron charge could be solved in four ways:

- By using two susceptors heated by two different induction coils. The susceptors would be electrically and thermally isolated from each other.

- By using a susceptor with varying cross section. The temperature of such a susceptor would be a function of its thickness. The cross sectional thickness in the cast iron zone must be larger than that in the shot zone.

- By increasing the concentration of coil turns in the cast iron instead of evenly spacing them throughout the susceptor length.

- By changing the packing efficiency of the particle valve and cast iron charge to equalize the required energy densities.

d. Advantages of Radiative Heating

- High source temperatures can be attained using a graphite susceptor. At these temperatures it may be possible to manufacture SD castings in reasonable heating times.

- High heating efficiencies can be obtained for radiative heating provided the susceptor is well insulated from the surroundings.

- The capital costs are lower than for the gas heating route. SD castings could be made by heating the components in a furnace located in a pressure vessel.

e. Disadvantages of Radiative Heating

- There may be problems using this method for manufacturing irregularly shaped castings. Either the efficiency or the time of heating will be controlled by the largest cross section.

- The mold must be preheated so that it does not crack when placed near the hot source.

- Radiative heating cannot be used for permanent and vacuum molds.

Radiative heating is definitely a suitable candidate for manufacturing SD castings by a batch process. The heating time is proportional to the square of the casting dimensions and so will control the cycle time for the process. There is no time advantage gained from the weaker dependence of solidification time on casting dimensions if the radiation heating route is used to manufacture SD castings.

4. Direct Induction Heating

Induction heating (IH) is one of the three methods of using direct dissipation of electrical energy to heat the work material. It provides a means for precise heating of electrically conducting objects. IH is clean, fast, repeatable and lends itself to automatic cycling. Some of the general advantages of IH are:

- No contact is required between the work load and heat source.

- Very high temperatures can be attained.

- Rapid heating of the workpiece is easily achieved.

- Higher efficiency than that offered by many furnace methods can be realized.

- Heating depth can be controlled by changing the frequency of the alternating field.

- Working conditions are cooler and cleaner.

- Vacuum or controlled atmospheres may be used to protect the workpiece.

The use of direct IH for manufacturing SD castings depends on the impedance of the individual components. Cast iron in the form of lumps can be easily melted by IH. Much literature is available outlining procedures for induction melting of metals and alloys. The particle valve, which necessarily consists of refractory particles, will remain inert to the induction flux because of its high resistivity ($\rho > 10^{12} \Omega \cdot m$). This implies that the particle valve must be heated by the cast iron and shot during IH. The IH of loosely packed particles in a bed is a new area which has not yet been reported in the literature. The key to making SD castings by IH revolves around the feasibility of inducing substantial electric currents in a packed bed of low carbon steel powders.

a. Induction Heating of Low Carbon Particles

Recently published work by Conta[3] on the IH of powder compacts does offer a guideline to predict the IH characteristics of powders. An incubation period was encountered by Conta at the beginning stages of audio frequency (3 kHz) heating for low-alloy steel, unsintered powder compacts. The incubation period was a function of the surface power density and the compact density. The incubation period was attributed to the high resistivity of the compacts resulting from surface adsorbtion of gases on the particles in the compact. The incubation period was circumvented by preheating the compacts to 400°F (205°C).

The results of Conta[3] on IH of powder compacts served as the basis for doing the present series of experiments to study the IH characteristics of low carbon steel powders in a packed bed. Appendix II-D gives the results of the experimental runs.

The analysis of IH of spherical low carbon steel particles contained in a mold in Appendix II-E assumes that the packed bed has a resistivity that is not temperature sensitive, enabling the packed bed to be coupled to the

induction flux using an appropriate frequency. Experimental results indicate that this assumption is not valid. The resistivity of the packed bed is temperature sensitive below 400°C. Hence below 400°C it is not possible to get good load coupling using a single frequency for IH.

The incubation period encountered at the beginning stages of audio frequency (4.2 kHz) heating is characterized by poor load coupling and inefficient heating. High packed bed resistivity is isolated as the cause of the incubation period. The high packed bed resistivity accounted for the incubation period observed even at radio frequency (450 kHz) heating. During audio frequency (4.2 kHz) heating no radial gradients were observed in the bed, the reason being that the depth of penetration of the magnetic flux was greater than the radius of the packed bed. With radio frequency heating the packed bed coupled to the induction flux. The interior of the packed bed was heated by conduction and radiation from the hot zone where heat was generated due to resistance losses. The packed bed was found to have poor radial and axial thermal transport properties.

b. Use of Direct Induction Heating for Manufacturing SD Castings

The use of direct IH for manufacturing SD castings using a batch process must satisfy the following economic objectives:

- Minimization of heating time.
- Uniform heating of particles in the bed to ensure good casting quality.
- Maximization of power utilization.

These objectives are interrelated and so it may not be possible to satisfy all three criteria simultaneously. The interdependence of the objectives calls for an optimum combination from an economic viewpoint. The economic variables for IH of particles are influenced by the parameters listed below:

- frequency of IH
- resistivity of packed bed
- incubation period
- effect of magnetic transformation
- induction coil
- mold geometry
- power input

The above parameters will be discussed with emphasis on the economic variables.

i. Frequency of Induction Heating

The frequency of IH is an important heating parameter. It controls the reference depth or the dimensions of the zone where power is dissipated. The depth of penetration is defined as the depth at which the induced current has reached about 37 percent of its value at the surface of the charge. It is governed by the relationship

$$\delta = 0.018\sqrt{\frac{\rho}{\mu f}} \qquad [6]$$

where

δ - depth of penetration, m

ρ - resistivity of charge, $\Omega \cdot m$

μ - material magnetic permeability, $T \cdot m \cdot A^{-1}$

f - frequency, kHz

The reference depth, δ, is inversely proportional to the square root of the frequency. At low frequencies the depth of penetration is large, whereas at high frequencies the depth of penetration is small, i.e., skin heating is observed. The packed bed has poor thermal transport properties and it is

desirable to use a low frequency for heating so that the power is dissipated in a large zone resulting in uniform heating of the bed.

The lower bound on the choice of frequency is fixed by heating efficiency considerations. The efficiency is controlled by the load-coupling characteristics of the charge. The depth of penetration must be smaller than half the radius of the packed bed as in Eq. [7] for efficient power transfer to the charge.

$$d_{PB} \geq 4\delta \qquad [7]$$

where d_{PB} is the diameter of the packed bed. Substituting for δ in Eq. [6]

$$d_{PB} \geq 0.072 \sqrt{\frac{\rho}{\mu f}} \qquad [8]$$

The inequality given by Eq. [8] must be satisfied for efficiently heating the charge. The critical packed bed diameter for efficient heating for a range of resistivities and frequencies is given in Appendix II-F.

Assume that a frequency is chosen that ensures good load coupling. The IH characteristics for this case are described in Appendix II-E.

The heated zone can be rapidly raised to process temperatures but the interior remains inert to the induction flux. The packed bed interior must be heated by radiative and conductive heat transfer from the hot zone. Experimental results indicate that radial heat transport in packed beds is a slow process and so will control the heating time as in the indirect radiative heating method. Hence it is only possible to attain uniform temperature distribution in the packed bed with minimal heating time if the penetration depth, δ, is large enough to permit the entire packed bed diameter to be heated simultaneously at substantial sacrifice in the heating efficiency. This agrees with our experimental results. The RESD powder could be heated uniformly at low frequencies to process temperatures in about 300 seconds at efficiencies of 10 to 15 percent.

ii. Resistivity of Packed Beds

The depth of penetration is proportional to the square root of the resistivity of the packed bed. No data was available in the literature giving the resistivity of a packed bed of low carbon steel particles. Room temperature resistivity was measured for the different powders used for IH runs. The experimental procedure and results are given in Appendix II-G.

The room-temperature resistivity of powders follows the relationship given by Eq. [9].

$$\rho = \rho_o [h_{PB}]^n \qquad [9]$$

where

ρ_o and n are constants

h_{PB} - height of packed bed.

The resistivity is not a constant but a function of the bed height.

The resistivity is strongly influenced by the surface morphology of the powders. Conta[3] attributed the high resistivity of particles in a bed to adsorbed gases on the particles. This postulation agrees with our experimental results. The adsorption phenomenon is controlled by the surface area of the particles. STSD powder had a lot of surface perturbations whereas STSDDO powder had a relatively smooth surface. The large difference in the resistivity of particles with the same size but with different surface morphologies confirms that the resistivity is controlled by the gases adsorbed on the particles at room temperature.

The resistivity of RESD powder was measured as a function of temperature. The results are given in Fig. II-D9, Appendix II-D. The data indicate that resistivity is controlled by three different phenomena: adsorbed gases at low temperatures, sintering by neck growth at high temperatures and surface

oxides at intermediate temperatures. The resistivity was very temperature sensitive up to 200°C. The resistivity drop results from the release of gases, especially water vapor, from the surface of the particles. In the temperature range of 200°C to 400°C, the resistivity drops linearly with temperature. The mechanism responsible for the phenomenon is defect semiconduction of the oxide layer on the particles. In the temperature range of 400°C to 950°C the resistivity approaches a constant value as a result of the exhaustion phenomenon observed in defect semiconductors. Above 950°C, the resistivity drops gradually with temperature due to sintering of the particles in the packed bed. During reheating of a packed bed, which has previously been heated above the sintering temperature, the first two stages of this resistivity-temperature curve are skipped entirely.

The resistivity as a function of temperature was not measured for the other powders used for IH. The RESD powder had a very low oxygen content (0.022 percent). The other powder, characterized in Appendix II-H,had oxygen contents greater than RESD powder. Hence it is reasonable to assume that the packed bed resistivity of steel powders with oxygen contents greater than 0.022 percent follows the same type of resistivity-temperature relationship as RESD powder.

The resistivity of RESD powder dropped from 7.4 Ω·m at 37°C to 0.0015 Ω·m at 400°C. The resistivity was approximately constant with a value of 0.00145 Ω·m in the temperature range of 400°C to 950°C. The strong temperature dependence of resistivity up to 400°C prevents efficient heating of the powder using a single induction frequency. Once the packed bed resistivity approaches a constant value, the particles can be efficiently heated. Maximum heating efficiency for a 60mm diameter packed bed of RESD powder can be attained if the bed is heated from 400°C to the Curie temperature (771°C) at a frequency of 45 kHz and at a frequency of 1 MHz above the Curie temperature.

Most of the IH runs were done at 4.2 kHz. At this frequency and with a resistivity of the packed bed equal to 0.00145 Ω·m, the depth of penetration was 50mm below the Curie temperature and 250mm above the Curie temperature. The large depth of penetration accounted for the uniform heating in the radial direction. However, the heating efficiency was low (15 percent).

iii. Incubation Period

An incubation period is observed during IH of powder. The cause is attributed to the high resistivity of the packed bed, resulting in poor load coupling to the induction flux. The heating during this period is slow and inefficient.

The incubation period is a function of the power input to the charge and the particle size. The power input controls the duration of the incubation period. At low power the incubation period lasted for 1200 to 1800 seconds. At high power inputs it was difficult to study the incubation phenomenon. The rapid change in the resistivity with temperature required adjustments of the capacitance in the resonant circuit, a cumbersome task for our equipment. Under such circumstances it was difficult to maintain a steady power input to the charge.

The particle size had an inverse relationship to the incubation period. The STLDDO powder showed no signs of an incubation period, the reason being that the incubation heating efficiency and the heating efficiency for this powder are comparable and very low (6 percent). The RESD powder showed a characteristic incubation period.

The incubation period is characterized by a low heating efficiency (6 to 7 percent). During this period the particles are heated by magnetic hysteresis losses. An incubation period of 1200 to 1800 seconds will control the heating time. The incubation period can be circumvented by preheating the particles to an adequate temperature, the coupling temperature, that

ensures load coupling to the induction flux. The coupling temperature for RESD powder was found to be 425°C.

iv. Effect of Magnetic Transformation

The Curie temperature for low carbon steel powders is 771°C. Below this temperature the powders are magnetic and above it the powders are nonmagnetic. At the Curie temperature there is a sudden change in the magnetic permeability as given by Eqs. [10] and [11]

$$\text{below } 771°C, \quad \mu = 3.1 \times 10^{-5} \text{ Tesla/(Ampere/meter)} \qquad [10]$$

$$\text{above } 771°C, \quad \mu = 1.25 \times 10^{-6} \text{ Tesla/(Ampere/meter)} \qquad [11]$$

The depth of penetration is inversely proportional to the square root of the magnetic permeability. The sudden decrease in the permeability at the Curie temperature will result in an increase of the depth of penetration. Such an increase may violate the inequality given by Eq. [8], leading to poor load coupling. With audio frequency heating, this has not been much of a problem. The charge impedance changes at the magnetic transformation but this can be offset by adding sufficient capacitance to the heating coil circuit.

v. Induction Coils

The induction coils influence the longitudinal temperature distribution in the packed bed. Experimental results indicate that at least 3 turns should be placed above and below the charge to heat the packed bed uniformly in the axial direction. If this is not done then longitudinal gradients are predominant in the packed bed and it takes a long time to equilibrate the temperature gradients.

The coils should be wrapped as closely as possible around the workpiece to obtain efficient heating. Oddly shaped workpieces may require impractical or inefficient coil geometries.

It is desirable to space the coil turns as close as possible and reduce the gap between the coils and the charge for efficient heating. The diameter of the coil tubing does not influence the economic variables, but it does influence the reliability of the setup by reducing the gap between turns.

vi. Mold Geometry

Particles contained in cylindrical molds can be rapidly and uniformly heated using audio frequency induction. No experimental work has been done on irregularly shaped packed beds. The IH characteristics of audio frequency heating for irregularly shaped molds containing particles can be extrapolated from the experimental results. The considerable depth of penetration at 4.2 kHz for low carbon steel particles will permit uniform heating of packed beds with varying cross sections. However, localized hot spots may result near the surface of the larger cross sections due to greater power dissipation in these areas combined with earlier sintering there.

vii. Power Input to Packed Bed

The power input to the packed bed has little influence on the efficiency of heating. However, it does affect the heating time. At high power inputs the packed bed could be raised to process temperatures in 180 seconds. The time for heating could be further cut down by the use of self-coupling IH units, where there is no idle time for compensation for changes in load impedance.

c. Problems of Direct Induction Heating for Manufacturing SD Castings

i. Cracking of Packed Bed During Heating

The cracking phenomenon observed during IH of particles in a mold is explained in Appendix II-I. Cracks in the packed bed of low carbon steel particles will affect the casting quality by changing the local packing

density. The cracks can be avoided if at sintering temperatures (1000°C to 1200°C) the power input to the bed is shot off for a short time to allow the particles to sinter together. This idle period during heating need last only 100 to 200 seconds.

ii. Preferential Coupling

The high resistivity of a packed bed of low carbon steel particles accounts for the preferential heating of bulk metallic components in the vicinity of the bed. SD casting manufacture by IH will therefore require that the cast iron charge above the shot have the same particle size as the shot itself so that both components can be simultaneously heated to process temperatures.

iii. Heating of Particle Valve

The material used for the particle valve must not be wet by the cast iron liquid or interact with the cast iron and low carbon steel particles at process temperatures. This dictates the use of non-conducting ceramics like silica, alumina, mullite, etc. which cannot be heated by induction. The particle valve must be heated indirectly by the cast iron charge above and low carbon particles below it. The energy required to heat a 10 mm deep particle valve for manufacturing a 1 kg casting is 81 kJ. (Appendix II-C). To supply this amount of energy by indirect means will take a considerable amount of time as indicated by the radiation heating results of a packed bed of steel particles. However, the heat capacity of alumina is 0.25 times that of steel per unit volume, permitting four times greater temperature gradients in the particle valve than in the metallic components. The cast iron and shot can be raised to process temperatures in about 200 seconds by IH. In the same time the temperature of the particle valve will be raised by a few hundred degrees. To avoid this problem it may be desirable

to preheat the alumina particles elsewhere to about 1000°C. At these temperatures the alumina particles do not sinter together. Alternatively, the particle valve could be reduced in thickness - perhaps to a few particle diameters - if ways could be found to make it so thin reliably; see Section III.

iv. Mold Limitations

For audio frequency IH we have attained heating rates of 3 to 5°C/s in the packed bed. The mold material is nonconducting and so is not heated by induction. The inside of the mold quickly attains the temperature of the particles, but the outside remains relatively cold resulting in large temperature gradients across the mold wall. The mold material must be able to withstand these temperature gradients or it may be necessary to preheat the mold to avoid thermal shock problems. Heating the particles at 3 to 5°C/s in a fully dense alumina crucible resulted in cracking of the crucible. No experiments were done using the type of molds cited in [2], which lie at two extremes: unbonded vacuum molds [4] and strongly dense permanent molds.

d. Advantages of Direct IH

- It lends itself to automatic cycling.
- The low carbon steel particles can be rapidly heated to SD casting temperatures.
- The method could be used for manufacturing SD casting by batch process if the cast iron is in the same form as the low carbon steel particles.

e. Disadvantages of Direct IH

- The IH of steel particles is a complex phenomenon. The operating conditions will vary depending on the particles used and the geometry of the casting. The thermal-power history to attain a uniform casting temperature in the SD components must be known prior to manufacturing the casting.

- Additional energy costs for atomization of the cast iron charge may be necessary.

- An idle time of 100 to 200 seconds to avoid cracks in the packed bed must be included in the heating schedule.

- Preheating of some types of mold may be necessary to avoid thermal shock at the heating rates attained during direct IH.

Direct induction heating is an effective method for uniformly heating the shot to process temperature in reasonable times. The method could be used for making SD castings via a batch process provided the cast iron charge has a resistivity comparable to that of the shot. We must await the results of simultaneously heating cast iron and shot by IH before outlining the procedure for manufacturing SD castings by this method.

Alternatively, IH could be used to manufacture SD castings via a semi-continuous process. The shot could be heated to SD casting temperatures in a mold by IH and then infiltrated with cast iron liquid melted elsewhere as proposed in the case of the gas heating method above.

II.F CONCLUSIONS

At this stage we can only conclude that radiative heating is the most suitable candidate for manufacturing an SD casting using a batch process. This means that the batch rapid cycle SD casting process can only be considered suitable for interim demonstration of the unique features of the diffusion solidification process, or where the product quality is extremely high, as in ultra high carbon high speed steel made by liquid infiltration.[5]

Several possible heating routes are available if a semi-continuous process is used for manufacturing SD castings. The assessment of these routes using

the economic criteria is subject to the feasibility of constructing an SD casting machine on a laboratory scale.

II.G FUTURE WORK

Objectives of the future work on heating methods are:

- To measure the relationship between the economic variables during gas heating of the shot. These experiments are necessary to refine the existing gas analysis given in Appendix II-A.

- To study the effect of source temperature, particle size and packed-bed diameter on the economic variables during radiative heating.

- To determine the constants in the economic equation for manufacturing SD castings by batch processes using radiative and induction heating. This requires the determination of thermal history of SD components during heating.

REFERENCES

1. G. Langford and R. E. Cunningham: Met. Trans. B, 1978, Volume 9B, pp. 5-19.
2. D. Apelian and G. Langford: Rapid Cycle Steel Casting. Proposal for research written for the Advanced Research Projects Agency, 1977.
3. R. L. Conta: IEEE Trans. on Industrial Applications, Vol. IA-13, No. 4, pp. 330-334.
4. Kubo et al.: "Molding Unbonded Sand with Vacuum - The V-Process", AFS Transactions, 1973, pp. 529-544.
5. G. Langford: Mater. Sci. Eng., 1977, Vol. 25, p. 275.

Table I. Cycle Time as a Function of Shot Diameter

Shot Diameter mm	Cycle Time s
0.25	130
0.50	525
0.75	1180
1.00	2100
1.25	3280
1.50	4725
1.75	6430

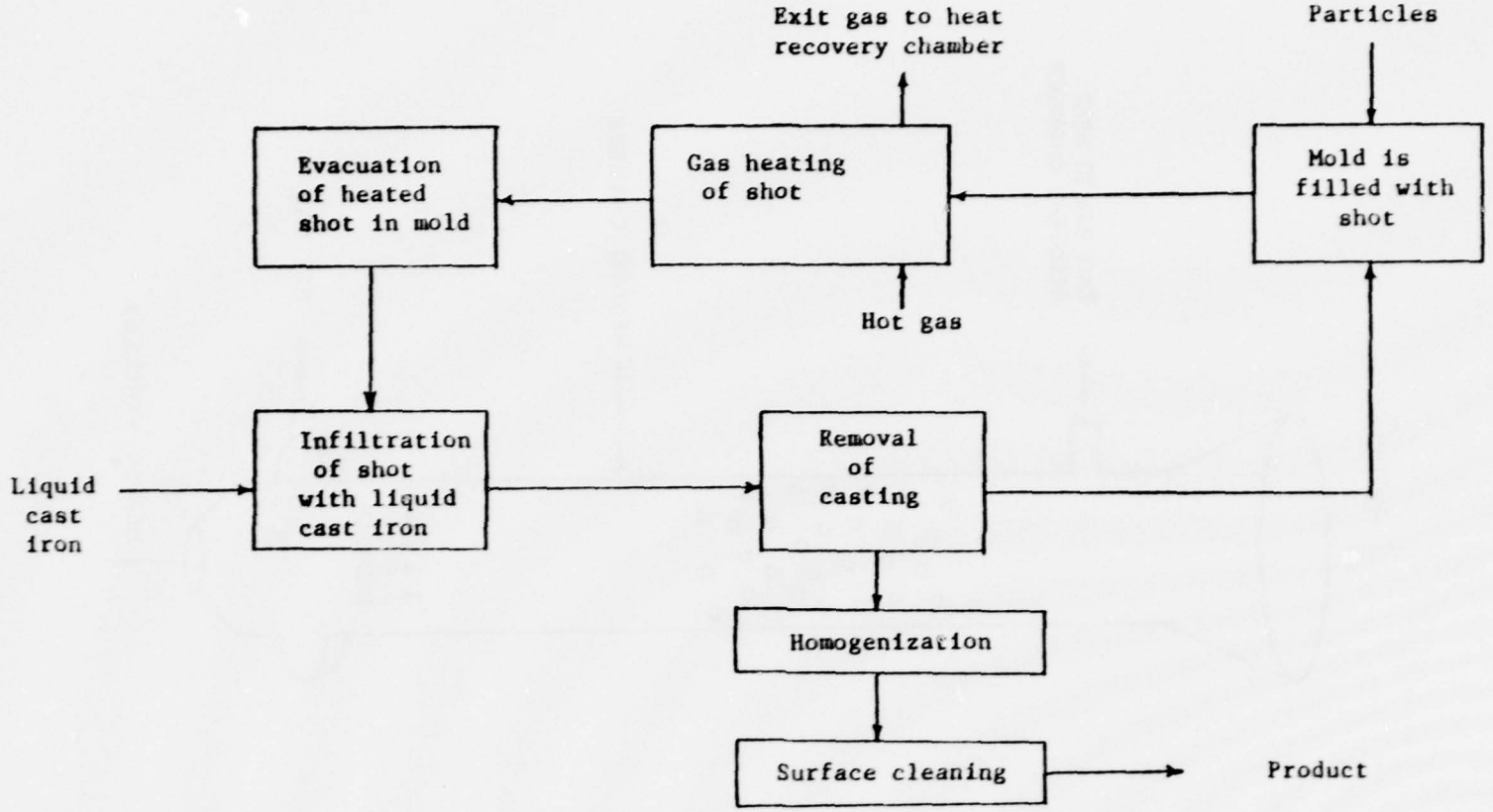

Figure 1. Flow sheet for manufacturing SD castings in permanent molds by gas heating.

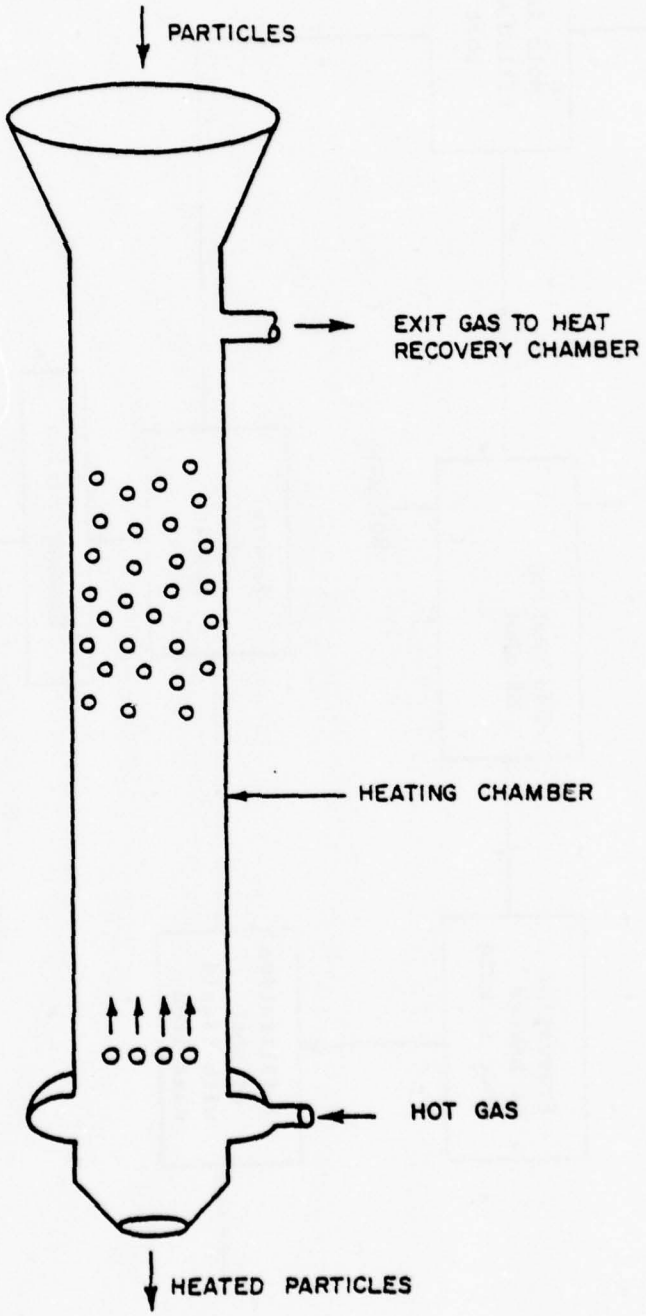

Figure 2. Particles heated individually to process temperatures by hot gas.

Legend

1. induction coils
2. graphite susceptor
3. insulation
4. mold
5. radiation shields
6. cast iron
7. particle valve
8. shot
9. graphite disc

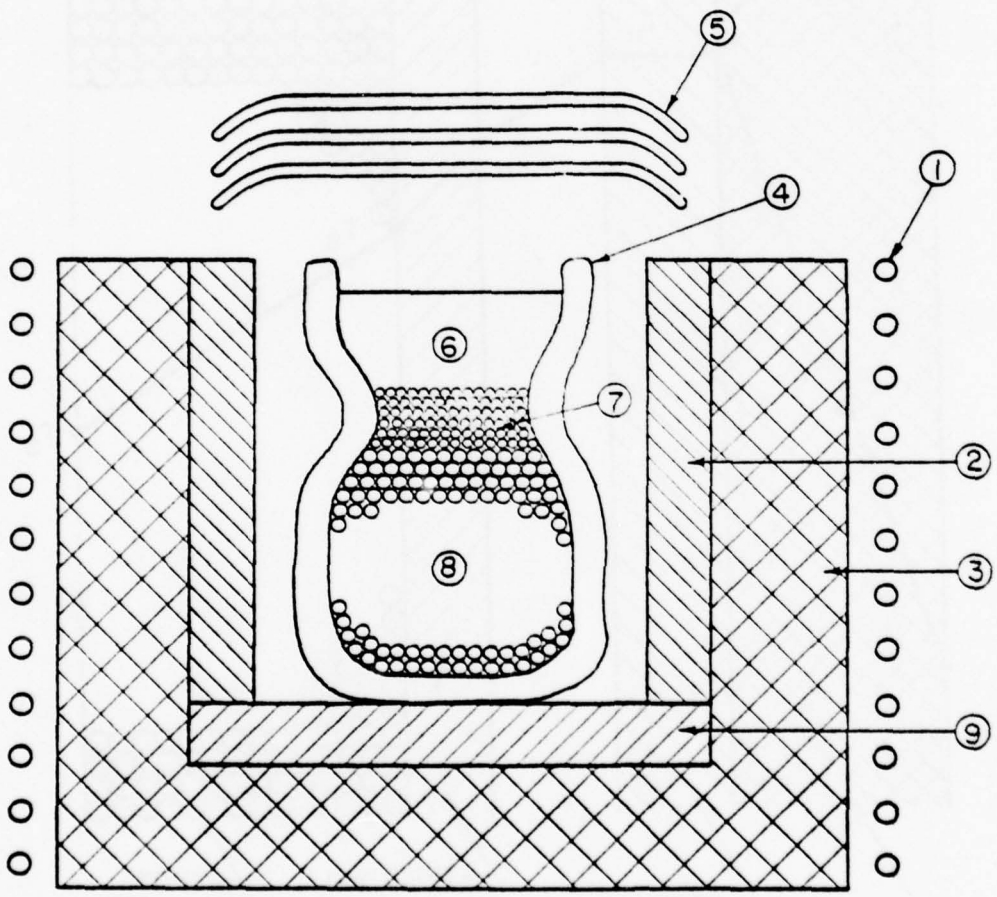

Figure 3. Radiative heating setup for manufacturing SD castings.

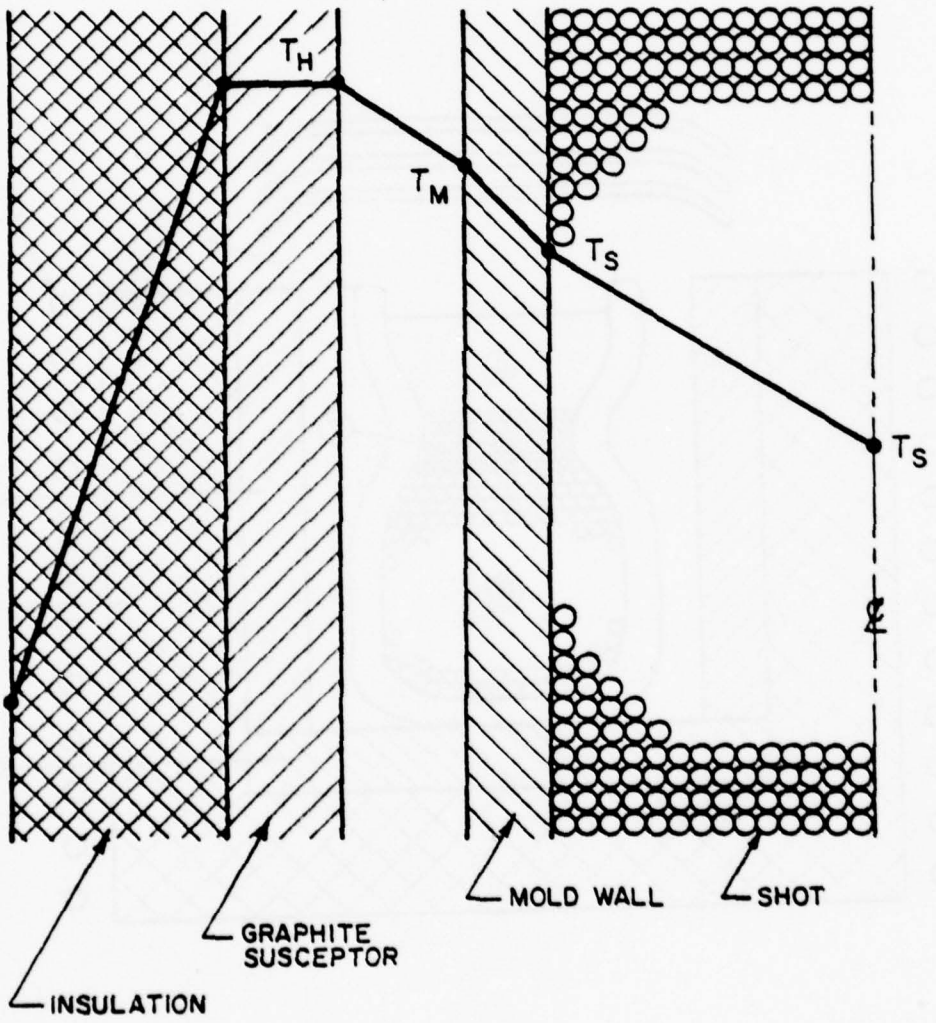

Figure 4. Radial temperature distribution during radiative heating.

APPENDIX II-A: HEATING OF LOW CARBON STEEL PARTICLES BY FORCED GAS INFILTRATION

The flow sheet for the process is shown in Fig. II-A1. The basis considered is a packed bed formed by 1 kg of low carbon steel, spherical particles, 0.50 mm (0.020 in) diameter, to be heated from room temperature to a process temperature of 1400°C. The particles are contained in a cylindrical impermeable mold with a diameter of 60 mm. Argon* gas is used as the heating medium and enters the packed bed at a temperature of 1550°C.

Lower Bound Process Efficiency

The following simplifying assumptions have been made in order to obtain a lower bound in evaluating the efficiency of the process

- The packed bed is well insulated; i.e., the heat losses to the surroundings are negligible.
- There are no temperature gradients in the packed bed. The packed bed has an infinite thermal conductivity.
- The gas leaving the packed bed has a temperature 100°C above the bed temperature.
- The compression of gas approaches isothermal conditions; i.e., PV = const. This is the case when several stages with intercoolers are used.
- Average values of gas and powder properties are used.

Heat Balance

Taking a heat balance around the packed bed, we have**

$$dM_G C_{pg} (T_G - (T + 100)) = m_c C_{pm} dT \qquad [1]$$

* Diatomic N_2 would be better because of its greater heat capacity; H_2 would be better yet (less dense); He is too expensive. Neither N_2 nor H_2 are completely inert with respect to Fe.

** A list of notations used is given at the end of the appendix.

The boundary conditions for the above equation are:

BC1	$t = 0$	$M_G = 0$	$T = T_R = 25°C$
BC2	$t = t_H$	$M_G = M_G$	$T = T_C = 1400°C$

Integrating Eq. [1] using the above boundary conditions we have;

$$M_G = \frac{M_C C_{pm}}{C_{pg}} \ln \left[\frac{T_G - (100 + T_R)}{T_G - (100 + T_C)} \right] \qquad [2]$$

$M_C = 1$ kg $\quad C_{pm} = 567$ J/(kg·K) $\quad C_{pg} = 525$ J/(kg·K)

$T_G = 1550°C \quad T_R = 25°C \quad T_C = 1400°C$

Substituting for the above values in Eq. [2], we have

$M_G = 3.62$ kg of Argon.

Gas Velocity and Mass Flow Rate

Let the heating time be 1000 seconds

$\therefore t_H = 1000$ s

$$V_G = \frac{M_G}{\rho_G} = \frac{3.62 \text{ kg}}{1.78 \text{ kg/m}^3} = 2.03 \text{ m}^3$$

$$\dot{Q}_G = \frac{V_G}{t_H} = 2.03 \times 10^{-3} \text{ m}^3/\text{s} = 0.072 \text{ ft}^3/\text{s}$$

$$v_o = \frac{\dot{Q}_G}{A} = \frac{2.03 \times 10^{-3} \text{m/s}}{\pi/4 \times (0.06)^2} = 0.718 \text{ m/s}$$

Pressure Drop in Packed Bed

The pressure drop through the packed bed is calculated using Ergun's equation, which is valid for turbulent and laminar flow

$$\frac{\Delta P}{L} = \frac{150\ \mu_G v_o (1-\varepsilon)^2}{d_p^{\,2}\ \varepsilon^3} + \frac{1.75\ \rho_G v_o^{\,2}(1-\varepsilon)}{d_p \varepsilon^3} \qquad [3]$$

$\mu_G = 4 \times 10^{-5}$ Pa·s $\qquad \varepsilon = 0.38 \qquad v_o = 0.718$ m/s

$d_p = 5 \times 10^{-4}$ m $\qquad \rho_G = 1.78$ kg/m^3

Substituting for the above values in Eq. [3], we have

$$\frac{\Delta P}{L} = \frac{150 \times 4 \times 10^{-5} \times 0.718 \times 0.62^2}{(5 \times 10^{-4})^2 \times 0.38^3} + \frac{1.75 \times 1.78 \times 0.718^2 \times 0.62}{(5 \times 10^{-4}) \times 0.38^3}$$

$$= 1.56 \times 10^5 \text{ Pa/m}$$

The length of packed bed is given by Eq. [4]

$$\ell_{PB} = \frac{m_c}{\rho_{shot}} \times \frac{1}{(1-\varepsilon)} \times \frac{1}{A} \qquad [4]$$

$$= \frac{1}{7870 \text{ kg/m}^3} \times \frac{1}{0.62} \times \frac{1}{\pi/4 \times (0.06)^2}$$

$$= 0.073 \text{ m}$$

Pressure drop across packed bed

$$\Delta P_{PB} = \left(\frac{\Delta P}{L}\right) \times \ell_{PB} = 1.56 \times 10^5 \times 0.073 = 1.14 \times 10^4 \text{Pa}$$

Compressor Power Requirements

Let the exit gas pressure (P_E) from the packed bed be 1.2 atm (1.2×10^5 Pa). Gas inlet pressure to the packed bed

$$P_I = P_E + \Delta P_{PB} = 1.30 \times 10^5 \text{Pa}$$

Assume that the gas pressure drop in the heat exchanger is equal to the pressure drop across bed

$$\therefore \Delta P_{HE} = \Delta P_{PB}$$

The outlet pressure from gas compressor,

$$P_2 = P_I + \Delta P_{HE} = 1.43 \times 10^5 \text{ Pa}$$

Inlet gas to compressor is at atmospheric pressure,

$$\therefore P_1 = 1.0 \times 10^5 \text{ Pa}$$

When compression cycle approaches isothermal conditions i.e. PV = const., the h.p. of compressor is given by Eq. [5]

$$\text{h.p.} = 0.0044\ P_1 Q_1\ \ell n\ (P_2/P_1) \qquad [5]$$

where,

P_1 - inlet pressure to compressor in psi

P_2 - outlet pressure to compressor in psi

Q_1 - volumetric flow rate in ft^3/min

$$\therefore \text{h.p.} = 0.0044 \times 0.072\ ft^3/s \times 60 s/min \times 14.7\ \ell n \frac{1.43}{1} = 0.100$$

Power rating of compressor = 0.1 h.p. x 746 W/h.p. = 74.6 W

Heat equivalent of work done by compressor,

$$Q_C = 74.6 \text{ W} \times 1000 \text{ s} = 74.6 \text{ kJ}$$

Efficiency of Process

$$\eta = \frac{Q_P}{Q_G + Q_C + Q_L} \qquad [6]$$

where

Q_P = energy required to heat the particles from T_R to T_C

$= m_C\ C_{pm}\ (T_C - T_R) = 1 \times 567 \times (1400-25) = 780$ kJ

Q_C = compression work = 74.6 kJ

Q_L = Heat loss to surroundings = 0

Q_G = heat supplied to gas in heat exchanger

$= m_G C_{pg}(T_G - T_R) = 3.62 \times 525 \times (1550-25) = 2900$ kJ

$$\therefore \eta = \frac{780}{2900 + 74.6} = 26.2\%$$

Using the above procedure the efficiency and power rating of compressor were determined for heating times of 100 and 10 seconds. The results are summarized in Table II-AI.

Upper Bound Process Efficiency

In the above analysis only 27 percent of the gas inlet energy is transferred to the shot irrespective of the gas velocity in the packed bed. The estimation of process efficiency using the second and third assumptions is the lower bound for heating shot by gas. The upper bound process efficiency can be estimated by using the first, fourth and fifth assumptions and assuming that the product of heat transfer coefficient and heat transfer area is infinite; i.e., that the gas rapidly transfers its thermal energy to the packed bed.

Under such circumstances the gas leaves the packed bed a few degrees above room temperature; i.e., the heat exchange efficiency between the gas and packed bed is 100 percent. This assumption permits the gas inlet temperature to be only slightly greater (say, a few °C) than the casting temperature. The quantity of gas required to heat the shot is given by Eq. [7]

$$M_G = \frac{m_C C_{pm}}{P_G C_{pg}} = \frac{1 \times 567}{1.78 \times 525} = 0.60 \text{ m}^3 \qquad [7]$$

The upper bound process efficiency can be calculated using the procedure followed for estimating the lower bound process efficiency. The process efficiency and power rating of the compressor for heating 1 kg of shot in a packed bed in 10, 100 and 1000 seconds is given in Table II-AII.

The actual process efficiency and the quantity of gas required per kg of shot heated must lie between the lower and upper bound estimates. Since no experimental data are available for gas heating of shot at SD casting temperatures (1250°C to 1400°C), we shall consider the average of the lower and upper bounds as the process efficiency and quantity of gas required per kg of shot. The average values for the lower and upper bounds are given in Table II-AIII.

Summary

The economics of heating shot by gas are controlled by three important variables:

- heating time
- power rating of compressor
- efficiency of the process

The heating time influences the production costs: Increasing the power rating of the compressor shortens the heating time, adding to the capital costs, and decreasing the process efficiency.

The heat transfer coefficient between the heating gas and the packed bed has not yet been determined; it may or may not influence the efficiency of the process but cannot be changed except by changing the process. The overall efficiency of shot heating by this technique is on the order of 50%.

NOTATIONS USED IN APPENDIX II-A

M_G - quantity of gas required to heat the packed bed to process temperature

T - temperature of the packed bed at any instant of time during the heating process

T_G - temperature of gas entering the packed bed

T_R - room temperature

T_C - casting temperature

C_{PG} - mean specific heat of gas

C_{pm} - mean specific heat of powders

m_C - weight of particles to be heated

ρ_G - mean density of gas

V_G - volume of gas required to heat up particles to process temperature

t_H - heating time

$\dot{Q}_G$ - volumetric flow rate of gas

v_o - superficial gas velocity through packed bed

A - area of packed bed

d_{PB} - diameter of packed bed

ΔP - pressure drop through packed bed

ℓ_{PB} - length of packed bed

μ - average viscosity of gas

ϵ - void fraction of packed bed

dp - diameter of particles

h.p. - horse power of compressor

η - efficiency of process

Table II-AI Economic Variables for Gas Heating Assuming that the Packed Bed has an Infinite Thermal Conductivity

Heating Time s	Heating Efficiency percent	Power Rating of Compressor kW	Quantity of Gas for Heating 1 kg of Shot m^3
10	18.5	130	
100	25.8	1.3	2.0
1000	26.2	0.075	

Table II-AII Economic Variables for Gas Heating Assuming that the Product of Heat Transfer Coefficient and Heat Transfer Area is Infinity

Heating Time s	Heating Efficiency percent	Power Rating of Compressor kW	Quantity of Gas for Heating 1 kg of Shot m^3
10	31.5	24	
100	98.1	0.15	0.61
1000	98.4	0.010	

Table II-AIII Economic Variables Expected for Heating Shot by Gas

Heating Time s	Heating Efficiency percent	Power Rating of Compressor kW	Quantity of Gas for Heating 1 kg of Shot m^3
10	25.0	82	
100	62.0	0.70	1.3
1000	62.3	0.040	

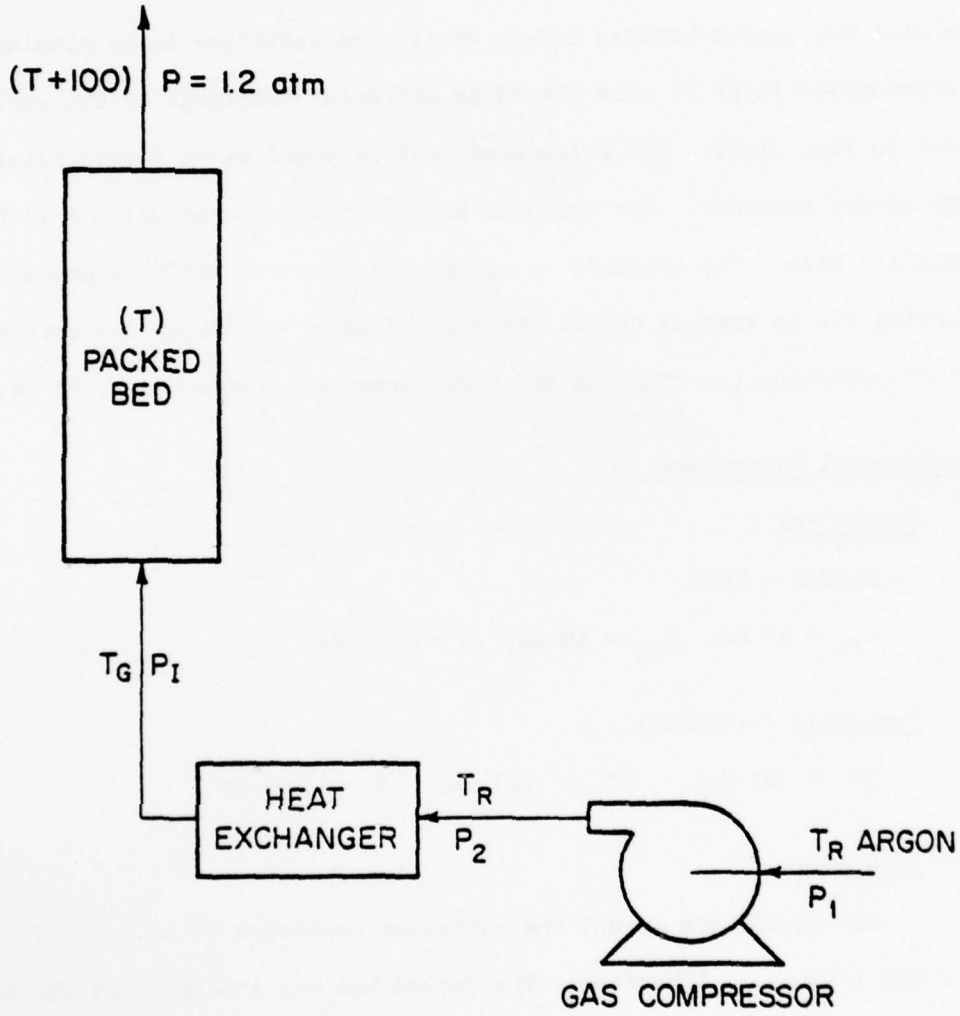

Figure II-A1. Flow sheet for heating particles by forced gas convection.

APPENDIX II-B: RADIATIVE HEATING EXPERIMENTAL RESULTS

Experimental Procedure

The experimental setup for radiative heating is shown in Fig. II-B1. The shot was placed between layers of alumina particles in an alumina crucible. Thermocouples (type W) were placed at different locations in the packed bed as shown in Fig. II-B2. The temperature was recorded using a multipoint Honeywell temperature recorder. The graphite susceptor was heated using a 10 kHz, 25 kW induction unit. The crucible was preheated to about 500°C to prevent it from cracking due to thermal shock. This was done by operating the unit at 1 to 3 kW. After preheating the crucible the power input was increased to 12 kW.

Experimental Parameters

Packed Bed

Powder - RESD

d_{PB} = 67 mm, ℓ_{PB} = 80 mm, W = 1.27 kg

Susceptor (Graphite)

ID = 83 mm, OD = 103 mm, ℓ = 305 mm

Insulation

The insulation around the susceptor consisted of 12.5 mm of graphite felt and 12.5 mm of fiberfrax. The packed bed was insulated at the top by a 50 mm layer of alumina particles and at the bottom by a 100 mm layer of alumina particles.

Crucible (Alumina)

ID = 67 mm, OD = 77 mm, ℓ = 188 mm

Coils

d_C = 9.5 mm, d_S = 165 mm, ℓ_S = 300 mm, N = 11 turns

Results

Fig. II-B2 shows the temperature distribution in the packed bed as a function of time. The packed bed heats uniformly in the longitudinal direction. Large radial temperature gradients (600°C to 900°C) are observed for a period of 1500 seconds. During this period the interior temperature increased by 200°C. After 1500 seconds the interior temperature rapidly increased. A heating time of about 2200 seconds was required to attain a uniform packed bed temperature of 1350°C. The heating efficiency was 4.2 percent.

The crucible showed no signs of cracks. The particles in the bed had sintered together. The packed bed surface was uniform and showed no signs of cracks.

LEGEND

1. induction coils
2. fiberfrax
3. graphite felt
4. graphite susceptor
5. alumina crucible
6. graphite disc
7. pyrolytic graphite
8. alumina particles
9. shot

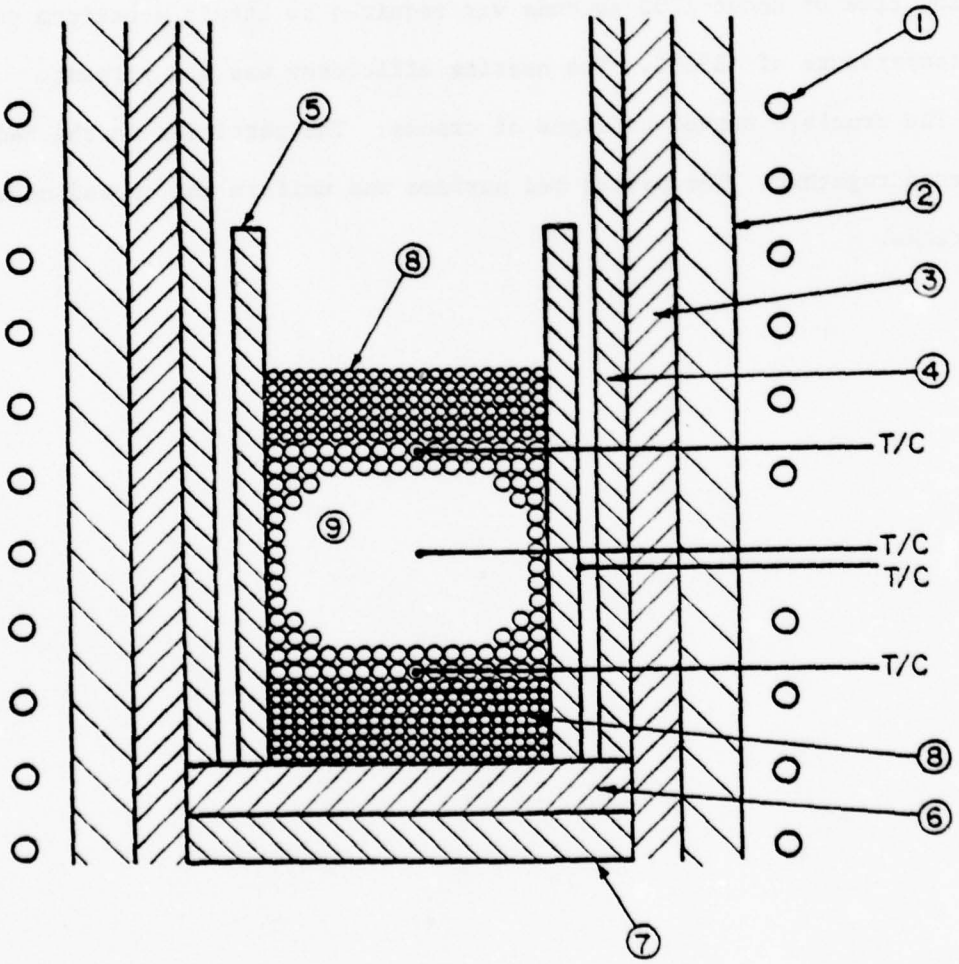

Figure II-B1. Radiative heating setup.

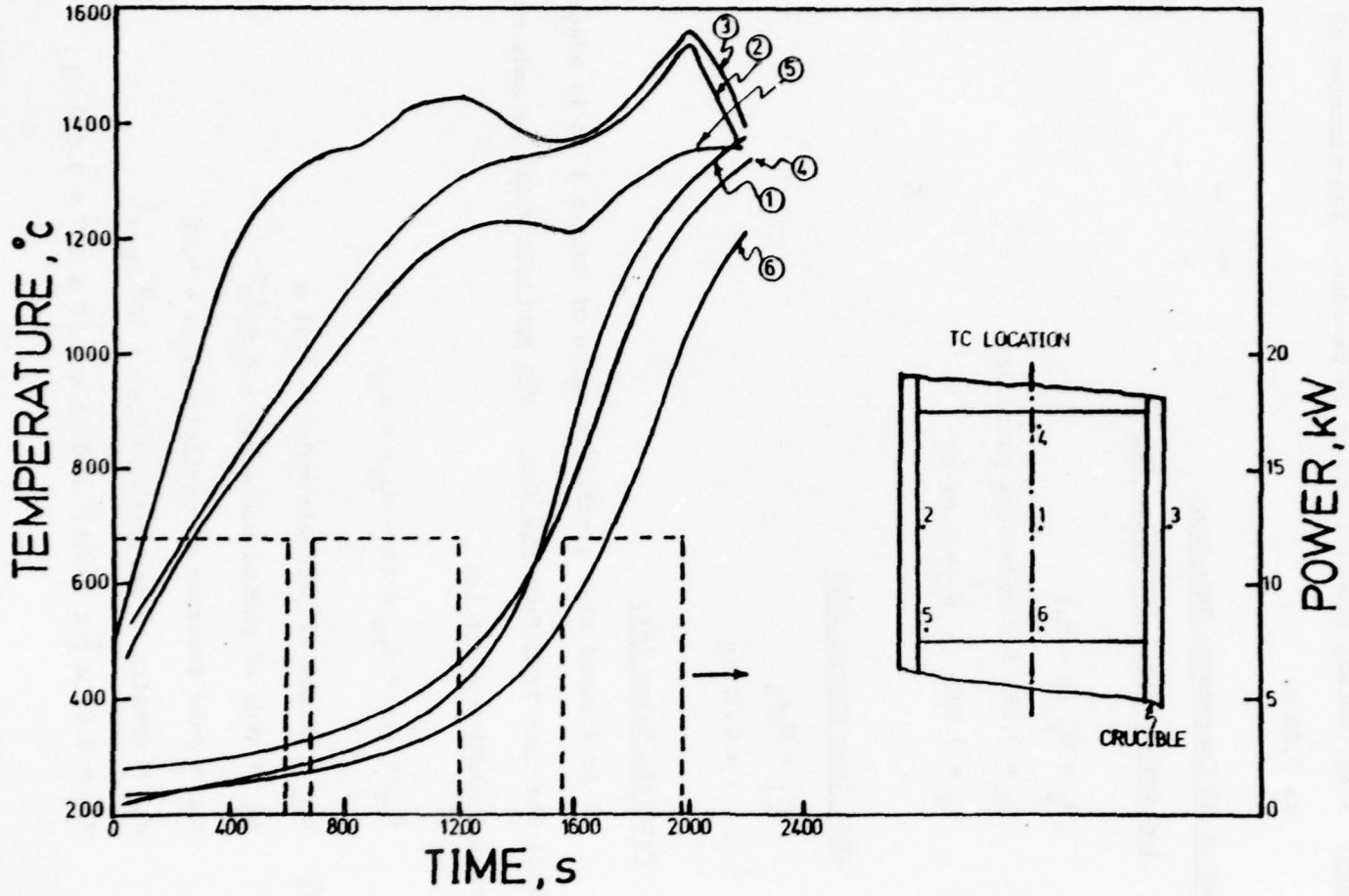

Figure II-B2. Temperature distribution in packed bed during radiative heating.

APPENDIX II-C: ENERGY REQUIREMENTS FOR MANUFACTURING SD CASTINGS USING A BATCH PROCESS

Basis: 1 kg casting manufactured by SD process. The diameter of casting is 0.06 m.

Mass of SD Components Required:

Low Carbon Steel Particles (Shot)

$$W_S = W_T (1 - \varepsilon_S) \quad [1]$$

$\varepsilon_S = 0.38$ for spherical particles

$W_T = 1$ kg, $W_S = 0.62$ kg

Cast Iron Charge (CI)

$$W_{CI} = W_T \varepsilon_S \quad [2]$$

$= 0.32$ kg

Particle Valve (PV)

It is assumed that a particle valve of height 1 cm is adequate to isolate the cast iron from the shot. The particle valve is made up of spherical alumina particles

$$W_{PV} = h_{PV} \times A_{PB} \times (1 - \varepsilon_{PV}) \times \rho_{PV} \quad [3]$$

where h_{PV} = height of particle valve = 0.01 m

A_P = area of packed bed = $\pi/4 \times 0.06^2 m^2$

ε_{PV} = void fraction of particle valve = 0.38

ρ_{PV} = density of particles = 3.99×10^3 kg/m^3

$W_{PV} = 0.01 \times \frac{\pi}{4} \times (0.06)^2 \times 0.38 \times 3.99 \times 10^3 = 0.070$ kg

Theoretical Energy Requirements for Making a 1 kg SD Casting Using a Direct Technique

Energy requirements will be calculated for heating the charge components

from room temperature to a process temperature of 1400°C:

Cast Iron

$$E_{CI} = W_{CI} \{C_{PI}(T_P - T_R) + \Delta H_m\} \quad [4]$$

where

C_{PI} = Average specific heat of CI = 600J/(kg·K)

T_P = Process temperature

T_R = Room temperature

ΔH_m = Heat of fusion = 273 kJ

$\therefore E_{CI} = 0.38 \{0.600 (1400 - 25) + 273\} = 417$ kJ

Shot

$$E_S = W_S C_{PS} (T_P - T_R) \quad [5]$$

$= 0.62 \times 0.600 \times (1400 - 25) = 512$ kJ

Particle Valve

$$E_{PV} = W_{PV} C_{PV} (T_P - T_R) \quad [6]$$

$C_{PV} = 0.84$ kJ/kg·K)

$E_{PV} = 0.07 \times 0.84 \times (1400 - 25) = 81$ kJ

Table II-CI summarizes the energy requirements for making a 1 kg casting.

Energy Considerations for Manufacturing a SD Casting by Indirect Heating

During indirect heating, the heat must be transported across a surface. The energy density (energy per unit area) controls the transport of heat and is given by Eq. [7]

Q_1 = Energy required to heat the charge to process temperature/ surface area available for heat transport

$$= E_L / (\frac{\pi}{4} \times \frac{d_{PB}}{2} \times h_i) \quad [7]$$

where

E_i = Energy required for the i^{th} component

h_i = Height of i^{th} component in mold

Height of Charge Components in Mold

Cast Iron

$$h_{CI} = \frac{W_{CI}}{\rho_{CI}} \times \frac{1}{(1 - \varepsilon_{CI})} \times \frac{1}{A_{PB}} \qquad [8]$$

ε_{CI} = packing factor of cast iron charge = 0.5

$$h_{CI} = \frac{0.38}{7.87 \times 10^3} \times \frac{1}{(1 - 0.5)} \times \frac{1}{\pi/4 \times 0.06^2} = 0.034 \text{ m}$$

Particle Valve

h_{PV} = 0.01 m

Shot

$$h_S = \frac{W_S}{\rho_S} \times \frac{1}{(1 - \varepsilon_S)} \times \frac{1}{A_{PB}} \qquad [9]$$

$$h_S = \frac{0.62}{7.87 \times 10^3} \times \frac{1}{(1 - 0.38)} \times \frac{1}{\pi/4 \times 0.06^2} = 0.045 \text{ m}$$

Energy Density Requirements to Heat the Components to a Process Temperature of 1400°C:

Cast Iron

$$Q_{CI} = \frac{E_{CI}}{\pi \times \frac{d_{PB}}{2} \times h_{CI}} = \frac{417}{\pi \times 0.03 \times 0.034} = 130 \text{ J/mm}^2$$

Particle Valve

$$Q_{PV} = \frac{E_{PV}}{\pi \times \frac{d_{PB}}{2} \times h_{PV}} = \frac{81}{\pi \times 0.03 \times 0.01} = 85 \text{ J/mm}^2$$

Shot

$$Q_S = \frac{E_S}{\pi \times \frac{d_{PB}}{2} \times h_S} = \frac{512}{\pi \times 0.03 \times 0.045} = 120 \text{ J/mm}^2$$

The results for energy requirements using an indirect method are summarized in Table II-CII. The difference in the energy density for the SD components can be minimized by changing the packing density of the casting iron charge and particle valve.

Table II-CI. Theoretical energy considerations for manufacturing a 1 kg SD casting by a direct heating method.

SD Charge Component	Mass of Component kg	Energy Required kJ
Cast Iron	0.38	417
Particle Valve	0.07	81
Shot	0.62	512

Table II-CII. Theoretical energy density considerations for manufacturing a 1 kg SD casting by an indirect heating method.

SD Charge Component	Mass of Component kg	Height in Mold mm	Energy Density J/mm^2
Cast Iron	0.38	34	130
Particle Valve	0.07	10	85
Shot	0.62	45	120

APPENDIX II-D: INDUCTION HEATING EXPERIMENTAL RESULTS

The appendix summarizes the experimental results of induction heating of steel powders. The relationships and notations used for evaluating the data are given at the end of the appendix.

Experimental Procedure

The particles were placed in a crucible insulated with fiberfrax*, a light weight thermal insulation made from alumina-silica fibers. An alumina tube, 6.35 mm (0.25 in) in diameter was placed in the center of the packed bed to maintain an inert atmosphere to minimize the oxidation of the particles during the heating period. Power was supplied to the particles through an induction coil closely surrounding the crucible. Thermocouples were placed at different locations in the packed bed. Temperatures were recorded using a multipoint Honeywell temperature recorder. Figs. II-D1, II-D2 and II-D3 show the different setups used for evaluating the induction heating characteristics of steel powders. The setup shown in Figs. II-D1 and II-D2 were used to evaluate the induction heating characteristics of low carbon steel powders. The setupt shown in Fig. II-D2 was also used to measure the resistivity of the packed bed as a function of temperature. The setup shown in Fig. II-D3 was used to study the induction heating characteristics of preheated powders. These particles were preheated by indirect resistance heating.

Experimental Parameters

The important experimental parameters for direct induction heating of steel particles are listed below:

- Powder
- Setup

---

* Registered Trade Mark and Product of the Carborundum Company.

- Packed bed
- Coil
- Resistivity leads
- Thermocouples
- Insulation
- Atmosphere
- Induction unit

The values for the experimental parameters are given in Table II-DI. Appendix II-H gives the characteristics of powders listed in Table II-DI. A cylindrical packed bed geometry was used in all the induction heating runs. The packed bed resistivity was measured using a four point technique. Tungsten wire, 0.25 mm (0.01 in) diameter, was used for the voltage and current leads. The crucible containing the particles was insulated from the surroundings with fiberfrax. A Taylor Winfield, 450 kHz, 10 kW radio frequency generator* was used to heat the particles in run #9. In the other runs, the particles were heated using an Inductotherm, 4.2 kHz, 30 kW audio frequency generator.

Results

The induction heating of low carbon spheroidal powders will be discussed with emphasis to the following factors:

- temperature distribution in packed bed
- incubation-period phenomena
- maximum packed bed temperature
- heating time
- heating efficiency
- resistivity

---

* The authors are indebted to the staff of the Laboratory for the Research for the Structure of Matter, University of Pennsylvania, for allowing us to use this equipment.

- reheating of packed bed
- packed bed after heating
- preferential coupling
- suppression of induction flux.

Temperature Distribution in Packed Bed

The temperature distribution in the packed bed was evaluated by recording the temperature at different locations as a function of time. The maximum longitudinal and radial gradients observed for the heating runs are listed in Table II-DII.

In audio frequency (4.2 kHz) induction heating, the radial temperature gradients were small in magnitude. Fig. II-D4 shows the temperature distribution in run #6. The packed bed heats uniformly in the radial direction. At audio frequencies large longitudinal gradients were observed during heating. The temperature at the middle part of the packed bed always exceeded the temperatures at the top and bottom of the bed. The temperature-time data for run #6, shown in Fig. II-D4, is an example of the longitudinal temperature gradients observed in the packed bed during induction heating. The longitudinal temperature gradients could be minimized by appropriate variation of the local coil spacing along the packed bed. This was done in run #7 and the results are shown in Fig. II-D5. The temperature of the top of the bed was considerably lower than the rest of the bed. The low concentration of coil turns at the top of the bed accounted for this temperature difference. Experimental results indicated that longitudinal temperature gradients could be minimized if three to four coil turns were concentrated at the top and bottom of the packed bed.

At radio frequencies (450 kHz) large radial temperature gradients were observed. No attempt was made to study the longitudinal temperature gradients during radio frequency heating. The results of induction heating at 450 kHz are shown in Fig. II-D6 (run #9).

Incubation Period Phenomena

An incubation period was observed during the heating of low carbon spheroidal steel particles. The incubation period was characterized by a low packed bed heating rate. The duration of the incubation period depends on the power input to the charge, the packed bed temperature and the particles in the bed. The incubation period was short-lived at high power inputs. The influence of high power inputs on the incubation period could not be studied due to the rapid change in load-coupling characteristics of the packed bed with temperature.

The coupling temperature represents the temperature at which there is a sudden increase in the heating rate. This temperature is influenced by the particles and the frequency of induction heating. If the coupling temperature exceeded the Curie temperature for iron (771°C), then the packed bed could not be heated above the Curie temperature regardless of the power input density to the charge. The incubation period results are given in Table II-DII.

The incubation period could be circumvented if the packed bed was preheated to the coupling temperature. The induction heating characteristics of preheated RESD powder was studied in runs #13 and 14. The packed bed was preheated to 350°C in run #13, about 75°C below the coupling temperature for RESD powder. The incubation period was cut down to 250 seconds. The particles were preheated to 425°C in run #14. At this temperature, no incubation period was observed, as shown in Fig. II-D7.

Maximum Packed Bed Temperature

Once the packed bed coupled to the induction flux, then SD casting temperature could be easily attained. On the other hand, heavily oxidized particles did not couple to the induction flux. For these particles the maximum attainable temperature was 771°C as shown in Fig. II-D8 for STLD powder. The maximum temperatures attained in the packed bed for the induction heating runs are given in Table II-DII.

Heating Time

The heating time is defined as the time to raise the packed bed to SD casting temperature after the packed bed coupled to the induction flux. At high power levels, using a manual induction unit, heating times of 300 seconds were observed. The heating times for the different runs are given in Table II-DII.

Heating Efficiency

The heating efficiency for the experimental runs is given in Table II-DII. Small size particles (RESD powder) were heated from the coupling temperature to process temperature at efficiencies of 10 to 15 percent. Larger size particles (STLDDO powders) could be heated from room temperature at efficiencies of 6 to 7 percent.

Resistivity of Packed Bed

The resistivity of RESD powder was measured as a function of temperature in runs #7 and 10. The results are given in Fig. II-D9.

Reheating of Packed Bed

After heating the packed bed to process temperatures and then cooling it to room temperature, it could be reheated to SD casting temperatures in about 300 seconds at heating efficiencies of 20 to 30 percent. In this case no incubation period was observed. Fig. II-D10 shows the temperature-time history for packed bed reheating in run #5.

Packed Bed After Heating

The particles in the packed bed had sintered together when SD casting temperatures were attained. The packed bed had oxidized in certain areas. In most runs, longitudinal cracks propagating radially and radial shrinkage at the center of the packed bed were observed. Fig. II-D11 shows the packed bed after

heating for run #10. At high power inputs the cracking phenomena could be avoided. Fig. II-D12 shows the packed bed after heating for run #5. In this case no cracks were observed. The cracking mechanism during induction heating of particles in a bed is discussed in Appendix II-I.

Preferential Coupling

The aim of run #15 was to determine if the cracks observed in the packed bed could be avoided by placing a weight on top of the packed bed. The weight was in the form of a thin carbon steel disc above which ceramic blocks were placed. A number of slots were cut in the disc to reduce its tendency to couple to the induction flux.

It was found that nearly all the power supplied was dissipated in the steel disc, resulting in melting of the disc and top portion of the packed bed. The packed bed remained relatively inert to the induction flux, even above the coupling temperature. The packed bed was heated by transport of heat from the disc. Fig. II-D13 shows the temperature-time history for run #15.

Suppression of Induction Flux

In run #16, a weight inert to the induction flux was placed on top of the bed. The weight considerably retarded the induction heating characteristics of the packed bed. Even at power inputs of 10 kW, the maximum temperature attained in the packed bed was only 780°C. On removal of a part of the weight the packed bed temperature could be raised to 1200°C. Fig. II-D14 gives the temperature-time results for run #16.

Discussion

During IH (induction heating) of low carbon steel particles, the heat is generated in the bed by electrical resistance and magnetic hysteresis losses. The resistance losses result from the induced currents in the load. The hysteresis losses result from the influence of an alternating magnetic field on

the load. Above the Curie temperature (771°C for iron) the hysteresis phenomenon within individual particles is absent and the packed bed can be heated only by resistance losses between particles.

The incubation period encountered during the IH of particles is attributed to the high packed bed resistivity. The resistivity is controlled by three different phenomena: adsorbed gases at low temperatures (100 to 200°C), sintering by neck growth at high temperatures (above 1000°C) and surface oxide at intermediate temperatures. The adsorbed gases on the particles account for the non-conducting nature of the packed bed at low temperatures. A non-conducting charge can be heated only by hysteresis losses since they involve motion of magnetic domains within the isolated particle. Once the gases are desorbed, the resistivity is controlled by the oxide surface layer on the particles. If the oxide layer is small as in the case of RESD powder, the packed bed begins to conduct electricity at about 400°C. Heavily oxidized powder, STLD, causes the packed bed to remain non-conducting even at the Curie temperature. In this case the bed can be heated only up to the Curie temperature. During the incubation period the packed bed is non-conducting and can be heated only by hysteresis losses within each individual particle. The incubation period can be prolonged by placing an inert (ceramic) weight on top of the bed. The weight restrains electrical contact of the particles in the direction of the electrical field permitting heat generation in bed only by hysteresis losses up to the Curie temperature. A metallic conductor whose size is large compared to the individual particles is preferentially coupled by the induction flux. The lower resistivity of the conductor permits large I^2R resistance losses in it compared to the packed bed.

At audio frequency IH, the high packed bed resistivity (0.001 ohm · m) accounts for the depth of penetration being greater than the radius of the charge, resulting in uniform heating of the bed in the radial direction. At

radio frequencies, the depth of penetration is less than the radius of the bed. The interior of the packed bed is heated by conduction and radiation from the zone where heat is generated by resistance losses.

NOTATIONS USED IN APPENDIX II-D

P_t - total power input from induction unit

P_ω - power utilized in heating charge

η_{IP} - IH efficiency during incubation period

η_H - IH efficiency after packed bed couples to the induction flux

d_{PB} - diameter of packed bed

ℓ_{PB} - height of packed bed

W - weight of particles in packed bed

d_C - coil diameter (tubing)

d_S - coil diameter (solenoid)

S - spacing between coil turns

g - gap (distance between coil and charge)

ℓ_S - length of coil

N - number of coil turns

Z - longitudinal direction; Z = 0 top of packed bed

r - radial direction

Z_{CT} - location of the top coil turn on the Z axis

Z_{BT} - location of the bottom coil turn on the Z axis

TC - thermocouple

K - Alumel/chromel TC

W - Tungsten 5% Rhenium/Tungsten 26% Rhenium TC

t_{IT} - thickness of insulation at the top of the packed bed

t_{IR} - radial insulation thickness

t_{IB} - bottom insulation thickness

ℓ_{VL} - distance between voltage leads

ℓ_{CL} - distance between current leads

T - temperature

ΔT_L - maximum longitudinal temperature gradients in bed

ΔT_R - maximum radial temperature gradients in bed

T_{CT} - coupling temperature

T_{MAX} - maximum temperature attained in the packed bed

θ - time

θ_{IP} - incubation period

θ_H - heating time

ρ_{PB} - resistivity of packed bed

R - resistance between voltage leads

Relationships used for evaluating data

A. Efficiency

$$\eta = \frac{P_W}{P_t} \times 100$$

B. Packed bed resistivity

$$\rho_{PB} = R \times \frac{\pi}{4} \times d_{PB}^2 \times \frac{1}{\ell_{VL}}$$

Table II-DI. Experimental Parameters for Induction Heating Runs

			Packed Bed			Coils					
Run #	Powder	Setup	d_{PB} mm	ℓ_{PB} mm	W kg	d_C mm	d_S mm	ℓ_S mm	S mm	g mm	N mm
1	WAVS	Fig. 1	68	188	3.50	6.35	130	150	15	31	9
2	STSD	Fig. 1	77	100	2.00	6.35	130	155	17	27	9
3	STSDDO	Fig. 1	77	90	1.80	6.35	130	110	10	27	9
4	RESD	Fig. 1	77	83	1.70	6.35	130	125	10	27	9
5	RESD	Fig. 1	63	130	1.60	6.35	130	150	16	34	9
6	RESD	Fig. 2	55	130	1.50	6.35	130	150	15	38	9
7	RESD	Fig. 2	55	120	1.40	6.35	130	205	35	38	9
8	RESD	Fig. 2	58	80	1.00	6.35	100	120	8	21	13
9	RESD	Fig. 2	57	80	1.00	6.35	100	120	8	21	13
10	RESD	Fig. 2	58	80	0.92	6.35	100	120	8	21	13
11	STLD	Fig. 2	60	80	0.75	6.35	100	120	8	21	13
12	RESD	Fig. 3	50	80	0.70	6.35	130	220	25	40	9
13	RESD	Fig. 3	58	80	1.00	9.50	110	165	16	25	10
14	RESD	Fig. 3	60	80	1.00	9.50	110	165	16	25	10
15	RESD	Fig. 2	60	75	0.95	9.50	110	165	16	25	10
16	RESD	Fig. 2	60	85	1.20	9.50	110	165	16	25	10
17	STLDDO	Fig. 2	60	80	0.90	9.50	110	165	16	25	10
18	STLDDO	Fig. 2	60	85	1.10	9.50	110	165	16	25	10

Table II-DI (Continued)

Run #	Coil Placement		Resistivity Leads		Thermocouples		Insulation			Heating Atmosphere	Induction Heating Frequency kHz
	Z_{CT} mm	Z_{CB} mm	ℓ_{VL} mm	ℓ_{CL} mm	Type	Number	t_{IT} mm	t_{IR} mm	t_{IB} mm		
1	8	160	-	-	K	4	0	5	15	Air	4.2
2	-43	110	-	-	K	4	75	17	30	Air	4.2
3	-31	80	-	-	K	4	40	17	55	Nitrogen	4.2
4	-17	85	-	-	K	4	45	17	75	Nitrogen	4.2
5	-30	120	48	63	W	2	40	18	40	Argon	4.2
6	-	-	19	68	W	8	35	20	40	Argon	4.2
7	-25	180	34	69	W	8	35	20	40	Argon	4.2
8	-20	100	-	-	W	4	35	19	80	Air	4.2
9	-20	100	-	-	W	2	55	15	40	Air	450
10	-20	100	50	70	W	4	45	14	80	Argon	4.2
11	-20	100	-	-	W	4	45	12	65	Argon	4.2
12	-50	170	-	-	W	4	55	15	45	Argon	4.2
13	-35	130	-	-	W	4	45	15	65	Argon	4.2
14	-35	130	-	-	W	4	45	15	65	Nitrogen	4.2
15	-35	130	-	-	W	4	45	15	65	Nitrogen	4.2
16	-35	130	-	-	W	4	45	15	65	Nitrogen	4.2
17	-35	130	-	-	W	4	45	15	65	Nitrogen	4.2
18	-35	130	-	-	W	4	45	15	65	Nitrogen	4.2

Table II-DII. Experimental Results of Induction Heating Runs

Run #	Temperature Gradients		Incubation Period				Heating Efficiency	Heating Time	Maximum Temperature
	ΔT_L °C	ΔT_R °C	P_I kW	θ_{IP} S	T_{CT} °C	η_{IP} %	η_H %	$\theta_{H,S}$	T_{MAX} °C
1	160	60	5	1300	340	11.2	20.4	-	890
2	180	70	-	-	>771	9.4	-	-	771
3	330	60	5	-	>771	7.4	5.2	-	1115
4	426	200	5	1250	426	7.2	19.6	-	1000
5	-	120	7.5	1280	460	6.0	7.8	300	1350
6	650	100	-	-	-	-	-	-	1400
7	700	30	-	-	450	9.2	6.5	800	1440
8	300	-	5.0	900	490	7.1	13.9	1000	1320
9	-	520	6.8	540	300	4.6	-	-	940
10	200	-	-	-	-	-	-	-	1450
11	30	-	-	-	>771	-	-	-	771
12	400	100	-	-	-	-	-	-	1200
13	220	-	-	250	420	-	13.2	750	1400
14	740	-	-	-	-	-	16.2	300	1400
15	1100	-	-	-	-	-	-	-	>1540
16	300	-	-	-	>771	-	-	-	780
17	580	-	-	-	-	-	6.0	1400	1420
18	280	-	-	-	-	-	7.2	1100	>1540

Legend

1. induction coils
2. crucible
3. fiberfrax
4. alumina tube
5. shot

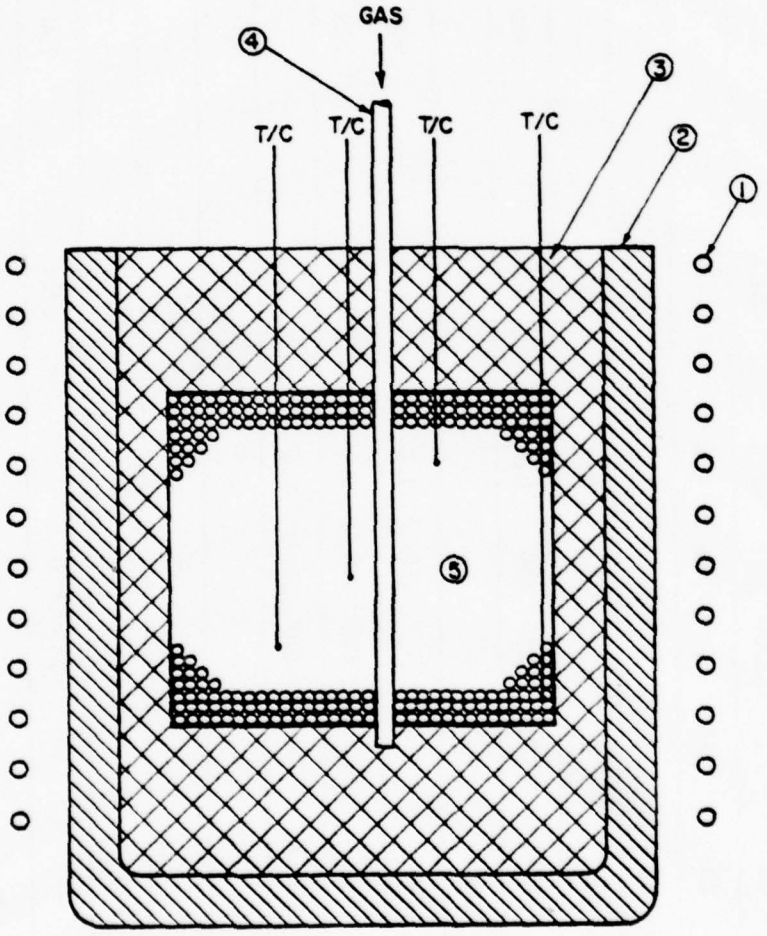

Figure II-D1. Induction heating setup with vertical insertion of thermocouples.

Legend

1. induction coils
2. alumina crucible
3. fiberfrax
4. graphoil gasket
5. current leads
6. voltage leads
7. shot
8. alumina tube

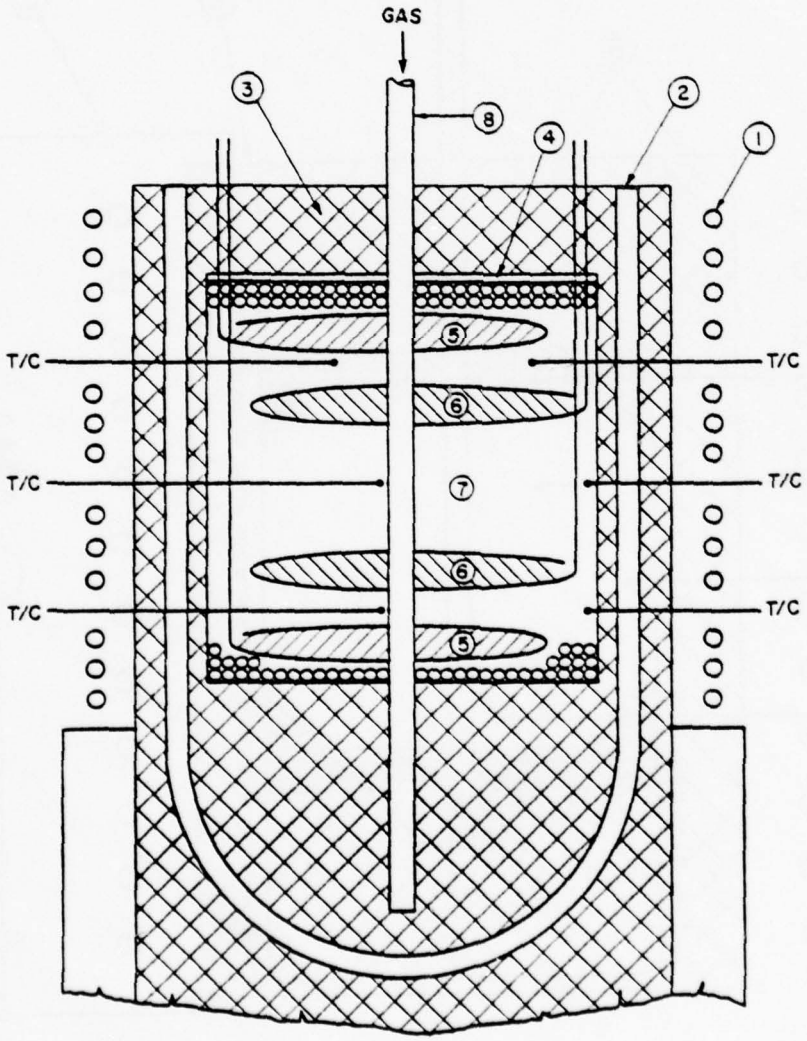

Figure II-D2. Induction heating and resistivity measurement setup with radial insertion of thermocouples.

Legend

1. induction coils
2. silica crucible
3. fiberfrax
4. nichrome wire
5. variable resistor
6. ammeter
7. shot

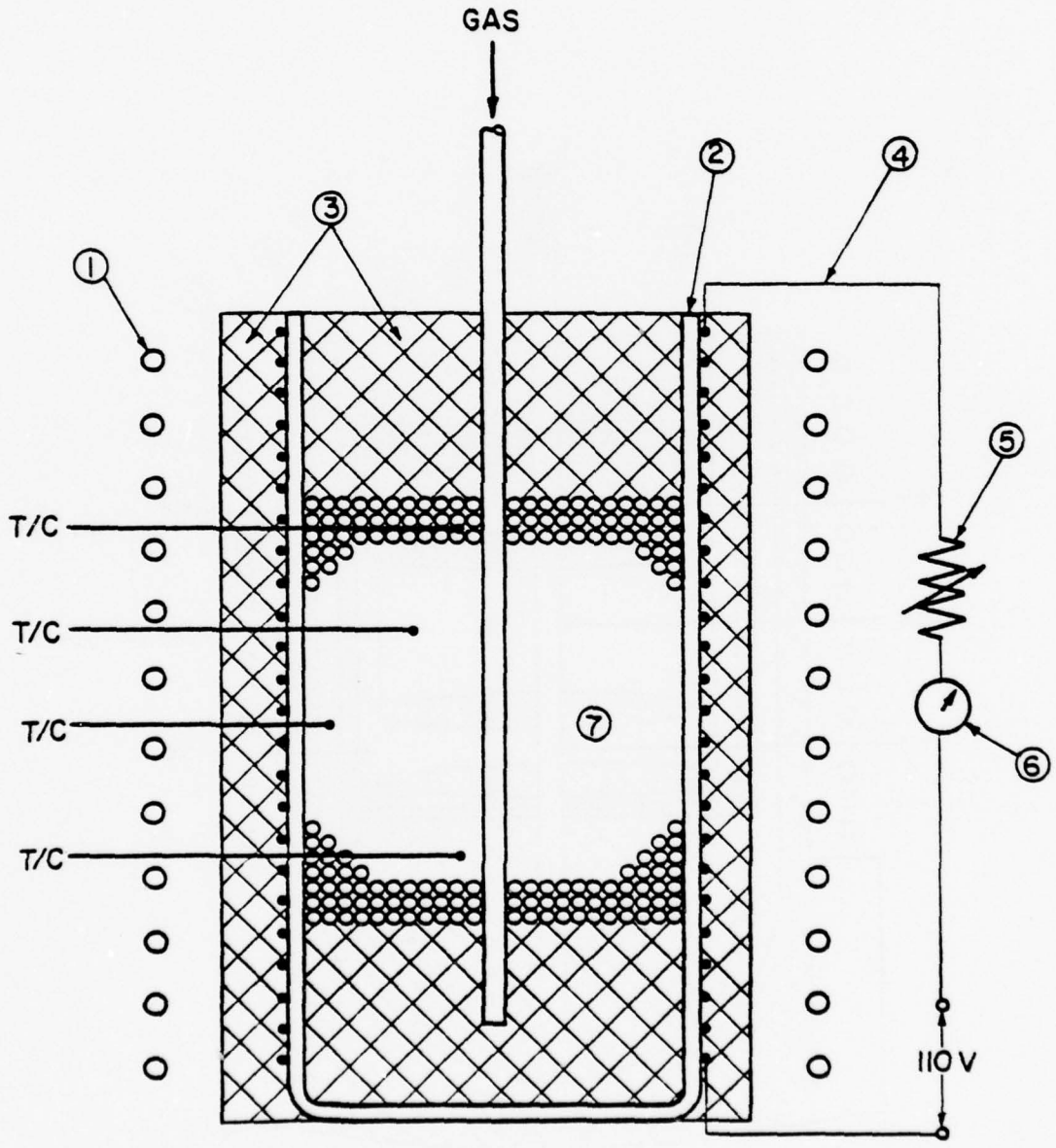

Figure II-D3. Induction heating setup for heating powders preheated by resistance heating.

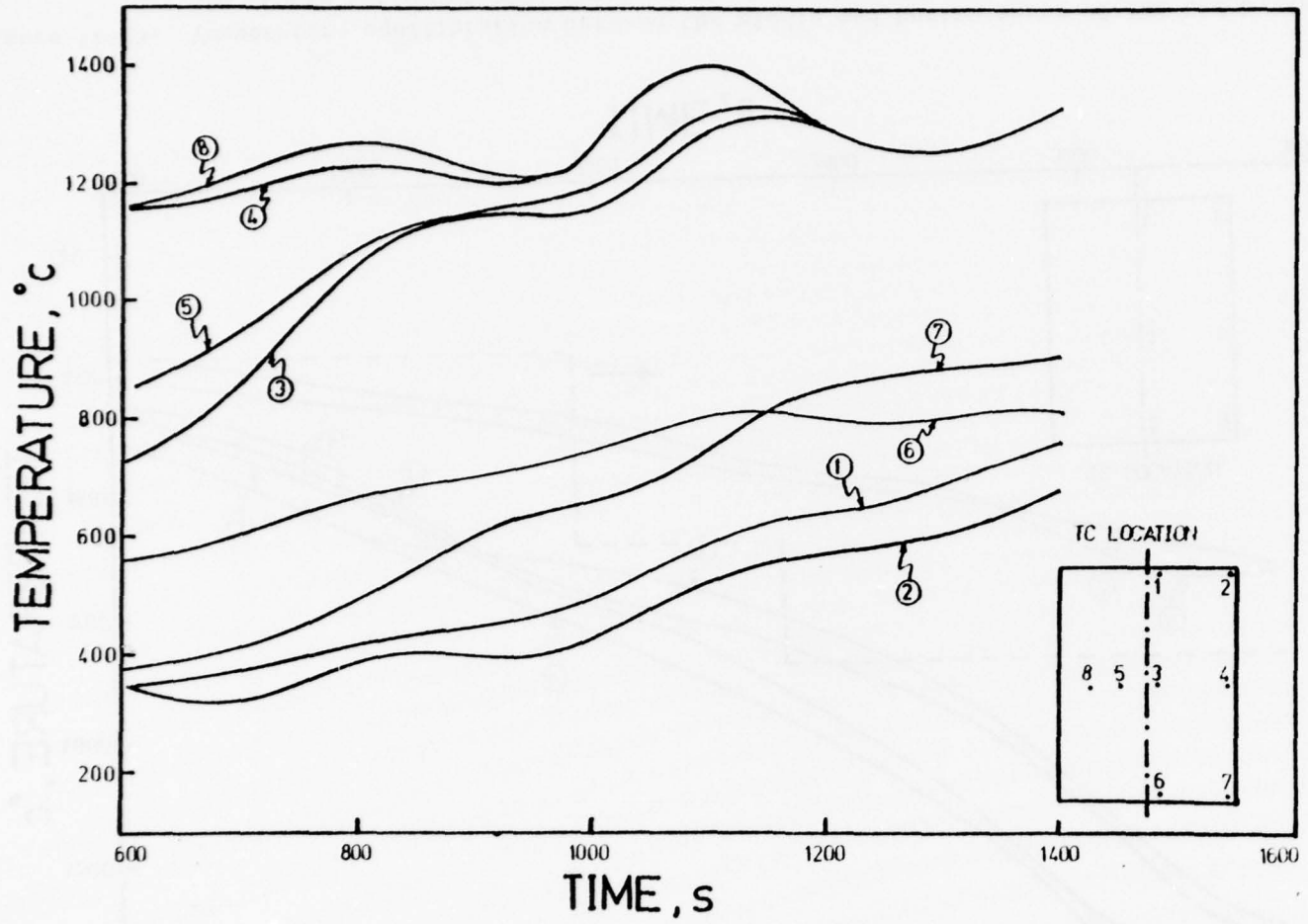

Figure II-D4. Thermal history for run #6 showing longitudinal and radial gradients in bed.

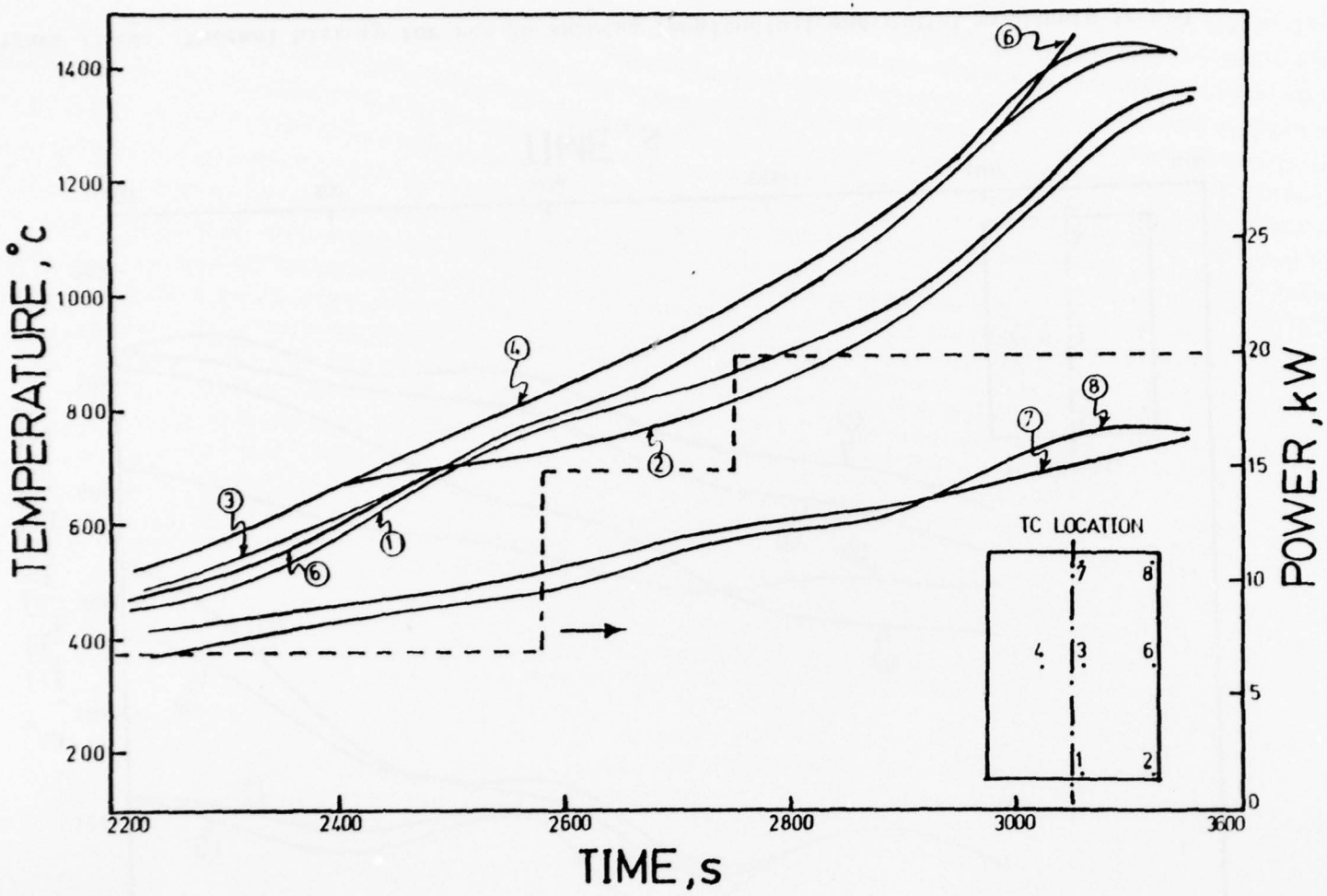

Figure II-D5. Temperature equilibration between the middle and bottom parts of the bed by increasing the concentration of coil turns at the bottom of the bed.

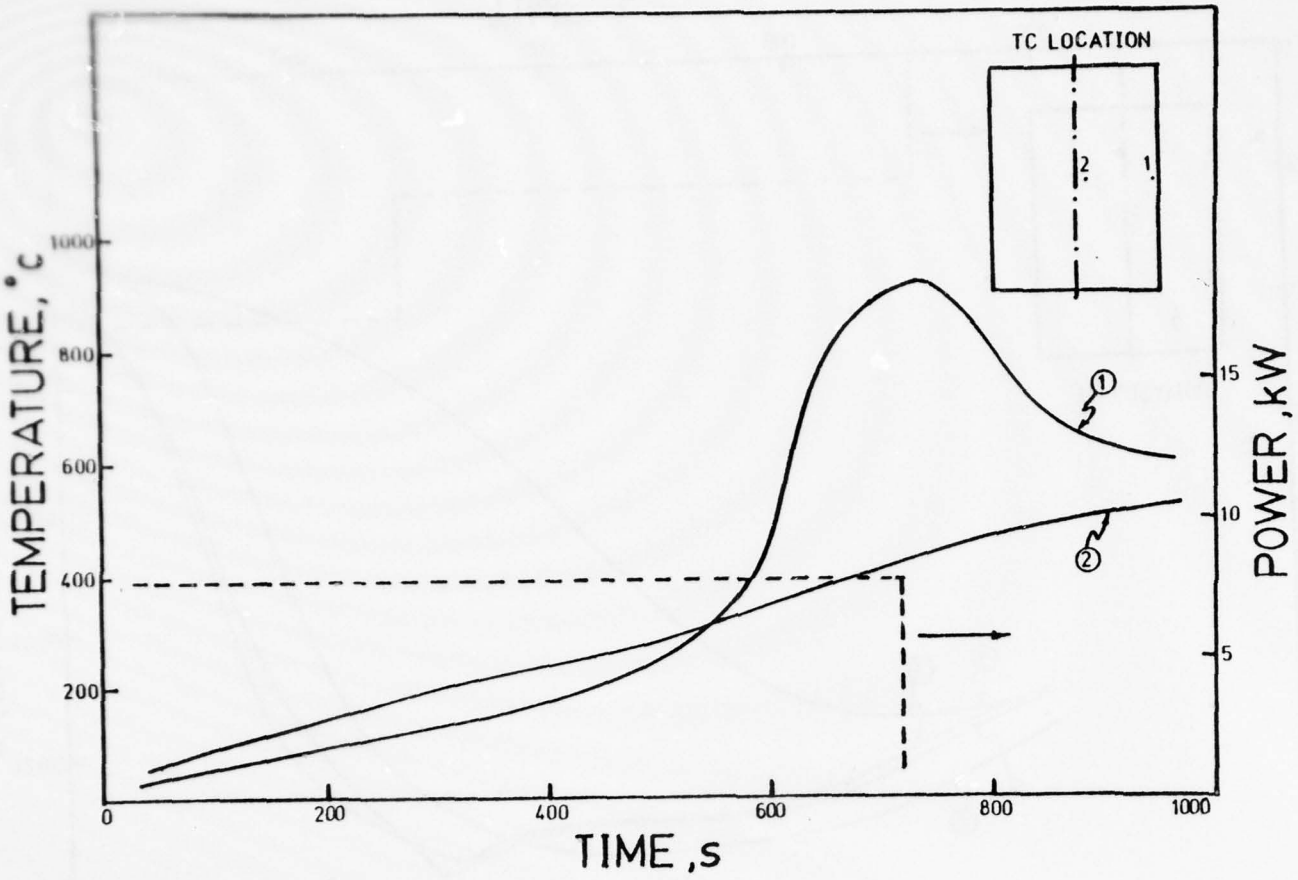

Figure II-D6. Radial temperature gradients during radio frequency heating.

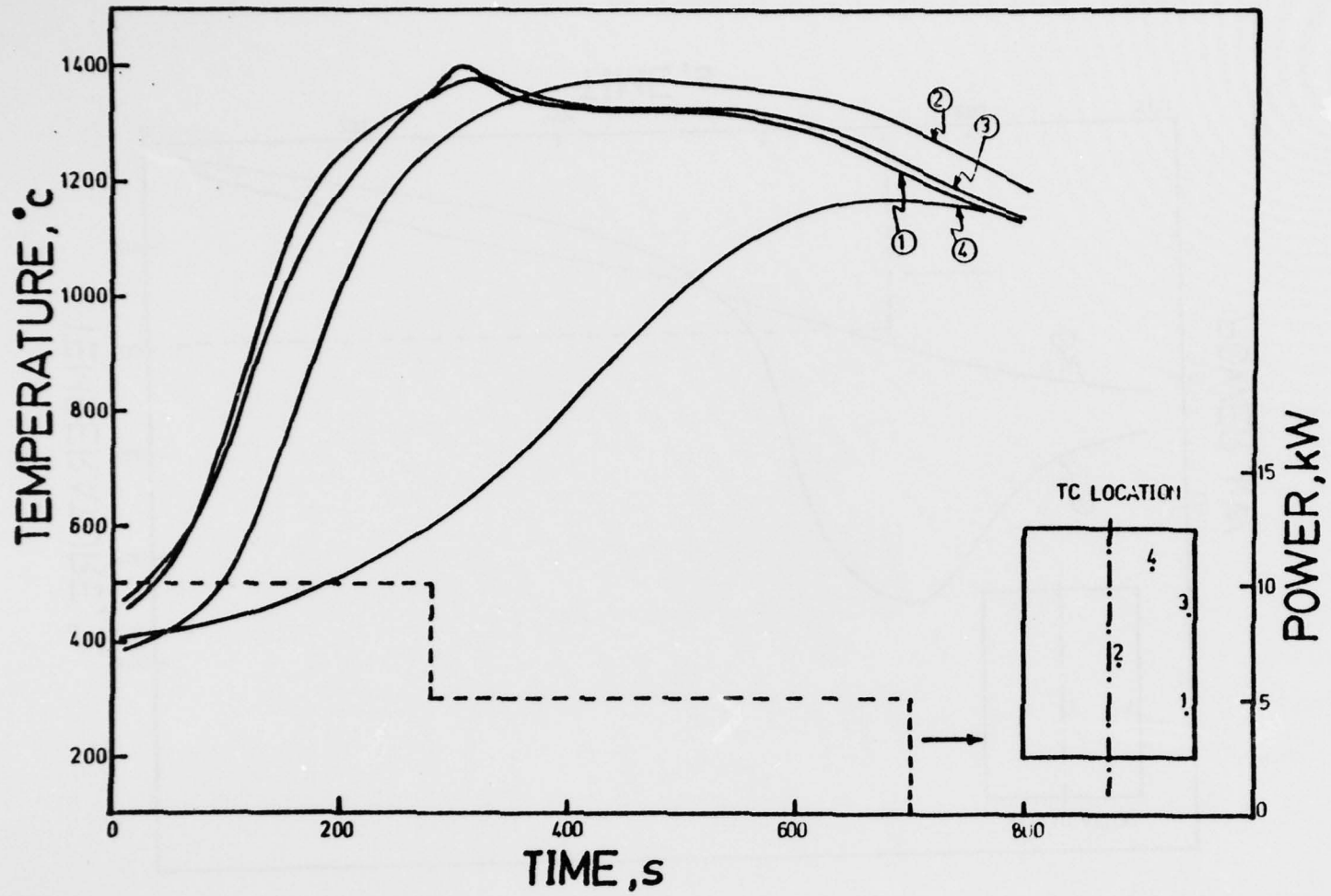

Figure II-D7. Thermal-power history of RESD powder preheated to coupling temperature.

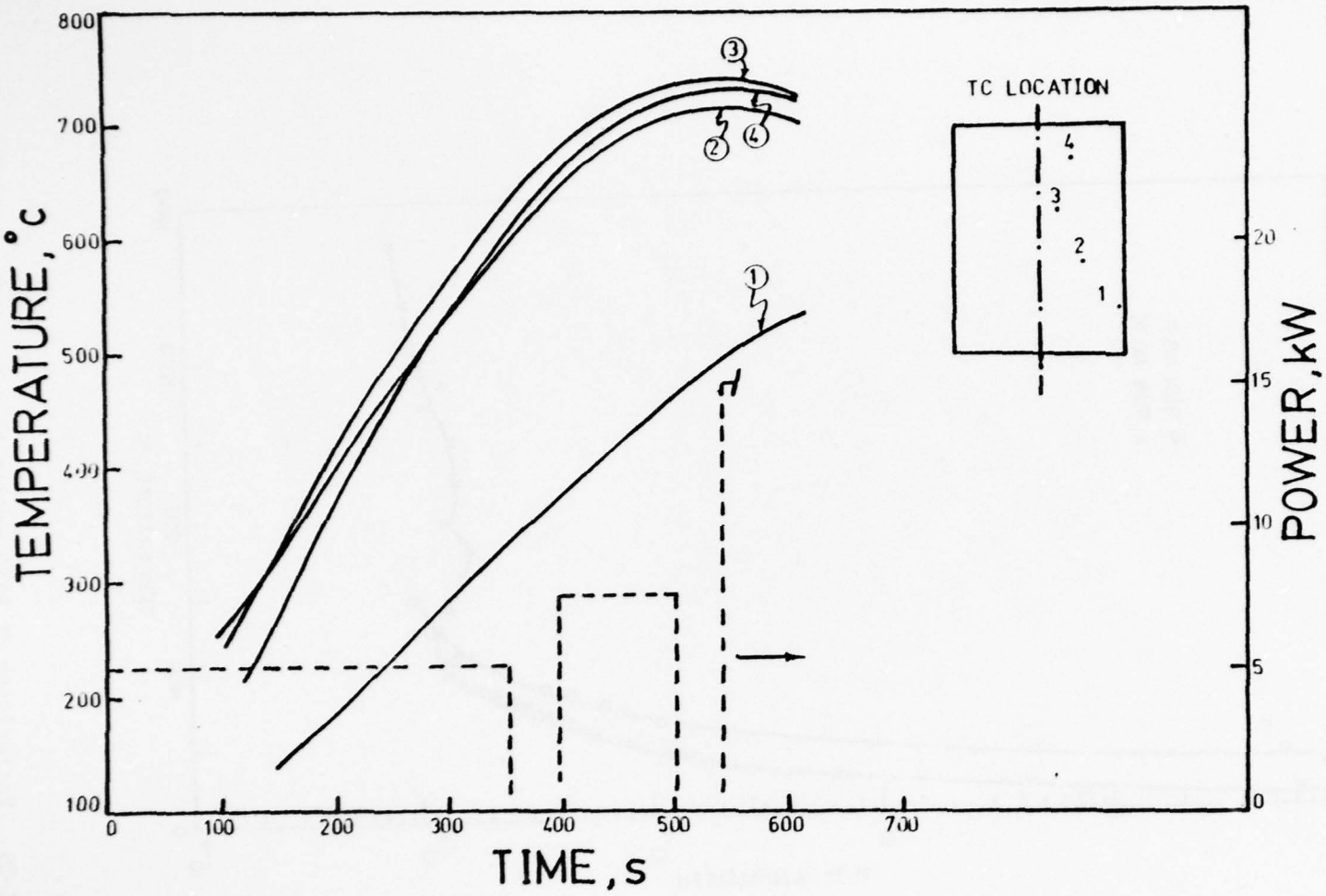

Figure II-D8. Thermal-power history for heavily oxidized STLD powder.

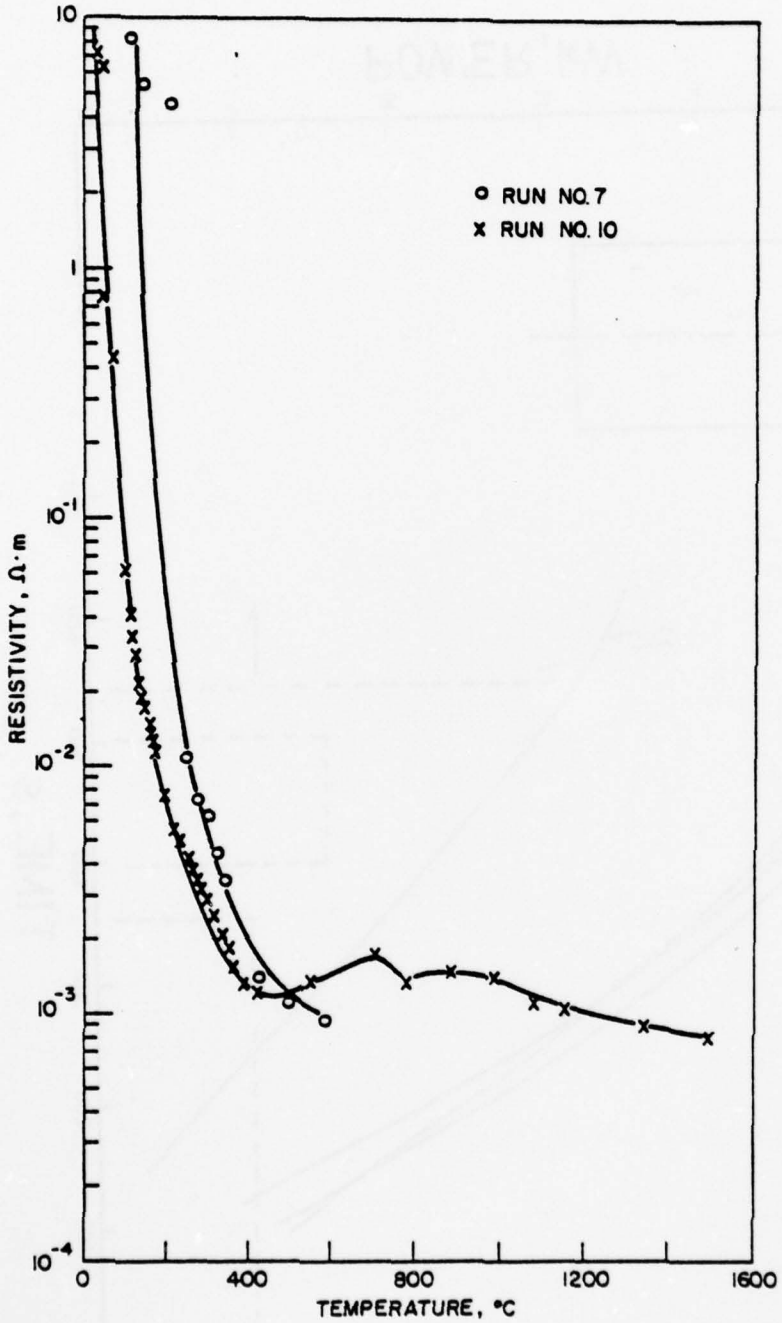

Figure II-D9. Resistivity of RESD powder as a function of temperature.

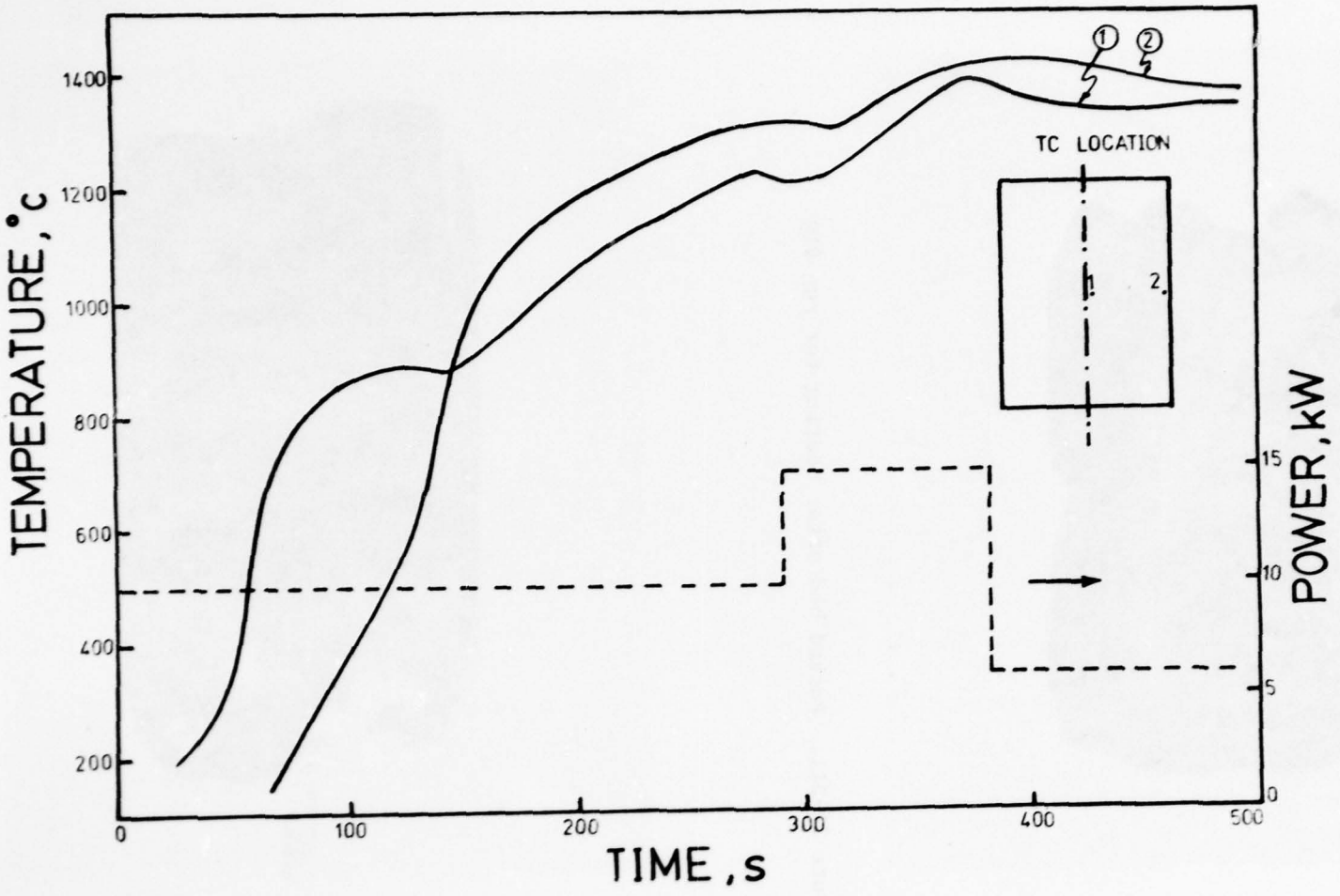

Figure II-D10. Thermal-power history for RESD powder reheated after attaining SD casting temperatures.

Figure II-D11. Packed bed after heating for run #10.

Figure II-D12. Packed bed after heating for run #5.

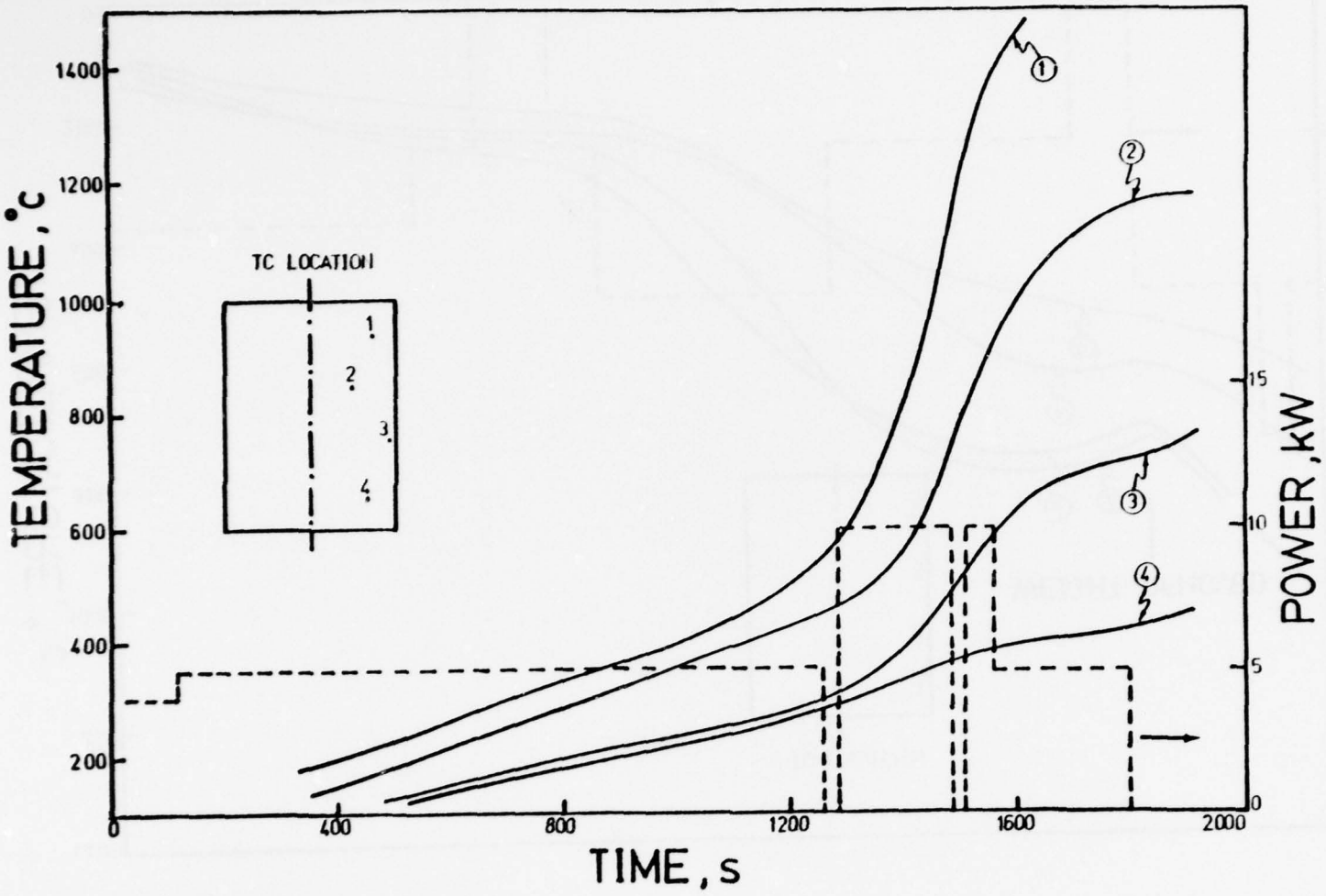

Figure II-D13. Thermal-power history for run #15 showing the effect of a metallic conductor placed on top of the bed.

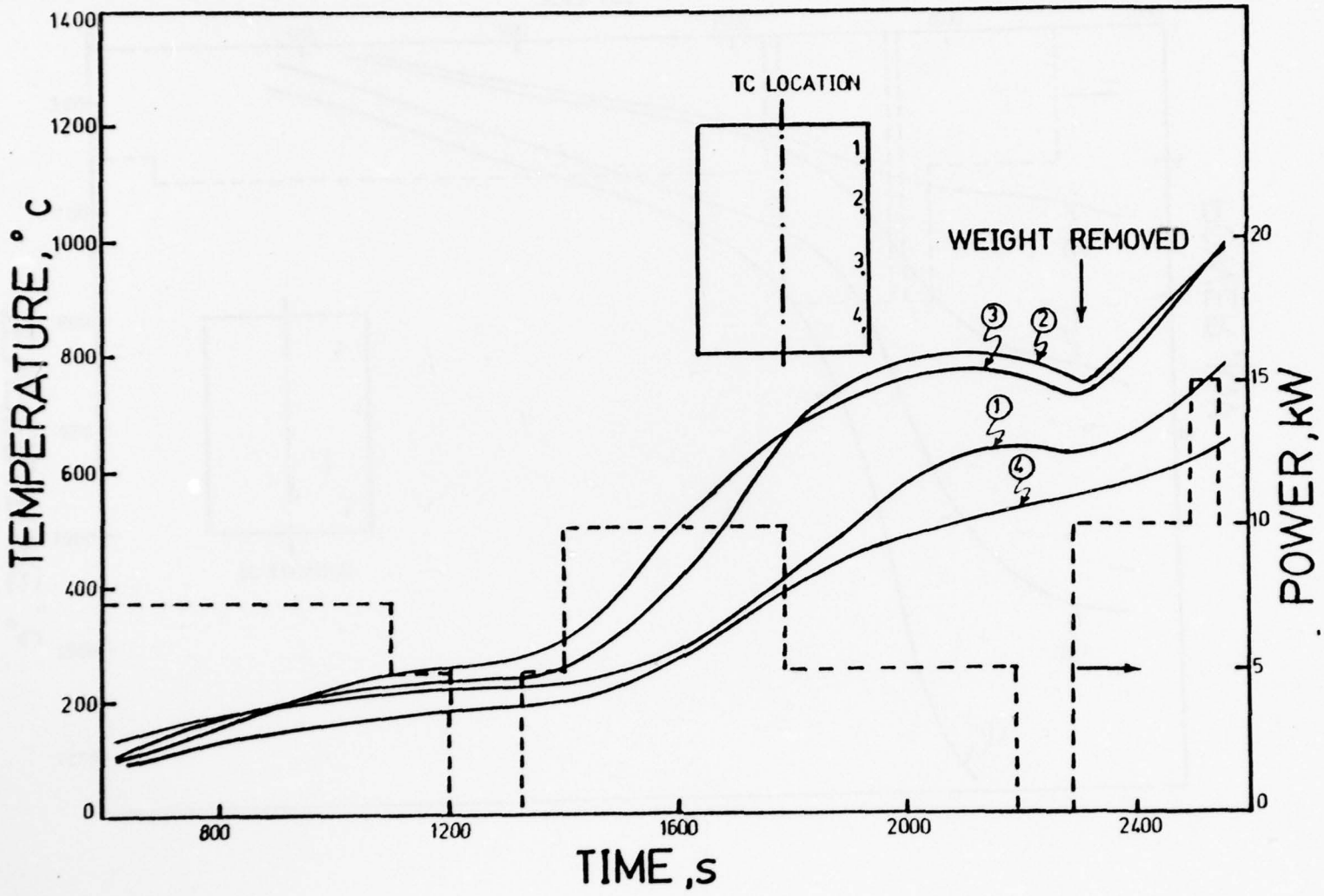

Figure II-D14. Thermal-power history for run #16 showing the effect of an inert weight placed on top of the bed.

APPENDIX II-E. INDUCTION HEATING CHARACTERISTICS OF A PACKED BED OF LOW CARBON STEEL PARTICLES

The direct induction heating (IH) of low carbon steel particles is best illustrated by showing typical temperature vs. time and power vs. time profiles. The following assumptions have been made in this analysis:

- The packed bed couples efficiently at the frequency of IH.
- The resistivity of the packed bed is a constant.
- Longitudinal temperature gradients are minimized by appropriate coil placement with respect to packed bed.
- A cylindrical packed bed geometry is chosen for simplicity with a radius, r_{PB}.

On supplying power to the packed bed, the current distribution in the bed is shown in Fig. II-E1. The distance at which the current drops to 37 percent of its surface value is called the depth of penetration, δ. The radial temperature distribution in the packed bed for different power inputs is shown in Fig. II-E2. Typical power-vs.-time schedules to attain SD casting temperatures in the packed bed are shown in Fig. II-E3(a). The surface of the packed bed is maintained at the maximum permissible temperature as shown in Fig. II-E3(b); the surface temperature for low carbon steel shot should not exceed 1530°C. When the temperature at the center of the packed bed is about 100°C below the SD casting temperature, the power supplied to the charge is reduced to P_L (power lost to the surroundings) until the packed bed attains a uniform temperature. The temperature distribution in the packed bed at different times during the heating period is shown in Fig. II-E3(c).

As the packed bed couples efficiently to the induction flux, the power supplied will be dissipated in the 'δ' zone. The interior of the packed bed

is heated by radiation and conduction from the hot zone. The time of heating will be controlled by the heat transport rate to the interior.

Experimental results indicate that the packed-bed resistivity is a strong function of temperature up to 400°C. Under these circumstances it is not possible to couple efficiently to the packed bed using a single IH frequency. At audio frequencies (4.2 kHz) the depth of penetration is considerable and radial temperature gradients are very small in magnitude. At higher frequencies, zone heating was observed and the IH characteristics will be similar to those described in this appendix.

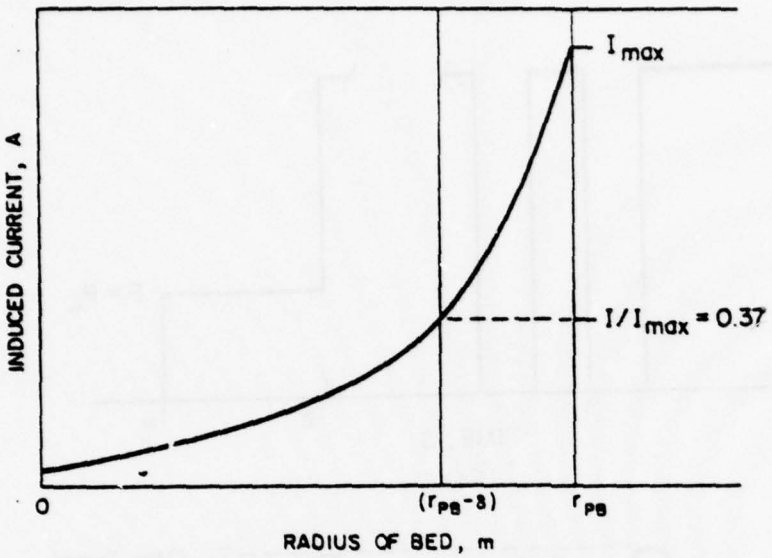

Figure II-E1. Typical current distribution in a cylindrical charge that couples efficiently to the induction flux, i.e., $d_{PB} \geq 4\delta$.

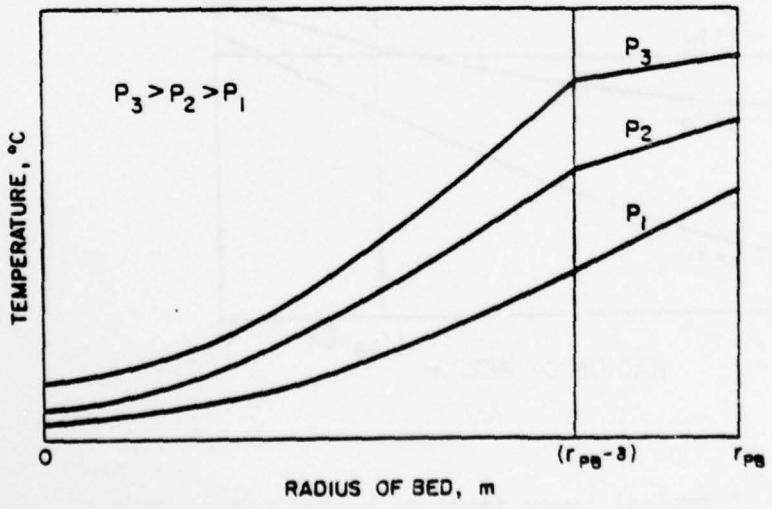

Figure II-E2. Radial temperature distribution in packed bed as a function of applied power.

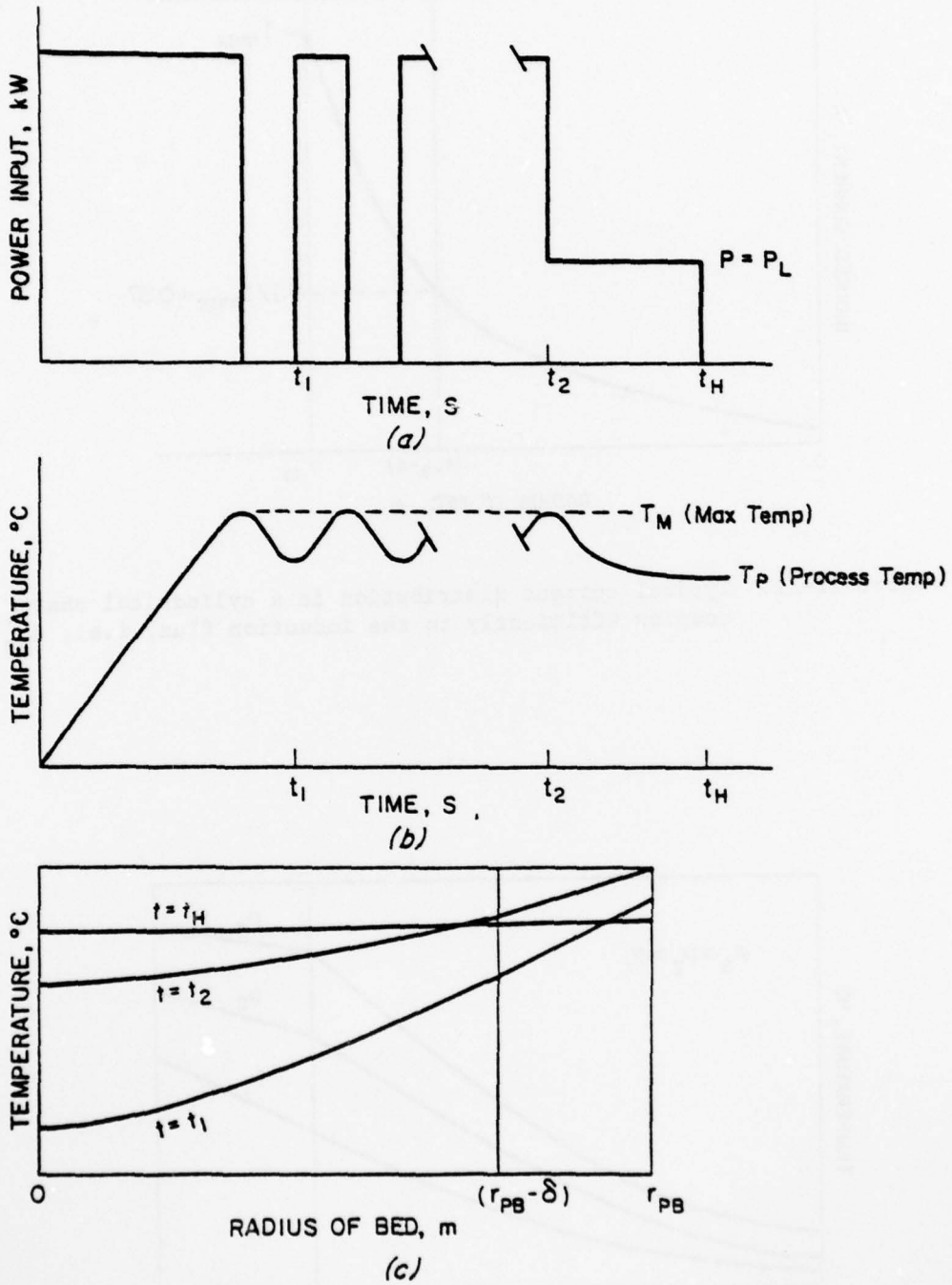

Figure II-E3. (a) A typical power input to packed bed to minimize heating time and heat the bed uniformly.
(b) Surface temperature as a function of time for the power input schedule given in (a).
(c) Radial temperature distribution in packed bed at different times for the power schedule given in (a).

APPENDIX II-F: CRITICAL PACKED BED DIAMETER AND FREQUENCY FOR INDUCTION HEATING OF PARTICLES

The depth of penetration at which the induced current has reached 37 percent of its value at the surface of the charge is given by Eq. [1].

$$\delta = 0.018\sqrt{\frac{\rho}{\mu f}} \qquad [1]$$

where

δ = depth of penetration in m

ρ = resistivity of charge in $\Omega \cdot m$

μ = magnetic permeability in $T \cdot m \cdot A^{-1}$

f = frequency in kHz

Good impedance matching is possible if the reference depth, δ, is equal to or less than 25 percent of the charge diameter, d_{PB}, as given in Eq. [2].

$$\delta \leq d_{PB}/4 \qquad [2]$$

Combining Eqs. [1] and [2] the diameter of packed bed in terms of frequency and resistivity is given by Eq. [3]

$$d_{PB} \geq 0.072\sqrt{\frac{\rho}{\mu f}} \qquad [3]$$

The magnetic permeability of low carbon steel particles is a function of temperature. Below the Curie temperature (771°C), the permeability has a value of about 3.1×10^{-5} Tesla/(Ampere · meter). Above the Curie temperature, iron is non-magnetic and the permeability has a value of 1.25×10^{-6} Tesla/(Ampere · meter).

Using the equality of Eq. [3] the critical coupling packed bed diameter can be estimated if the resistivity and induction heating frequency are known.

Tables II-FI through II-FIV give the critical packed bed diameters for a range of frequencies and packed bed resistivities.

It is often desirable to determine the critical induction heating frequency for a given packed bed resistivity and diameter. Eq. [4] gives this critical frequency.

$$f \geq 0.0052 \frac{\rho}{\mu d_{PB}^2} \qquad [4]$$

Using the equality of Eq. [4], the critical coupling frequency for different packed bed diameters and resistivities (given by $\rho = 10^N\ \Omega \cdot m$, where N is an integer) has been evaluated in Table II-FV.

Table II-FI. Critical packed bed diameter for an induction heating frequency of 4.2 kHz.

Resistivity of packed bed	$T < 771°C$, $\mu = 3.1 \times 10^{-5}$ T · m · A^{-1}		$T > 771°C$, $\mu = 1.25 \times 10^{-6}$ T · m · A^{-1}	
Ω · m	δ, m	d_{PB}, m	δ, m	d_{PB}, m
1×10^{-6}	1.6×10^{-3}	6.2×10^{-3}	7.8×10^{-3}	3.1×10^{-2}
1×10^{-5}	5.0×10^{-3}	2.0×10^{-2}	2.5×10^{-2}	1.0×10^{-1}
1×10^{-4}	1.6×10^{-2}	6.2×10^{-2}	7.8×10^{-2}	3.1×10^{-1}
1×10^{-3}	5.0×10^{-2}	2.0×10^{-1}	2.5×10^{-1}	1.0×10^{0}
1×10^{-2}	1.6×10^{-1}	6.2×10^{-1}	7.8×10^{-1}	3.1×10^{0}
1×10^{-1}	5.0×10^{-1}	2.0×10^{0}	2.5×10^{0}	1.0×10^{1}
1×10^{0}	1.6×10^{0}	6.2×10^{0}	7.8×10^{0}	3.1×10^{1}
1×10^{1}	5.0×10^{0}	2.0×10^{1}	2.5×10^{1}	1.0×10^{2}
1×10^{2}	1.6×10^{2}	6.2×10^{1}	7.8×10^{1}	3.1×10^{2}

Table II-PII. Critical packed bed diameter for an induction heating frequency of 10 kHz.

Resistivity of packed bed	$T < 771°C$, $\mu = 3.1 \times 10^{-5}$ T · m · A^{-1}		$T > 771°C$, $\mu = 1.25 \times 10^{-6}$ T · m · A^{-1}	
Ω · m	δ, m	d_{PB}, m	δ, m	d_{PB}, m
1×10^{-6}	1.0×10^{-3}	4.0×10^{-3}	5.0×10^{-3}	2.0×10^{-2}
1×10^{-5}	3.0×10^{-3}	1.2×10^{-2}	1.6×10^{-2}	6.4×10^{-2}
1×10^{-4}	1.0×10^{-2}	4.0×10^{-2}	5.0×10^{-2}	2.0×10^{-1}
1×10^{-3}	3.0×10^{-2}	1.2×10^{-1}	1.6×10^{-1}	6.4×10^{-1}
1×10^{-2}	1.0×10^{-1}	4.0×10^{-1}	5.0×10^{-1}	2.0×10^{0}
1×10^{-1}	3.0×10^{-1}	1.2×10^{0}	1.6×10^{0}	6.4×10^{0}
1×10^{0}	1.0×10^{0}	4.0×10^{0}	5.0×10^{0}	2.0×10^{1}
1×10^{1}	3.0×10^{0}	1.2×10^{1}	1.6×10^{1}	6.4×10^{1}
1×10^{2}	1.0×10^{1}	4.0×10^{1}	5.0×10^{1}	2.0×10^{2}

Table II-FIII. Critical packed bed diameter for an induction heating frequency of 50 kHz.

Resistivity of packed bed	$T < 771°C$, $\mu = 3.1 \times 10^{-5}$ T · m · A^{-1}		$T > 771°C$, $\mu = 1.25 \times 10^{-6}$ T · m · A^{-1}	
Ω · m	δ, m	d_{PB}, m	δ, m	d_{PB}, m
1×10^{-6}	4.5×10^{-4}	1.8×10^{-3}	2.3×10^{-3}	9.0×10^{-3}
1×10^{-5}	1.4×10^{-3}	5.7×10^{-3}	7.1×10^{-3}	2.8×10^{-2}
1×10^{-4}	4.5×10^{-3}	1.7×10^{-2}	2.3×10^{-2}	9.0×10^{-2}
1×10^{-3}	1.4×10^{-2}	5.7×10^{-2}	7.1×10^{-2}	2.8×10^{-1}
1×10^{-2}	4.5×10^{-2}	1.8×10^{-1}	2.3×10^{-1}	9.0×10^{-1}
1×10^{-1}	1.4×10^{-1}	5.7×10^{-1}	7.1×10^{-1}	2.8×10^{0}
1×10^{0}	4.5×10^{-1}	1.8×10^{0}	2.3×10^{0}	9.0×10^{0}
1×10^{1}	1.4×10^{0}	5.7×10^{0}	7.1×10^{0}	2.8×10^{1}
1×10^{2}	4.5×10^{0}	1.8×10^{1}	2.3×10^{1}	9.0×10^{1}

Table II-FIV. Critical packed bed diameter for an induction heating frequency of 450 kHz.

Resistivity of packed bed	$T < 771°C$, $\mu = 3.1 \times 10^{-5}$ T · m · A^{-1}		$T > 771°C$, $\mu = 1.25 \times 10^{-6}$ T · m · A^{-1}	
Ω · m	δ, m	d_{PB}, m	δ, m	d_{PB}, m
1×10^{-6}	1.5×10^{-4}	6.0×10^{-4}	7.5×10^{-4}	3.0×10^{-3}
1×10^{-5}	4.7×10^{-4}	1.9×10^{-3}	2.4×10^{-3}	9.5×10^{-3}
1×10^{-4}	1.5×10^{-3}	6.0×10^{-3}	7.5×10^{-3}	3.0×10^{-2}
1×10^{-3}	4.7×10^{-3}	1.9×10^{-2}	2.4×10^{-2}	9.5×10^{-2}
1×10^{-2}	1.5×10^{-2}	6.0×10^{-2}	7.5×10^{-2}	3.0×10^{-1}
1×10^{-1}	4.7×10^{-2}	1.9×10^{-1}	2.4×10^{-1}	9.5×10^{-1}
1×10^{0}	1.5×10^{-1}	6.0×10^{-1}	7.5×10^{-1}	3.0×10^{0}
1×10^{1}	4.7×10^{-1}	1.9×10^{0}	2.4×10^{0}	9.5×10^{0}
1×10^{2}	1.5×10^{0}	6.0×10^{0}	$7.5 \times 10^{-}$	3.0×10^{1}

Table II-FV. Critical frequency for a packed bed resistivity given by the relationship, $\rho = 10^{N}\ \Omega \cdot m$ (N is an integer)*

Packed bed diameter	Frequency, kHz x $10^{-(N+2)}$	
d_{PB}, m	T < 771°C, $\mu = 3.1 \times 10^{-5}$ T·m·A^{-1}	T > 771°C, $\mu = 1.25 \times 10^{-6}$ T·m·A^{-1}
0.01	16200	405000
0.02	4050	101000
0.03	1800	45000
0.04	1000	25000
0.05	650	16000
0.06	450	11200
0.07	330	8300
0.08	250	6300
0.09	200	5000
0.10	160	4100
0.11	130	3400
0.12	110	2800
0.13	95	2400
0.14	82	2100
0.15	72	1800
0.16	63	1500
0.17	56	1400
0.18	50	1300
0.19	45	1100
0.20	40	1000

* The value of N depends on the packed bed resistivity. If $\rho = 1.45 \times 10^{-3}\ \Omega \cdot m$, then N is equal to -3.

APPENDIX II-G: ROOM-TEMPERATURE RESISTIVITY OF POWDER

Apparatus

The setup for measuring room-temperature resistivity is shown in Fig. II-G1. The particles are contained in a glass tube. Electrical contact is made with the packed bed using a brass plate and copper rod. The contacts are connected to a solid-state, Keithley Electrometer. Resistances in the range of 0 to 10^{18} ohms can be accurately measured using this Electrometer.

Experimental Procedure

The particles were poured into the glass tube. The tube was tapped a few times to maximize the packing of the particles in the bed. A copper rod was inserted into the tube and allowed to make electrical contact with the particles at the top of the bed. The resistance between the electrical contacts was recorded from the electrometer and the packed bed height was measured. The experiment was repeated for different packed bed heights.

Theoretical Considerations of Packed Bed Resistivity

The packed bed refers to the packing of spherical particles in a container. A single size of spherical particles can be assumed to have an orthorhombic packing in such a bed.

Consider a packed bed of diameter, d_{PB}, and height, h_{PB}. The resistance of the bed can be assumed to be the sum of parallel resistances. Each parallel resistance is a function of the number of particles (of diameter d_p) that can be contained in a length equivalent to h_{PB} and the particle resistance, r_p.

The particle resistance at room temperature is given by Eq. [1],

$$r_p = r_m + 2\,(r_O + r_G) \approx 2(r_O + r_G) \qquad [1]$$

where

r_m = metallic resistance

r_O = oxide layer resistance

r_G = adsorbed gas layer resistance

A single parallel resistance is the sum of individual particle resistances in the packed bed height and is given by Eq. [2]

$$R_P = n_P r_P = 2 \frac{h_{PB}}{d_P} (r_O + r_G) \qquad [2]$$

n_P = number of particles in a height, h_{PB}

The number of parallel resistances (n) is given by the product of packed bed area and the surface density of the packing. It can be calculated using Eq. [3]

$$n = 0.453 \left(\frac{d_{PB}}{d_P}\right)^2 \qquad [3]$$

The packed bed resistance, R_T, is the parallel sum of n resistances of value R_p and is given by Eq. [4]

$$R_T = 4.4 \frac{h_{PB} d_P (r_O + r_G)}{d_{PB}^2} \qquad [4]$$

The resistivity of the packed bed is given by Eq. [5]

$$\rho_{PB} = 3.4 \, d_P (r_O + r_G) \qquad [5]$$

Eq. [5] predicts that the packed bed resistivity is a constant. The experimental results do not agree with this simple theoretical approach. The theory assumes that the particles do not contact each other in the radial direction. Actually each particle in the bed touches about six other particles in the radial direction. The resistance of the packed bed is not just the sum of parallel resistances but an interwoven complex of series and parallel resistances. The theory also assumes that the packing is orthorhombic along the entire height of the packed bed. Packing irregularities do exist.

Experimental results indicate that the resistivity of the packed bed is a strong function of the packed bed height and can be expressed by the relationship given by Eq. [6]

$$\rho_{PB} = \rho_0 (h_{PB})^n \qquad [6]$$

where ρ_0 and n are constants.

Neglecting the contact resistance of the electrodes the measured resistance can be expressed in terms of h_{PB} using Eq. [6]

$$R_T = R_{PB} = \frac{\rho_0}{A_{PB}} (h_{PB})^{n+1} \qquad [7]$$

where, A_{PB} is the area of the packed bed. The constants ρ_0 and n can be evaluated from the intercept and slopes of log-log plots of R_T vs. h_{PB}.

Contact Resistance

The contact resistance was estimated by placing a 20 mm long copper rod between the electrical contacts. The resistance was in the range of 1 to 2 ohms and could be considered negligible compared to the resistance of the packed bed.

Contact Pressure

The contact pressure is the pressure exerted by the electrical contacts while measuring the resistance of the bed. The contact pressure for all the experimental runs was 66,200 Pa.

Results

The data of R_T vs. h_{PB} are plotted in Fig. II-G2 and Fig. II-G3 for the different powders. The resistivity relationship is given in Table II-GI.

Table II-GI. Room temperature resistivity relationship for different powders used for induction heating.*

Powder	ρ_0	n	$\rho_{PB} = \rho_0 (h_{PB})^n$ $\Omega \cdot m$
RESD	3.9×10^6	1.9	$3.9 \times 10^6 (h_{PB})^{1.9}$
STSD	2.3×10^6	2.0	$2.3 \times 10^6 (h_{PB})^{2.0}$
STSDDO	9.5	0.8	$9.5 (h_{PB})^{0.8}$
STLD	1.5×10^7	1.67	$1.5 \times 10^7 (h_{PB})^{1.67}$
STLDDO (1.5mm dia.)	9.7×10^{-2}	0.25	$9.7 \times 10^{-2} (h_{PB})^{0.25}$
STLDDO (1.84 mm dia.)	6.7×10^{-2}	0.30	$6.7 \times 10^{-2} (h_{PB})^{0.30}$

*h_{PB} is the height of packed bed in meters.

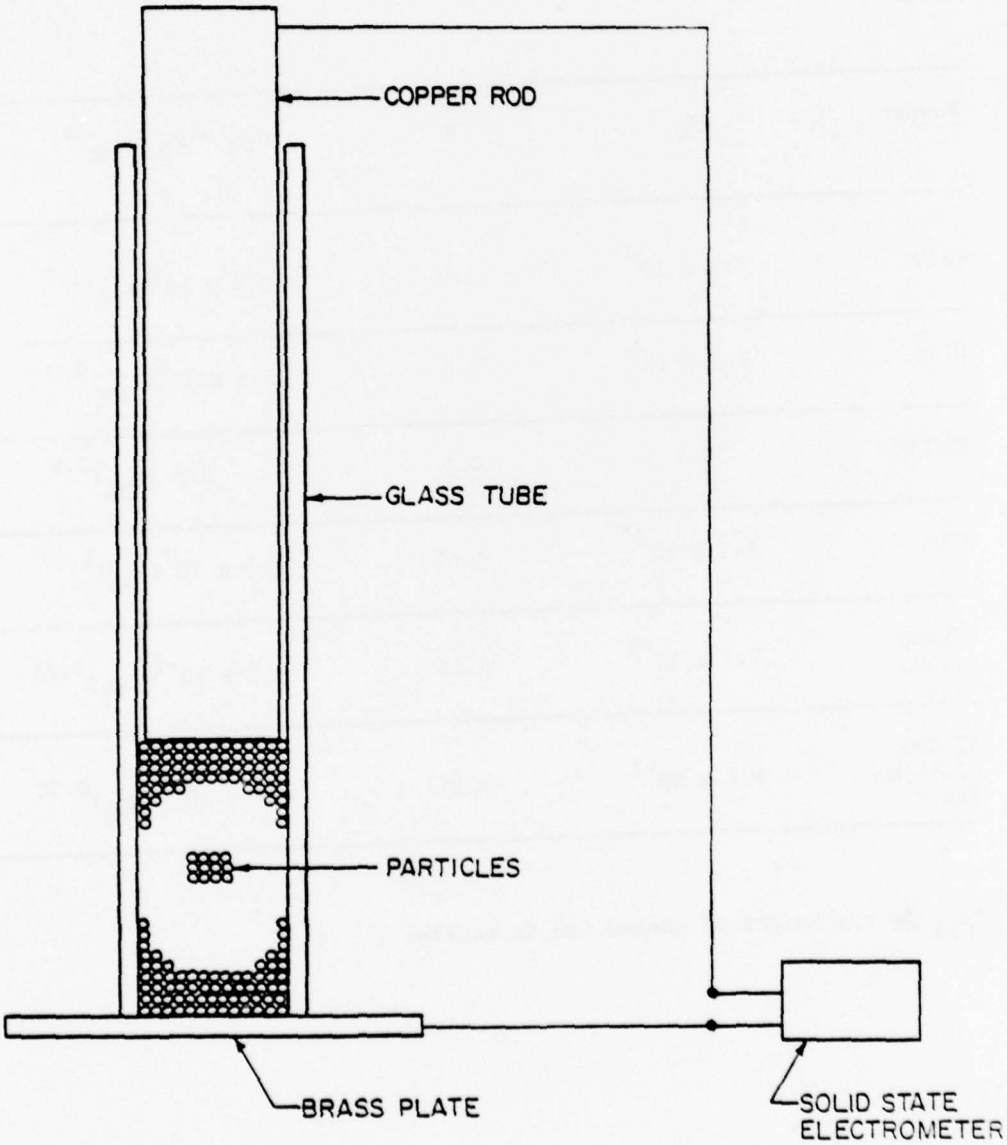

Fig. II-G1. Room temperature resistivity apparatus.

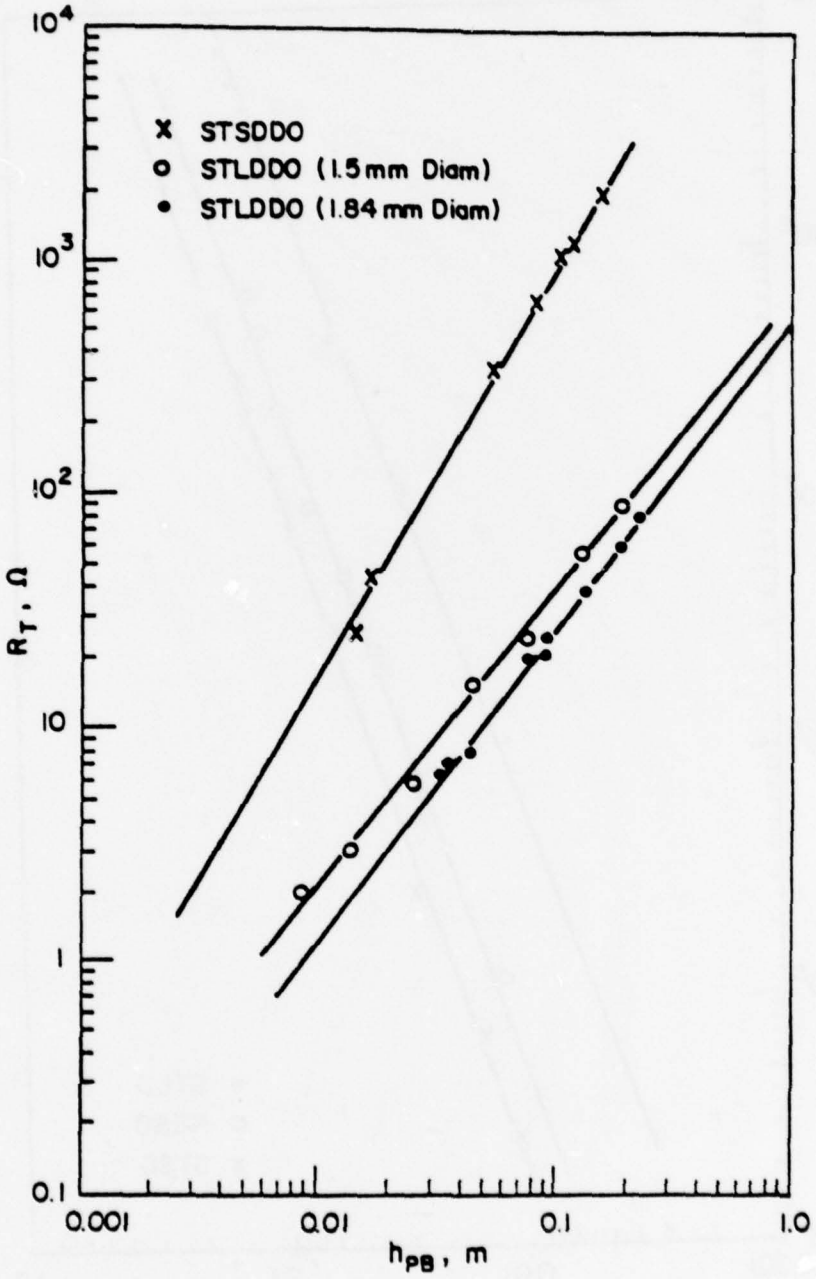

Fig. II-G2. Resistance of STSDDO, STLDDO (1.5 mm in dia.) and STLDDO (1.84 mm in dia.) as a function of packed bed height, h_{PB}.

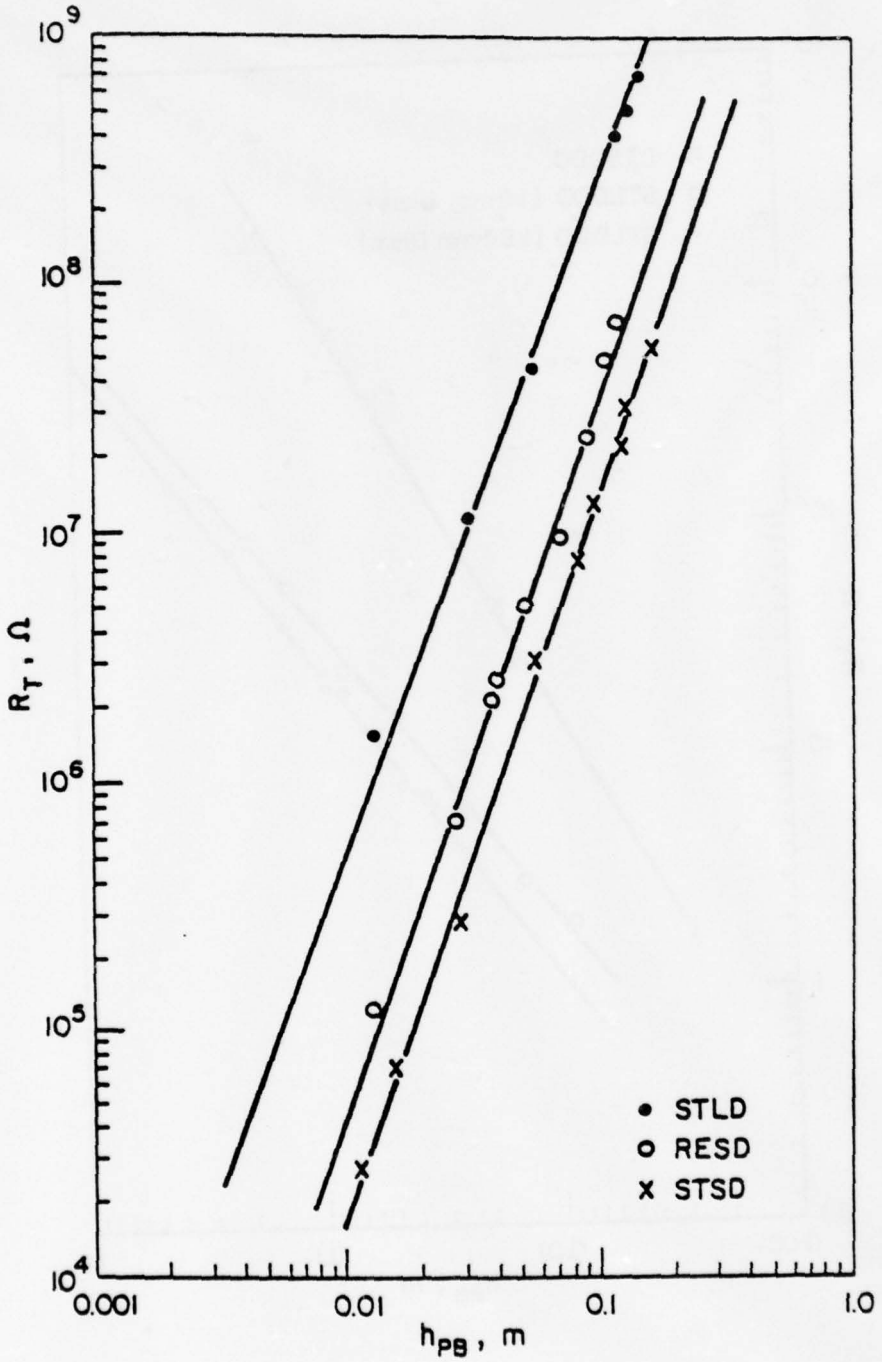

Fig. II-G3. Resistance of RESD, STLD and STSD powder as a function of bed height, h_{PB}.

APPENDIX II-H. POWDER CHARACTERIZATION

The powders used for heating are classified by the manufacturing process, particle size and shape, surface morphology and chemical analysis. The chemical analyses of the powders are given in Table II-HI. The powders are referred to by a letter code. The first two letters refer to the powder manufacturing process. The next two letters refer to the particle size and shape. Two more letters are used if the powders were subjected to physical or chemical changes after they were manufactured.

WAVS (Water Atomized, Very Small) Powder

The powder was manufactured by water atomization. The particles were irregular in shape and had an average size of 0.074 mm (0.003 in). The particle surface had a dull greyish appearance.

STSD (Steam Atomized, Small Diameter) Powder

The powder was manufactured by steam atomization. The particles were spherical in shape and had an average size of 0.28 mm (0.011 in). The particle surface was rough and had a number of perturbations on it as shown in Fig. II-H1.

STSDDO (Steam Atomized, Small Diameter, Deoxidized) Powder

The STSD powder was heated for 8 hours at 950°C in a nitrogen atmosphere. The purpose of the heat treatment was to use the dissolved carbon to reduce the surface oxide of the particles according to the reactions:

$$FeO + \underline{C} \rightarrow Fe + CO$$

$$SiO_2 + 2\underline{C} \rightarrow Si + 2CO$$

$$MnO + \underline{C} \rightarrow Mn + CO$$

The particle surface was smoother than the STSD powder and had a shiny appearance as shown in Fig. I-H2.

RESD (Rotating Electrode, Small Diameter) Powder

The powder was manufactured by the rotating electrode process. The particles were spherical in shape and had an average size of 0.216 mm (0.0085 in). The particle surface was rough as shown in Fig. II-H3.

STLD (Steam Atomized, Large Diameter) Powder

The powder was manufactured by steam atomization. The particles were spherical in shape and had an average size of 1.63 mm (0.064 in). The particles had the same surface morphology as STSD powder.

STLDDO (Steam Atomized, Large Diameter, Deoxidized) Powder

The STLD powder was heated for 48 hours in a nitrogen atmosphere. The purpose of the heat treatment was to reduce the surface oxide layer as done for STSDDO powder. The particles have the same shape and size as STLD powder. The surface morphology is expected to be the same as STSDDO powder.

Table II-HI. Chemical analysis of powders, weight percent.

Element	WAVS	STSD	STSDDO	STLDDO	RESD	STLD
C	-	1.090	0.840	0.810	0.180	0.950
Si	-	0.400	0.420	0.960	0.038	0.970
Mn	1.0	0.420	0.410	1.040	0.760	1.000
O	-	0.440	0.360	0.041	0.022	0.200
N	-	0.140	0.021	0.036	0.005	0.013
S	-	0.023	0.024	0.033	0.022	0.031
Fe	98.5	97.613	97.925	97.080	98.973	96.836
Ni	0.5	-	-	-	-	-

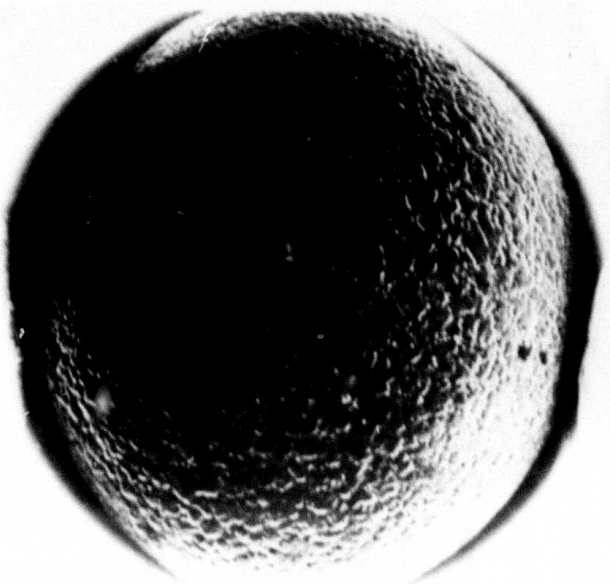

Figure II-H1. Scanning electron micrograph of STSD powder (300X).

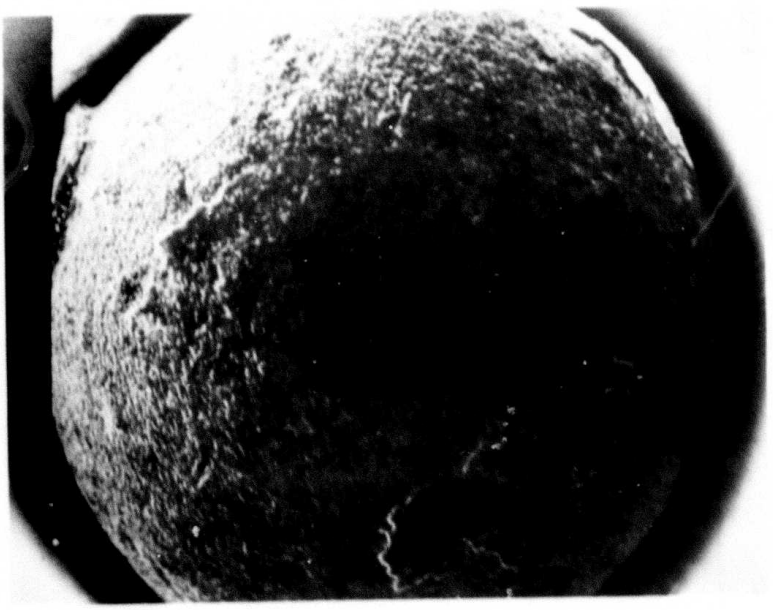

Figure II-H2. Scanning electron micrograph of STSDDO powder (300X).

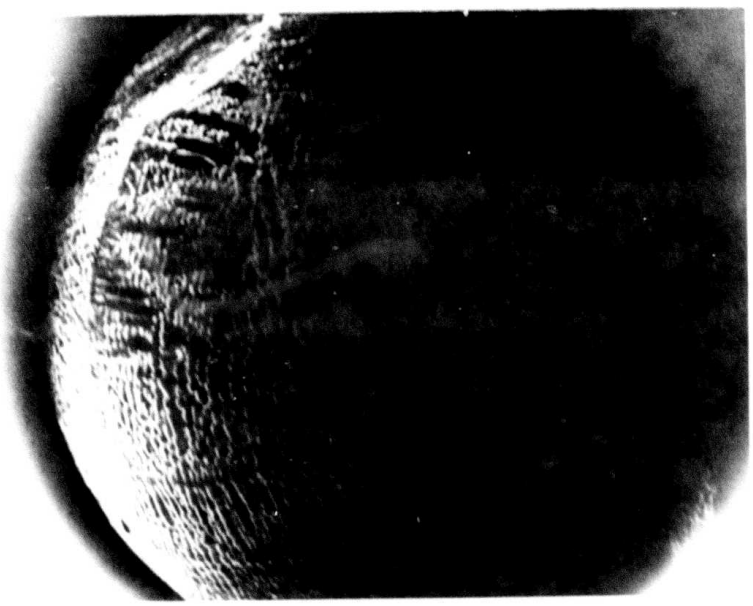

Figure II-83. Scanning electron micrograph of RESD powder (300X).

APPENDIX II-I. CRACKING PHENOMENA IN INDUCTION-HEATED PACKED BEDS

The cracks observed on heating the packed bed of low carbon steel shot to process temperatures of 1400°C have longitudinal orientation and penetrate in the radial direction. In most cases, the cracks were restricted to the central part of the packed bed where radial shrinkage was observed. However, in some cases, the longitudinal cracks extended beyond the shrinkage zone and were connected by tangential cracks.

Electro-magnetic forces act on the individual particles in the bed during induction heating. The force is in the axial direction and its magnitude is directly proportional to the induced current in the charge. A typical current density in a charge that couples efficiently to the induction flux is shown in Appendix II-E, Fig. II-E1. The current density is maximum at the surface of the charge, and so the force acting on the particles is maximum along the outer circumference of the bed. Below sintering temperatures, the packed bed contains particles that are not bonded together, so the force resulting from the induced current raises the particles above the packed bed. This results in the formation of ridges above the packed bed. The particles should slide back to the original packed bed geometry on removing the input power to the charge. However, while heating the particles to process temperatures the particles begin to sinter together at temperatures greater than 1000°C. The sintering of the particles results in their occupying the same position they did in the force field. This is responsible for the formation of ridges observed at the top of the bed. Ridge formation was also observed at the bottom of the packed bed, but the effect was very small as the particles at the bottom were in contact with a rigid mold surface (compressed fiberfrax).

The ridge formation resulted in poorer packing in the original packed bed geometry. To accommodate for this depletion the original packed bed geometry

must change. The change is brought about by a shrinkage in the midsection of the packed bed.

If the ridge formation is severe, i.e., more particles have been raised above the packed bed, then the shrinkage is much more at the midsection of the packed bed to accommodate the depletion of particles in the bed. There is a limit to the amount of cylindrical shrinkage permissible at the midsection of the bed, as the maximum shrinkage depth is at the point where the gravitational force balances the induction force. In such cases the depletion of particles due to ridge formation is accommodated in the packed bed by the formation of cracks oriented in the direction of the external induction force.

In two of the heating runs, numbers 5 and 18 (Appendix II-D), no cracks or shrinkage was observed. In these runs, the particles were heated rapidly using high power inputs. It was difficult to maintain high power levels to a charge whose load coupling characteristics are very sensitive to temperature. The induction unit had manual controls and so the power to the charge had to be frequently shut off to balance the load by adjusting the voltage and capacitor controls.

Consider two situations during the heating of the particles in the bed at high power inputs. The packed bed temperature is below the sintering temperature and the power to the charge is shut off. In this case the particles will fall back and regain their original mold geometry. However, if the particles are rapidly heated to sintering temperatures and the power to the charge is shut off, then the particles should slide back to the original mold geometry. At this stage if sufficient time is given for the particles to sinter together before reapplying power, then the particles are no longer loosely held. On reapplying power the induction force acts on the bed rather than the individual particles. In such cases no ridge formation, cracks or shrinkage are observed in the packed bed. The results of runs number 5 and 18 (Appendix II-D) substantiate the above explanation.

An alternative mechanism for the cracking phenomena can be attributed to non-uniform sintering of particles in the bed. Longitudinal temperature gradients were observed in the packed bed during heating. The top and bottom parts of the bed were at a lower temperature than the middle part of the bed. At high temperatures, this non-uniform temperature distribution in the bed results in the particles sintering at a faster rate in the middle part of the bed. The enhanced sintering rate at the center could be responsible for crack nucleation due to shrinkage resulting from sintering of the particles.

Once the cracks are formed then there is a much higher resistance across the cracks than at the crack tips. This reduces the amount of heat dissipated at the sides of the crack and so the particles located in this zone are heated much less than the particles located at the tips of the crack. The particles at the crack tips sinter to a greater extent and the shrinkage resulting from sintering leads to the propagation of the crack.

One method of preventing cracks is to stop heating after rapidly attaining temperatures of 1000°C to 1200°C to permit the particles to sinter together for about 100 seconds. The sintered bed can then be raised to process temperatures.

Another suggested method was to place a weight on top of the packed bed as was done in runs number 15 and 16 (Appendix II-D). However, the weight reduces the induced current density in the charge by inhibiting electrical continuity between the particles in the circumferential direction (the direction of maximum electrical field in the packed bed). The net effect of the weight is that the packed bed remains inert to the induction flux and can be heated only by magnetic hysteresis.

III. PERFORMANCE AND OPERATING CHARACTERISTICS OF THE PARTICLE VALVE - TASK 2

M. Paliwal
D. Apelian
G. Langford

SUMMARY

A particle valve for liquid metals consisting of an aggregate of non-wetting refractory particles can have metallurgical applications ranging from atomization to filtration to a quick-acting valve for rapid cycle casting of steel by diffusion solidification. The performance of such a particle valve is evaluated experimentally and theoretically. The supportable head over the particle valve is derived as a function of particle size and liquid surface tension. The experimentally determined breakthrough pressures in the Sn/Al_2O_3 and Hg/Al_2O_3 systems agree with and confirm the derived expression

$$\Delta P = -10.9 \left(\frac{\gamma_{LV}}{d}\right) \cdot \cos \theta'_A$$

where γ_{LV} is the liquid-vapor surface tension, d is the particle diameter, and θ'_A is the apparent advancing contact angle between the liquid and solid. Several mechanisms are identified which may cause failure of the particle valve by disruption or premature breakthrough. Failure can be initiated by buoyancy or turbulent forces acting on the individual particles causing flotation; the breakthrough pressure can be exceeded momentarily by forces caused by various impacts such as droplets falling into the liquid metal. The critical operating limits are given. It is shown that a particle valve can be relied upon when utilized within these limits.

TABLE OF CONTENTS: Section III. Performance and Operating Characteristics of the Particle Valve - Task 2

III.A Introduction 116

III.B Derivation of Breakthrough Pressure-Theoretical Considerations 117

III.C Experimental Procedure 122

III.D Results and Discussion 124

1. Particle Valve Performance 124

a. Required Breakthrough Pressures 124
b. Reliability of the Particle Valve 126
c. Spherical vs. Irregular Particles 126
d. Particle Valve Height 126

2. Disruption Mechanisms of the Particle Valve 127

a. Failure Due to Direct Impingement of Liquid Droplets on the Particle Valve 127
b. Failure by Augmented Hydrostatic Pressure Caused by an Impinging Liquid Droplet 129
c. Failure Due to Buoyancy Forces Acting on Individual Particles - Flotation 130

3. Practical Considerations 132

III.E Conclusions 133

References 124

Tables 125

Figures 132

Appendix III-A: Buoyancy Forces Acting on Individual Particles 141

III.A INTRODUCTION

In the SD casting process[1,2] a liquid of high carbon content (≈3%C) is infiltrated into a bed of low carbon steel shot (≈0.01%C). The liquid is isolated from the shot by an aggregate or bed of coarse, non-wetting refractory (Al_2O_3) beads, hereafter termed a particle valve (PV). Figure 1 illustrates the general arrangement of the SD casting process. Because of the non-wetting nature of the liquid cast iron on Al_2O_3, the surface tension forces can prevent the liquid cast iron from penetrating the Al_2O_3 PV. When melt transfer is required, a gas pressure is applied in excess of that pressure which can be supported by the PV, causing infiltration of the particle bed and subsequently of the steel shot. The particles in the PV are usually much coarser than those in the steel shot bed so that the pressure drop through the PV is negligible.

A quick release valve for liquid metals has numerous metallurgical applications and advantages - (i) transferring of liquid metal between vessels without tilting, (ii) pouring slag-topped melts without entrapping slag in the metal, (iii) isolating the melt from the orifice in the bottom pour atomization processes, and (iv) filtering liquid metals. A particle valve is also successfully being utilized at Drexel University in a bottom-pour atomization furnace for the manufacture of low carbon steel shot, where it separates the melt from the orifice (Fig. 2). See Section IV of this report. Another useful application of the PV as a filter medium during atomization has been shown by Apelian et al.[3] in filtering and atomizing 7075 aluminum through a consolidated bed of Al_2O_3 refractory particles. During melt purification, a PV can also be used as a medium through which bubbling of gases can take place.[4]

The objectives of this study are:

(i) To derive and measure the relationship between the supportable metallostatic head and particle size as a function of surface tension, contact angles, bed height, bed porosity, and sphericity and surface roughness of the particles.

(ii) To evaluate the reliability of a PV as a useful liquid valve for metallurgical applications.

(iii) To investigate the various mechanisms which will disturb the PV and cause its failure.

III.B DERIVATION OF BREAKTHROUGH PRESSURE - THEORETICAL CONSIDERATIONS

In general, flow of liquids through porous media can be separated into two regimes: (i) the liquid wets the porous medium, or (ii) the liquid is non-wetting.

For the case of wetting liquids, the surface tension forces do not act as the major barrier for flow, such as in the case of water flow through soils. Various investigators, D'Arcy[5], Poiseuille[6], Kozeny and Carman[7] have attacked the problem and offer governing equations relating the pressure needed for a given flow rate as a function of the bed length and permeability and viscosity of the liquid. In these investigations the permeability factor was considered as an overall parameter taking into account the bed porosity, tortuosity of the existing channels, surface area of the porous medium, etc.

For the case of non-wetting liquids, which is the case of interest here, surface tension forces need to be overcome for flow to be initiated. The pressure required to force a liquid through a constriction is given by Adam[8]:

$$\Delta P = \gamma_{LV}\left(\frac{1}{R_1} + \frac{1}{R_2}\right) \cdot \cos\theta \qquad (1)$$

where R_1 and R_2 are the principal radii of curvature, θ is the stationary contact angle between the solid and liquid, and γ_{LV} is the surface tension or the free surface energy of the liquid-vapor interface. For a capillary of circular cross-section, R_1 and R_2 are then equal to the capillary radius, r_c, and Eq. (1) can be written as:

$$\Delta P = -\frac{2\gamma_{LV}}{r_c} \cdot \cos\theta \qquad (2)$$

When the liquid is not stationary but rather moving down the capillary the contact angle is taken as the advancing contact angle, θ_A [8]. In the dynamic situation taking into account the advancing contact angle and the characteristic surface roughness of the particles gives rise to an apparent advancing contact angle, θ'_A. Eq. (2) is then modified to:

$$\Delta P = -\frac{2\gamma_{LV}}{r_c} \cdot \cos\theta'_A \qquad (3)$$

For penetration of a liquid into a capillary of non-circular cross-section a widely accepted method[9] is to define an effective radius or hydraulic radius m as the ratio of the area of the orifice to the perimeter of the orifice, or as the ratio of the volume to the surface area of the pore itself.

$$m = \frac{A}{L} = \frac{\text{area of orifice}}{\text{perimeter of orifice}} \text{ , or alternatively} \qquad (4)$$

$$m' = \frac{V}{A} = \frac{\text{volume of pore}}{\text{surface area of pore}} . \qquad (5)$$

Thus, the breakthrough pressure in terms of the hydraulic radius, m, becomes:

$$\Delta P = -\frac{\gamma_{LV} \cdot \cos\theta'_A}{m} \qquad (6)$$

The normal packing of spheres into a mold can be approximated by an orthorhombic arrangement giving a porosity of about 40%[10]. Irrespective of the packing arrangement and total porosity of the bed, the smallest pore will be the interstitial site formed by three touching spheres on a given cross-sectional plane. The latter interstitial site can also be thought of as a triangular orifice, as illustrated in Fig. 3a. The maximum breakthrough pressure will be that required for the liquid to penetrate through the minimum constriction site. It can be safely assumed that a differential fluid element will have to penetrate through such a minimum constriction site during flow through the maze-like medium. Thus, the particle valve will fail or become operable at the "maximum" breakthrough pressure corresponding to the "minimum" constriction site.

Taking into consideration two distinctly different liquid phase geometries within the triangular orifice and the corresponding hydraulic radii gives rise to two different breakthrough pressures. For the case shown in Fig. 3a, m = 0.0255d and

$$\Delta P = -39.2 \left(\frac{\gamma_{LV}}{d}\right) \cdot \cos \theta'_A \tag{7}$$

whereas for the case shown in Fig. 3b, m = 0.0387d and

$$\Delta P = -25.8 \left(\frac{\gamma_{LV}}{d}\right) \cdot \cos \theta'_A \tag{8}$$

where d is the diameter of the beads in the particle bed.

Previously, Langford and Cunningham[1] have used an approximate breakthrough pressure:

$$\Delta P = -20 \left(\frac{\gamma_{LV}}{d}\right) \cdot \cos \theta'_A \tag{9}$$

and assumed a value of 180° for θ'_A, thus reducing Eq. (9) to:

$$\Delta P = \frac{20\gamma_{LV}}{d} \tag{10}$$

Mayor and Stowe[11] offer a theoretical breakthrough pressure which takes into account the fact that the porosity of the bed and the contact angle of the fluid affect the actual geometry of the liquid within the orifice. Assuming a similar triangular orifice as shown in Fig. 3a and a contact angle of 180°, their breakthrough pressure is:

$$\Delta P = \frac{22.64\gamma_{LV}}{d} \qquad (11)$$

For a similar triangular orifice, Frevel and Kressley[12] through analyses of the radii of curvature offer a slightly different breakthrough pressure:

$$\Delta P = -17.66 \left(\frac{\gamma_{LV}}{d}\right) \cdot \cos\theta \qquad (12)$$

The hydraulic radius, m, can easily be calculated when the liquid wets the pore surface - the case when the triangular orifice is completely filled with the liquid phase. For non-wetting fluids more exact calculations taking into account the effect of porosity and contact angle on the geometry of the fluid in the pore as done by Mayor and Stowe[11] and Frevel and Kressley[12] are not only cumbersome in approach but also give widely differing results. The use of the hydraulic radius, m, can satisfactorily be used for the case when the fluid wets the pore surface. Flow equations thus derived confirm well the experimental results[9]. However, for the case of a non-wetting fluid a similar approach using the hydraulic radius, m, cannot be satisfactorily used, but one must rather consider the surface tension forces which are influenced by the magnitude and sign of the radii of curvature.*

* Radii of curvature have the same sign if their centers of rotation lie on the same side of the interface. If the centers of rotation are on opposite sides of the interface, the radii of curvature have opposing signs (positive and negative). To be consistent with our definition of ΔP, a radius of curvature is assigned a negative sign when its center of rotation lies on the side of the interface occupied by the liquid.

When surface tension forces are the overriding factor during flow, the hydraulic radius approach has no physical significance. Our approach accounts for the actual curvatures of the fluid as it goes through the constriction site. The triangular constriction site envisioned is shown in Fig. 4a. Two cross-sectional views of the liquid within the constriction site, one parallel to the plane of the paper, and the other perpendicular, are shown in Figs. 4b and 4c, respectively. Mathematically, the equation of the free surface of the liquid as it is flowing through the site is:

$$\frac{1}{R_1} + \frac{1}{R_2} = \text{constant} \tag{13}$$

where R_1 and R_2 are the major and minor principal radii of curvature of the liquid.

For this particular liquid surface, the radii of curvature can be approximated at a particular point, point D - Fig. 4b. One radius, R_1, is fixed by the boundary constraint due to the shape of the beads and is identical to the radius of the beads:

$$R_1 = r \tag{14}$$

At point D, the radius R_2 of the liquid surface can be expressed as a function of the radius of the inscribed circle in the triangular orifice, r_c.

$$R_2 = -r_c \tag{15}$$

However, the radius of the inscribed circle, r_c, can be easily expressed as a function of the radius of the spherical beads, r. Geometrical considerations lead to the result

$$R_2 = -r_c = -0.1547\ r \tag{16}$$

Applying the above values in the fundamental expression:

$$\Delta P = \gamma_{LV} \left(\frac{1}{R_1} + \frac{1}{R_2}\right) \cdot \cos \theta'_A \qquad (17)$$

The breakthrough pressure becomes:

$$\Delta P = -10.9 \left(\frac{\gamma_{LV}}{d}\right) \cdot \cos \theta'_A \qquad (18)$$

III.C EXPERIMENTAL PROCEDURE

Tin and mercury were chosen as the model melt materials since both are non-wetting to Al_2O_3, relatively reliable surface tension data are available and the required experimental setup was greatly facilitated by the low melting points of both tin and mercury.

Sn/Al_2O_3 System:

A schematic diagram of the apparatus used is shown in Fig. 5. The graphite crucible containing the PV and the melt had two openings at the bottom. The first opening contained an open ended thermocouple wired to a recorder, which signaled liquid infiltration of the PV when the thermocouple became short circuited. The second opening was connected to a tube open to the atmosphere. The crucible was enclosed in a pressure vessel which was subsequently evacuated and backfilled with argon. The pressure differential above the melt and the bottom of the PV was measured by a manometer placed between points 10 and 11, Fig. 5.

Commercially available grade A tin was used. Both irregular and spherical Alcoa tabular alumina particles of various sizes were used to construct the PV. These particles were carefully machine sieved and then hand sieved in the different mesh size ranges. A layer of fiberfrax* and -325 mesh (<45μm)

* Manufactured by The Carborundum Company, Niagara Falls, N. Y.

alumina powder below the PV protected the two bottom openings of the crucible from clogging with liquid tin following breakthrough. Similarly, -325 mesh (<45μm) alumina powder around the edges of the PV insured that the liquid tin did not leak along the smooth sides of the crucible, where the packing of the particles was relatively less efficient.

After assembling a 1.5 cm high PV in the graphite crucible, solid tin was carefully emplaced, connections for the temperature recorder and induction coils were made, and the pressure vessel was evacuated and back filled with argon. Audio frequency induction heating (@ 4.2 kHz) was employed for melting and maintaining the temperature of the liquid tin at 300°C. A chromel/alumel thermocouple was used for recording and monitoring the temperature of the melt. During melting and equilibrating, the pressure inside the vessel was maintained at one atmosphere. Temperature of the melt was kept constant at 300°C in all the experiments. Upon temperature equilibration the bottom of the crucible was opened to the atmosphere via the valve and bubble tube - point 10, Fig. 5. The argon pressure inside the vessel was increased until the open ended thermocouple indicated breakthrough of the liquid through the PV. The required pressure was duly noted at the manometer.

Hg/Al_2O_3 System:

Since the mercury/Al_2O_3 system did not require heating or temperature monitoring a different set up was used with essentially the same logic as used in the Sn/Al_2O_3 experiments. The PV was assembled in a long quartz cylinder of 3.8 cm diameter and argon was used for pressurization.

III.D RESULTS AND DISCUSSION

1. Particle Valve Performance

a. Required Breakthrough Pressures

Experimentally measured breakthrough pressures for the different Al_2O_3 particle size ranges for the Sn/Al_2O_3 and Hg/Al_2O_3 systems are given in Tables I and II, respectively.

In the available literature no data could be found on contact angles between Hg and Al_2O_3. Allen and Kingery[13] have measured the contact angles of Sn on Al_2O_3 in vacuum at temperatures ranging from 800°C to 1470°C. They report values of θ (stationary contact angle) as 162° at 800°C, 167° at 1100°C, and 166° at 1200°C. The contact angle of Sn on Al_2O_3 at 300°C cannot be extrapolated from Allen and Kingery's data. Moreover, they have measured the stationary contact angle - a stationary drop resting on a finely polished surface - which is quite different than the apparent advancing contact angle, θ_A'. In a dynamic situation the advancing contact angle is always greater than the stationary contact angle, and the receding contact angle is smaller than the stationary contact angle[14]. Furthermore, the surface roughness of the solid substrate should be considered since it also influences the apparent contact angle. For liquids with contact angles greater than 90° the effect of surface roughness is to increase the apparent advancing contact angle, θ_A' [8,14,15]. Thus the apparent advancing contact angle can be as much as 50° to 60° greater than measured stationary contact angles[8] For purposes of our calculations we have assumed that the apparent advancing contact angle, θ_A' is equal to 180°, so that $\cos \theta_A' = -1$ (if θ_A' had an actual value of 165° the error in the value of $\cos \theta_A'$ would only be 3.4%, since $\cos 165° = -0.966$).

For the Sn/Al_2O_3 system, using a value of 580 dyne/cm (580 mN/m) for γ_{LV} and taking the advancing contact angle, θ_A', to be 180°, a linear regression analysis of the experimentally measured breakthrough pressures, ΔP, as a function of the particle diameter, d_{avg}, yields (Table I):

$$\Delta P = -11.1 \left(\frac{\gamma_{LV}}{d}\right) \cdot \cos \theta_A' \qquad (19)$$

with a correlation coefficient of 0.996. Figure 6 is a plot of Eq. (19).

Similarly, for the Hg/Al_2O_3 system using values of 485 dyne/cm (485 mN/m) for γ_{LV} and 180° for θ_A', a linear regression analysis of the experimentally measured breakthrough pressures, ΔP, as a function of the particle diameter, d_{avg}, yields (Table II):

$$\Delta P = -10.9 \left(\frac{\gamma_{LV}}{d}\right) \cdot \cos \theta_A' \qquad (20)$$

with a correlation coefficient of 0.992. Figure 7 is a plot of Eq. (20). Both of the empirical fits shown in Figs. 6 and 7 agree very well with the theoretically derived relationship (Eq. (18)).

Calculated theoretical breakthrough pressures from Eq. (18) and the corresponding percent difference from the experimental values are given in columns 6 and 7 of Tables I and II for the Sn/Al_2O_3 and Hg/Al_2O_3 systems respectively. The maximum error for the Sn/Al_2O_3 system is 12.2% and for the Hg/Al_2O_3 system is 9.1%. The maximum errors occurred at low breakthrough pressures where large diameter particles were employed. The inherent experimental error involved in measuring the metallostatic head above the PV and the manometer reading is ±0.15 inHg (0.51×10^3 Pa). At 2.0 inHg (6.8×10^3 Pa) this would imply a 7.5% error. In light of the error due to the experimental setup itself, the existing maximum error between the theoretical and experimental values, 12.2% and 9.1% for the Sn/Al_2O_3 and Hg/Al_2O_3 systems, respectively, are acceptable.

Frevel and Kressley[12] have carried out mercury porosimetry studies on the Hg/glass microbeads system. Their experimentally measured and derived breakthrough pressures are respectively given, columns 3 and 4, Table III. Better agreement between experimental and theoretical values is obtained when comparing Frevel and Kressley's experimental data with our derived breakthrough pressure, Eq. (18), see Table III. This further confirms the validity of our theoretical analysis of the required breakthrough pressure.

b. Reliability of the Particle Valve

Experiments were repeated with the same experimental setup to check the reliability of the PV and the repeatability of the results. Four experiments using -16, + 20 mesh (850 to 1180μm) irregular particles along with two experiments with spherical particles of each size range -18, + 20 mesh (850 to 1000μm) and -25, + 30 mesh (600 to 710μm) gave the results shown in Table I for the Sn/Al_2O_3 system. Measured breakthrough pressures varied by only ±0.1 inHg (0.3×10^3Pa) for each of the above size ranges, whereas the accuracy of the experimental setup was ±0.15 inHg (0.51×10^3Pa). Hence, under static conditions the PV gives repeatable results.

c. Spherical vs. Irregular Particles

Irregular and spherical particles of the same size range, -18, +20 mesh (850 to 1000μm) were used in experiments #1 and #10 (Table I) with the Sn/Al_2O_3 system. The required breakthrough pressure for irregular particles has been found to be 10% lower than that for spherical particles. Theoretically it is difficult to model breakthrough pressure for irregular particles since the radii of curvature cannot be easily defined.

d. Particle Valve Height

The height of the PV does not affect the failure pressures as long as there exist a few layers of well packed particles which remain

undisturbed by the motion of the liquid above the particles. By the same reasoning the cumulative porosity of the bed is immaterial as long as the liquid has to pass through a few constricted triangular openings of the type shown in Fig. 4a. In one of the runs (experiment #8, Sn/Al_2O_3 system with -16, + 20 mesh (850 to 1180μm) particles) doubling the height of the PV did not cause any significant change in the breakthrough pressure (1.9 inHg (6.4×10^3 Pa) as compared to 1.8 inHg (6.1×10^3Pa), the variation being within the experimental error).

Failure of the PV is sudden rather than gradual. This was verified experimentally by slowly cooling liquid Sn from 300°C while maintaining a constant pressure of 1.5 inHg (5.1×10^3Pa) equal to 83.3% of the actual failure pressure for -16, +20 mesh (850 to 1180μm) irregular particles. Inspection of the system after solidification of the tin showed no sign of leakage into the PV.

2. Disruption Mechanism of the Particle Valve

Various disruption mechanisms have been observed and characterized. By disruption it is understood that the packed layers of the Al_2O_3 beads forming the PV break up or float, causing premature leakage of the liquid. The various disruption mechanisms have been modeled to better understand quantitatively the governing parameters and thus the required critical variables to avoid disruption of the PV.

a. Failure Due to Direct Impingement of Liquid Droplets on the Particle Valve

The small spheres forming the PV behave as a thixotropic fluid because of their smooth surfaces and open packing and can easily be disturbed by mechanical forces. Assuming that a pool of metal does not exist above the particle bed, on first filling the vessel the liquid metal droplets falling unto the top surface layer of the PV can easily disrupt the PV and cause

leakage. Particularly for the case when the liquid metal possesses a much higher density than the Al_2O_3 particles (as in the case of molten steel), the momentum of the falling droplets may cause mechanical disruption of the particles. To avoid disruption requires that the top layer of the particles be bonded. Even when a small liquid pool rests on the particle bed, a droplet impinging on the pool will cause splashing of the liquid and will thus lose part of its energy in doing so; however, the droplet may still possess enough energy to move the particles of the PV mechanically. To avoid disruption the energy required to form a new drop (or to expose an area equivalent to a drop with a diameter equal to the height of the liquid pool, h) should be greater than that of the falling droplet, see Figure 8. The energy of a drop of radius, R, falling from a height H above the liquid pool is $\frac{4\pi R^3 \rho g H}{3}$, where ρ and g are the density of the liquid and the acceleration due to gravity, respectively. The energy required to create a new surface - a drop of diameter h (the height of the liquid pool) - is $\pi h^2 \gamma_{LV}$, where γ_{LV} is the surface tension. Thus, the criterion to avoid failure of the PV by this mechanism becomes

$$\frac{4\pi R^3 \rho g H}{3} \leq \pi h^2 \gamma_{LV} \tag{21}$$

To prevent failure either the height of the liquid pool, h, above the PV should be

$$h \geq \left(\frac{4\rho g HR^3}{3\gamma_{LV}}\right)^{1/2} \tag{22}$$

or the radius of the liquid droplet impinging unto the PV should be

$$R \leq \left(\frac{3h^2 \gamma_{LV}}{4\rho g H}\right)^{1/3} \tag{23}$$

Maximum allowable liquid droplets of molten steel that will not cause failure of the PV are tabulated in Table IV for various pool depths, h.

b. Failure by Augmented Hydrostatic Pressure Caused by an Impinging Liquid Droplet

When the height of the liquid pool is close to the supportable metallostatic head the PV will not be disturbed mechanically by the falling droplet, but the energy of the droplet might be sufficient to cause a dynamic metallostatic head greater than the breakthrough pressure.

The maximum kinetic pressure of the droplet on the liquid pool is given by ρgH, where H is again the droplet fall height. This impact pressure will vary inversely as the square of the distance from the impact area, so that the total (dynamic + static) head, $P_{(S+D)}$, at the PV will be:

$$P_{(S+D)} = \rho gH \left(\frac{R}{h}\right)^2 + \rho gh \quad (\text{for } R \leq h) \tag{24}$$

where ρ is the density of both the liquid pool and the droplet, R is the radius of the droplet, and h is the depth of the liquid pool. The existing pool depth h can be expressed as some fraction f of the maximum static supportable height or the critical height, h_c, i.e. $h = f \cdot h_c$. To avoid failure, the total head (dynamic plus static) should be less than the maximum equivalent static head in the absence of the dynamic component. The imposed criterion is:

$$P_{(S+D)} \leq \rho gh_c \tag{25}$$

In terms of the process variables, the maximum height H from which a liquid droplet of radius R can fall without causing failure of the PV is then:

$$H \leq \left(\frac{h_c}{R}\right)^2 \cdot f^2(1-f)h_c \tag{26}$$

Table V shows the behavior of Eq. (26) for various pool depths. For illustrative purposes the maximum static head, h_c, is assumed to be 10 cm. For example, for a given pool depth of 5 cm, the maximum height from which a

droplet 2.5 cm radius can strike the liquid pool above the PV is 20 cm. Larger droplets will cause failure of the PV. It can also be noted from Table V that there must be a small amount of liquid pool on the PV to prevent its failure caused by the impact pressure of droplets falling from heights greater than h_c. Once the initial cushioning pool has been established, the PV is quite safe until the static head exceeds 99% of the breakthrough pressure. In the present consideration it is assumed that the particles are not being disturbed mechanically by the impinging droplet (true for the case of a bonded or shielded PV). For an unbonded PV where the particles are loose and can be disturbed due to mechanical forces, these conditions apply only if the restrictions placed by Eq. (22) have already been satisfied, see Table IV.

For a bonded PV without a liquid pool resting on it, droplets falling from a height less than the critical head, h_c, will be unable to generate sufficient direct kinetic pressure to infiltrate the PV. For greater heights and dynamic pressures breakthrough may be only transient if the PV is well bonded. Since the metallostatic head may be insufficient to force the liquid to remain inside the PV, this liquid may simply be expelled back on top of the PV.

c. Failure Due to Buoyancy Forces Acting on Individual Particles - Flotation

Disintegration of the PV following breakthrough can occur due to density differences between the liquid phase and the beads. At breakthrough, the volume of pores between the particles is not completely filled with the liquid phase, resulting in an imbalance of forces and thus a net downward force on each particle. However, when pressures greater than the required breakthrough pressure are applied, the envelopment of each particle by the liquid phase will increase, and thus there may be a possibility of disruption

of the PV due to the unbalanced buoyancy forces.

The pertinent forces have been calculated and are shown in Appendix III-A. The results indicate that the greater the applied infiltration pressure (expressed as a multiple N of the required breakthrough pressure), the greater the force holding down the particles. However, the larger the particles are, the more is the buoyant force, so that there is a critical size of particles for which the particles will float as soon as infiltration begins.

The restriction on r, the radius of the particles used, as derived in Appendix III-A is:

$$r \leq \left[\frac{10.15\ \gamma_{LV}\ N \sin^2\alpha}{\Delta\rho g}\right]^{1/2} \qquad (27)$$

where

$$N = \frac{\text{applied infiltration pressure, } P_i}{\text{required breakthrough pressure, } P_{BR}}$$

α = half angle describing the area of the particle not in contact with the liquid phase, see Fig. A2.

$\Delta\rho$ = density differential between the liquid phase and the alumina beads.

Table VI shows the calculated values of r, the critical particle radius for the steel/Al_2O_3 system below which disintegration of the PV will not occur following infiltration, for different values of $P_i = N \cdot P_{BR}$ (calculated by the use of Eqs. (A14) to (A17) as derived in Appendix III-A). It should be noted that for the steel/Al_2O_3 system and for $P_i = P_{BR}$, the critical particle radius is 0.867 cm (Table VI) which is too large to be of any practical consequence.

3. Practical Considerations

As has previously been shown, the breakthrough pressure for a particular size of refractory particles is a function of both the surface tension and contact angles. Hence, the surface tension and the apparent advancing contact angles for a particular melt/PV system need to be known fairly accurately for the correct estimation of the supportable metallostatic head. This is particularly important when the effect of alloying elements is considered; small traces of surface-active elements in the melt may cause considerable reductions in the surface tension and contact angles.

Halden and Kingery[16] studied the effect of C, N, O and S on the liquid iron surface tension and interfacial energy with Al_2O_3 and arranged them as S > O > N > C in order of decreasing surface activity. They reported the value of surface tension, γ_{LV} = 1632 dyne/cm (1632 mN/m), and the contact angle θ = 147.5° for an Fe-0.0077% O - 0.009% C - 0.005% S melt as compared to γ_{LV} = 707 dyne/cm (707 mN/m) and θ = 100.8° for an Fe-0.0398% O - 0.004% C - 2.0% S melt. This would correspond to a 90% decrease in the calculated breakthrough pressure. Such drastic lowering of the $|\cos\theta|$ term with varying contact angles can render the PV completely unreliable; therefore, highly surface-active elements like S and O need to be carefully controlled. Elements which by themselves are not surface-active in the melt may be quite surface-active in the presence of each other.[17]

Besides changing the surface energies of the system directly, the alloying elements can also cause premature failure of the PV by producing elemental metal vapor or a volatile metal-oxygen compound which can coat the refractory particles and thus change their wetting characteristics. Svoboda and Geiger[18] have shown that for the Fe-Mn system mass transport takes place by formation of volatile polynuclear oxides and that maximum vaporization into a porous

aggregate occurs at oxygen partial pressures which are slightly less than those required for the liquid oxide to reach an equilibrium state. Furthermore, the vaporization stops when a liquid oxide layer is present - i.e. when partial pressure of oxygen is greater than the equilibrium pressure. Therefore, to prevent failure of the PV caused by diffusion of vapor species into the porous aggregate, metallic alloying elements that are easily volatized or form an easily volatized oxide are to be avoided.

III.E CONCLUSIONS

1. A particle valve (PV) consisting of a bed of coarse, non-wetting refractory (Al_2O_3) beads may be used as a quick release valve for liquid metals.

2. The PV has numerous metallurgical applications and has successfully been utilized in bottom-pour atomization where the PV isolates the liquid steel from the exit orifice.

3. An expression for the required breakthrough pressure for the liquid to penetrate the PV has been derived: $\Delta P = -10.9 \left(\frac{\gamma_{LV}}{d}\right) \cdot \cos \theta'_A$.

4. Experimental breakthrough pressures were measured in the Sn/Al_2O_3 and Hg/Al_2O_3 systems. Excellent agreement was found between the theoretical and experimental results.

5. Based on numerous experiments, it can be concluded that the PV is reliable; the required breakthrough pressure does not depend on the PV height; and spherical or irregular particles may be employed to construct the PV.

6. Various failure mechanisms of the PV have been observed, characterized and modeled.

REFERENCES

1. G. Langford, R. E. Cunningham: Metallurgical Transactions, 1978, Vol. 9B, p.5.

2. D. Apelian, G. Langford: Rapid Cycle Steel Castings, proposal submitted to ARPA, January 24, 1977.

3. D. Apelian, M. C. Flemings, R. Mehrabian: Journal of Materials Science, 1975, 10, p. 460.

4. K. Brondyke, P. D. Hess: Trans. AIME, 1964, vol. 230, p. 1553.

5. H. P. G. D'Arcy: "Les fontaines publiques de la ville de Dijon", Victor Dalmont, Paris, 1856.

6. A. E. Scheidegger: "The Physics of Flow Through Porous Media", p. 115, University of Toronto Press, 1957.

7. P. C. Carman: "Fundamental Principles of Industrial Filtration", Trans. Inst. Chem. Engrs. (London), 1937, vol. 15, p. 168.

8. N. K. Adam: Discussions Trans. Faraday Society, 1948, 3, p. 5.

9. P. C. Carman: Discussions Trans. Faraday Society, 1948, 3, p. 72.

10. L. C. Graton, H. J. Fraser: Journal of Geology, 1935, vol. 43, No. 8, part 1, p. 785.

11. R. P. Mayor, R. A. Stowe: Journal of Colloid Science, 1965, vol. 20, p. 893.

12. L. K. Frevel, L. J. Kressley: Analytical Chemistry, 1963, vol. 35, part 2, p. 1492.

13. B. C. Allen, W. D. Kingery: Trans. of the Metallurgical Society of AIME, 1959, vol. 215, p. 30.

14. A. B. D. Cassie: Discussions Trans. Faraday Society, 1948, 3, p. 11.

15. R. Shuttleworth, G. L. J. Bailey: Discussions Trans. Faraday Society, 1948, 3, p. 16.

16. F. A. Halden, W. D. Kingery: Journal of Phys. Chemistry, 1955 vol. 59, p. 557.

17. P. Kozakevitch, "Surface Phenomena of Metal" p. 223, Society of Chemical Industry monograph no. 28, 1968.

18. J. M. Svoboda, G. H. Geiger: Trans. of the Metallurgical Soc. of AIME, 1969, vol. 245, p. 2363.

TABLES

Table 1: Experimentally measured and calculated breakthrough pressures for the Sn/Al_2O_3 system (spherical and irregular particles)

Expt.*	Particle Size		$\frac{1}{d_{avg}}$ (cm^{-1})	ΔP**(inHg) Experimental	ΔP**(inHg) Theoretical	% Error
	Mesh No.	Size (cms)				
1a	-18 +20	0.1-0.085	10.81	2.3	2.02	12.2
1b	-18 +20	0.1-0.085	10.81	2.3	2.02	12.2
2a	-25 +30	0.071-0.06	15.26	3.0	2.90	3.3
2b	-25 +30	0.071-0.06	15.29	2.9	2.90	0.0
3	-35 +40	0.05-0.0425	12.62	4.3	4.05	5.8
4	-40 +45	0.0425-0.0355	25.64	5.3	4.80	9.4
5	-45 +50	0.0355-0.03	30.53	5.9	5.71	3.2
6	-16 +20	0.118-0.085	9.85	1.7	Irregular Particles	
7	-16 +20	0.118-0.085	9.85	1.8		
8	-16 +20	0.118-0.085	9.85	1.9***		
9	-16 +20	0.118-0.085	9.85	1.8		
10	-18 +20	0.1-0.085	10.81	2.1		

* Experiments 1 through 5 are with spherical particles.
Experiments 6 through 10 are with irregular particles.

** 1 inHg = 3.38638×10^3 Pa
1 psi = 6.894757×10^3 Pa

*** PV height was double (3.0 cm).

Table II. Experimentally measured and calculated breakthrough pressures for the Hg/Al_2O_3 system (spherical particles).

Expt.	Particle Size		$\frac{1}{d_{avg}}$ (cm^{-1})	ΔP*(inHg) Experimental	ΔP* (inHg) Theoretical	%Error
	Mesh Size	Size (cm)				
11	-20 +25	0.085-0.071	12.82	2.2	2.0	9.1
12	-25 +30	0.071-0.06	15.26	2.6	2.38	8.5
13	-30 +35	0.06-0.05	18.18	2.8	2.85	-1.8
14	-35 +40	0.05-0.0425	21.62	3.3	3.38	-2.4
15	-40 +45	0.0425-0.0355	25.64	4.2	4.01	4.5
16	-45 +50	0.0355-0.03	30.534	4.9	4.78	2.5

* 1 inHg = 3.38638×10^3 Pa

1 psi = 6.894757×10^3 Pa

Table III. Experimentally measured and calculated breakthrough pressures for the Hg/glass microbeads system - Frevel and Kressley's data(12).

Particle Size	d_{avg} (cm)	ΔP, (psi) Experimental from Frevel & Kressley (12)	ΔP^{*}, (psi) Theoretical - Eq. (8) from Frevel & Kressley (12)	ΔP^{*}†, (psi) Theoretical - Eq. (18) this paper
-35 +40 mesh 0.0425-0.05cm	0.0462	1.2	-	1.24 3.3% Error
-65 +70 0.016-0.021cm	0.0185	3.01	2.75 8.6% Error	3.11 3.3% Error

* For the Hg/glass system:

$\theta_A' = 140°$

$\gamma_{LV} = 474$ dyne/cm ($\equiv$474 mN/m)

† 1 psi = 6.894757×10^3 Pa

1 inHg = 3.38638×10^3 Pa

Table IV. Maximum allowable radius of molten steel droplet, R (cm), falling from a height, H, unto a liquid pool of depth, h, which will not cause failure of the PV - Eq. (23).

$h_{(cm)}$ \ $H_{(cm)}$	1	2	5	10	15	20
1	0.547*	0.434	0.321	0.252	0.222	0.200
2	0.869	0.690	0.508	0.404	0.353	0.321
5	1.601	1.270	0.936	0.743	0.649	0.590
10	2.541	2.017	1.486	1.179	1.030	0.936

* The following values were used in the calculations:

γ_{LV}(steel) = 1500 dyne/cm (≡ 1500 mN/m)

ρ = 7 gm/cm^3 (7 x 10^3 kg/m^3)

g = 980 cm/s^2 (9.8 m/sec^2)

Table V. Maximum height, $H^{\dagger}_{max}$ (cm), from which a droplet of radius, R, can fall into the liquid pool of depth, h, without causing breakthrough.

f*	0.01	0.025	0.1	0.25	0.50	0.75	0.90	0.99	1.0
R(cm) \ h(cm)	0.1	0.25	1.0	2.5	5.0	7.5	9.0	9.9	$h=h_c^{**}$
0.01	1,000	large	large	large	large	large	large	large	0
0.025	160	1,000	large	large	large	large	large	large	0
0.1	10	61	900	large	large	large	large	1,000	0
0.25	NA††	10.0	140	750	large	large	1,300	160	0
1.0	NA	NA	9.0	47	130	140	81.0	10.0	0
2.5	NA	NA	NA	8.0	20.0	23.0	13.0	1.6	0

* f = fraction of maximum supportable head = $\frac{h}{h_c} = \frac{h}{10}$

** The maximum static head, h_c, is assumed to be 10.0 cm.

† $H_{max} = \frac{h_c^3 f^2(1-f)}{R^2}$ as described by Eq. (26).

†† R > h in Eq. (26) and is thus not applicable, NA.

Table VI. The maximum allowable particle radius r, above which the PV will fail for infiltration pressure of $Pi = N \cdot P_{BR}$ for the low carbon steel/Al_2O_3 system.

$n = \frac{r}{R_1}$	$\alpha(degrees)$ $\cos^{-1}(\frac{n}{n+1})$	$N = f(\alpha)$	r (cm)* critical particle radius
7.66	27.8	1	0.867
10	24.61	1.38	0.909
25	15.94	3.88	1.005
100	8.07	16.88	1.072
250	5.12	43.35	1.092
1000	2.56	177.93	1.107
2000	1.81	358.4	1.111

* Calculated using Eq. (A17).

Note: γ_{LV}(steel) = 1500 dyne/cm (1500 mN/m)

$\Delta\rho$ = 4.5 gm/cm^3 (4.5 x 10^3 kg/m^3)

g = 980 cm/s^2

FIGURES

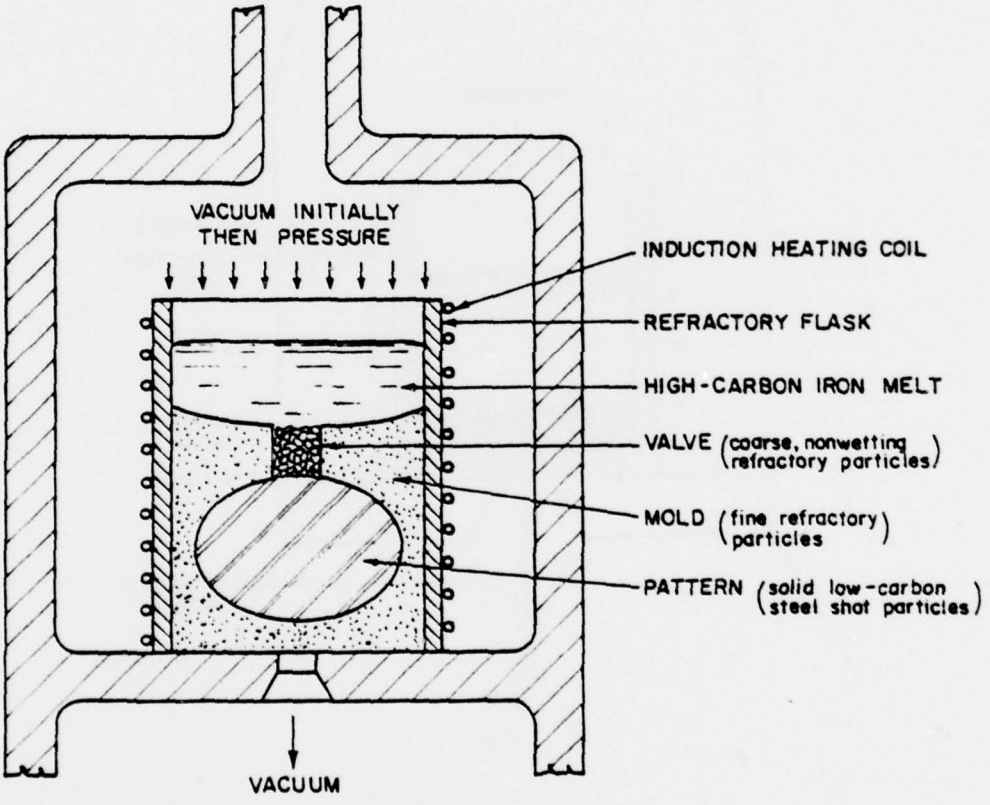

Figure 1. General arrangement for steel casting by diffusion solidification.

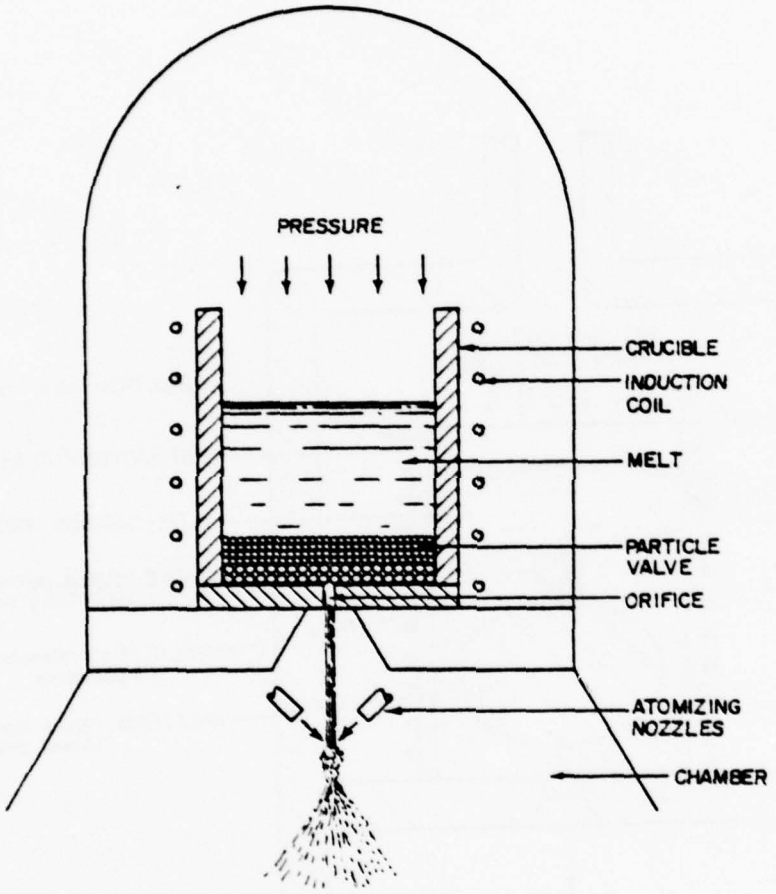

Figure 2. Atomization process where the PV separates the melt from the orifice.

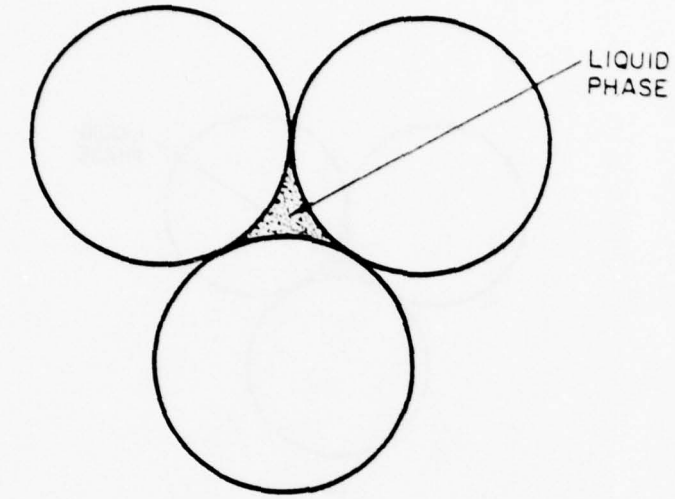

(a)

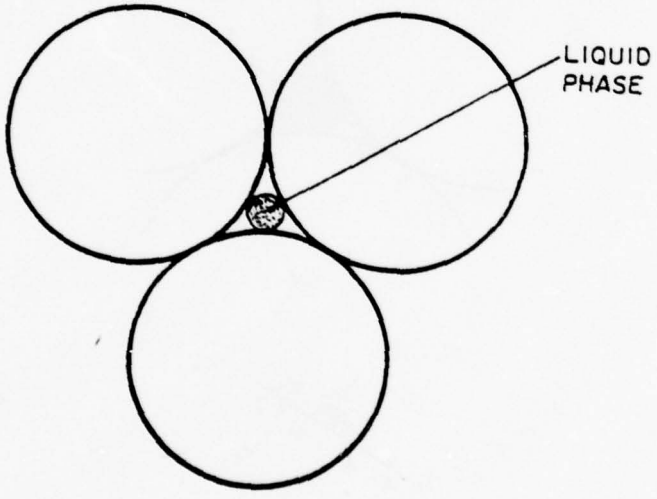

(b)

Figure 3. Triangular orifice formed by three touching spheres and assumed liquid phase geometries for calculating breakthrough pressure using the concept of hydraulic radius.

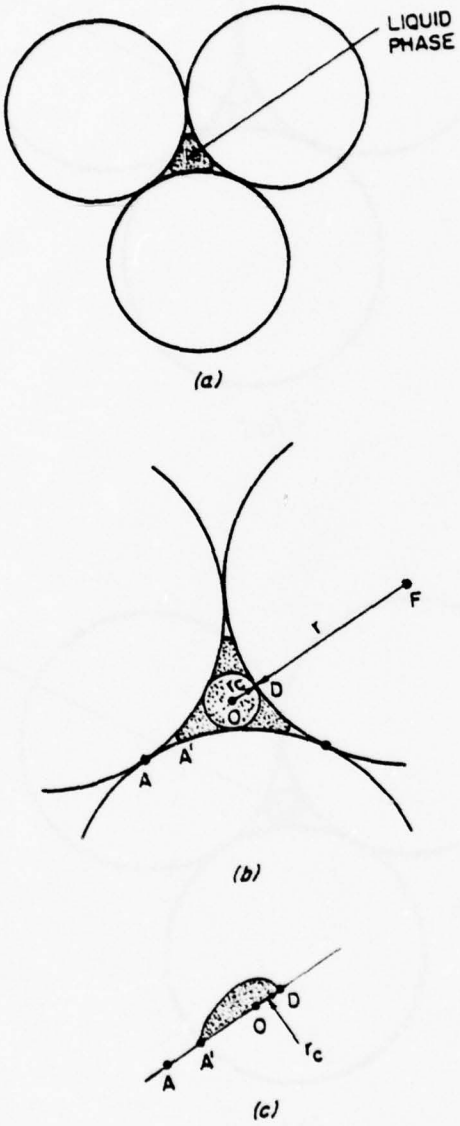

Figure 4. Assumed geometry for calculating breakthrough pressure using radii of curvature.
(a) Triangular orifice and assumed liquid phase geometry.
(b) Cross sectional view of liquid parallel to plane of the paper.
(c) Cross sectional view of liquid perpendicular to the plane of the paper.

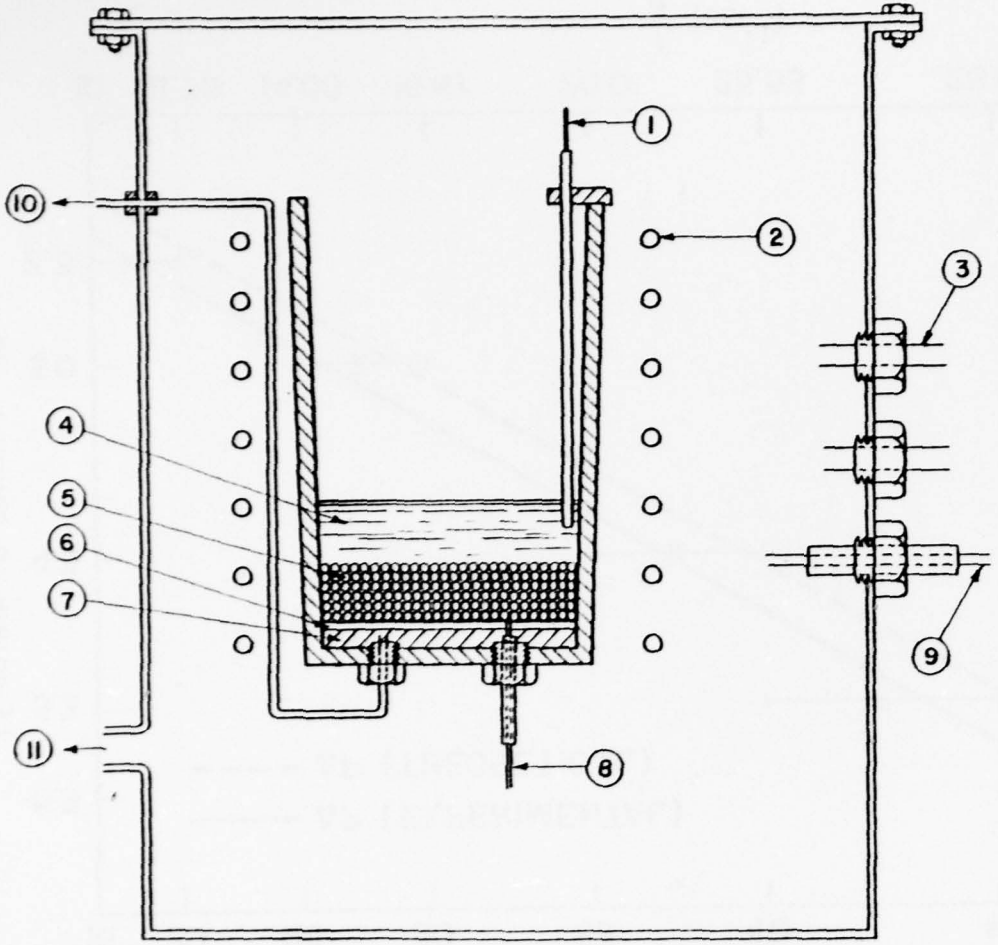

1. Thermocouple
2. Induction coil
3. Induction coil lead
4. Melt
5. PV (Al_2O_3 beads)
6. Fine Al_2O_3 powder
7. Fiberfrax
8. Open-ended thermocouple
9. Thermocouple leads
10. Tube open to atmosphere via a valve and bubble tube
11. Vacuum and gas pressurization

* Points 10 and 11 are connected by a manometer.

Figure 5. Schematic diagram of the apparatus used for Sn/Al_2O_3 system.

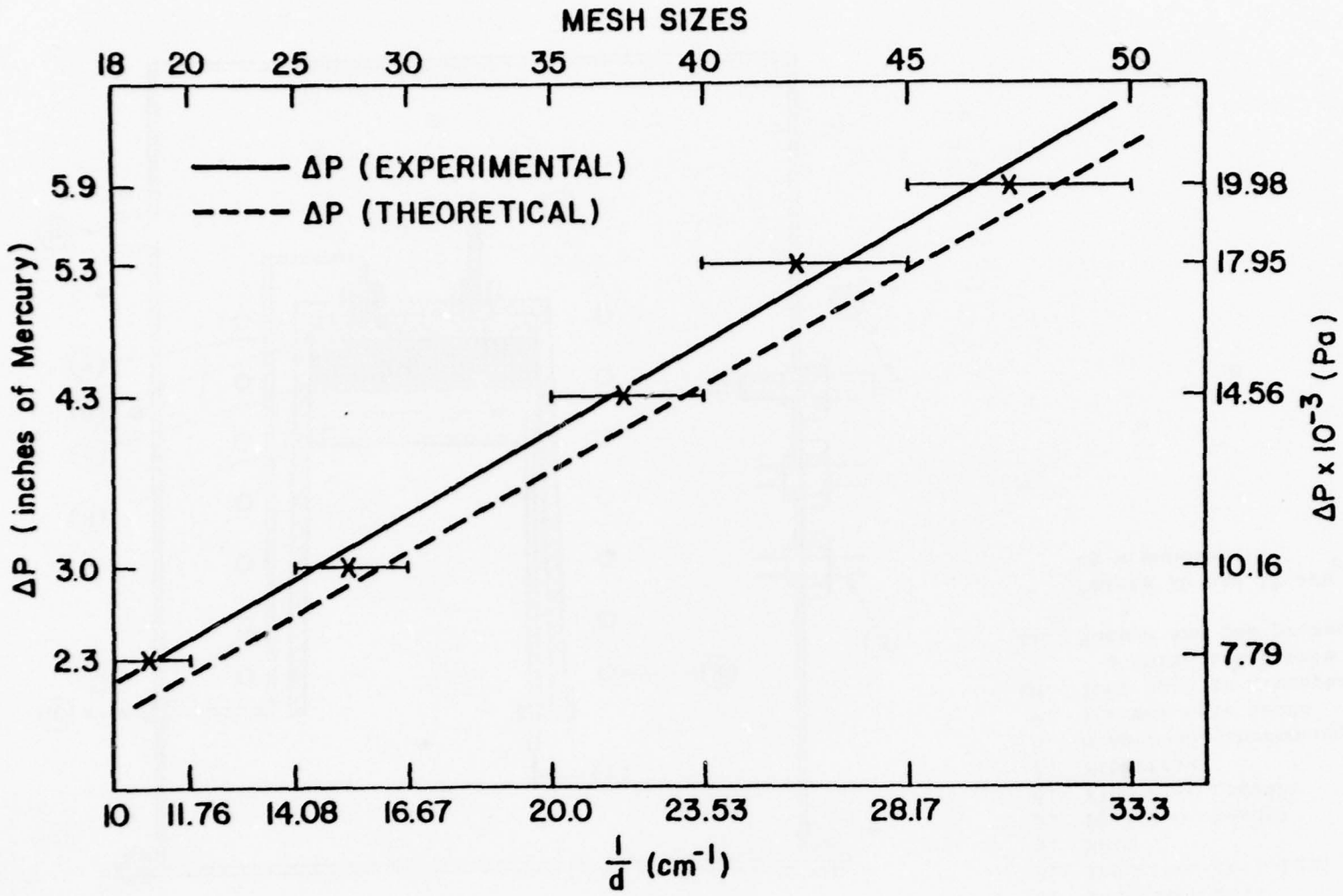

Figure 6. Theoretical and experimental breakthrough pressure for the Sn/Al_2O_3 PV system.

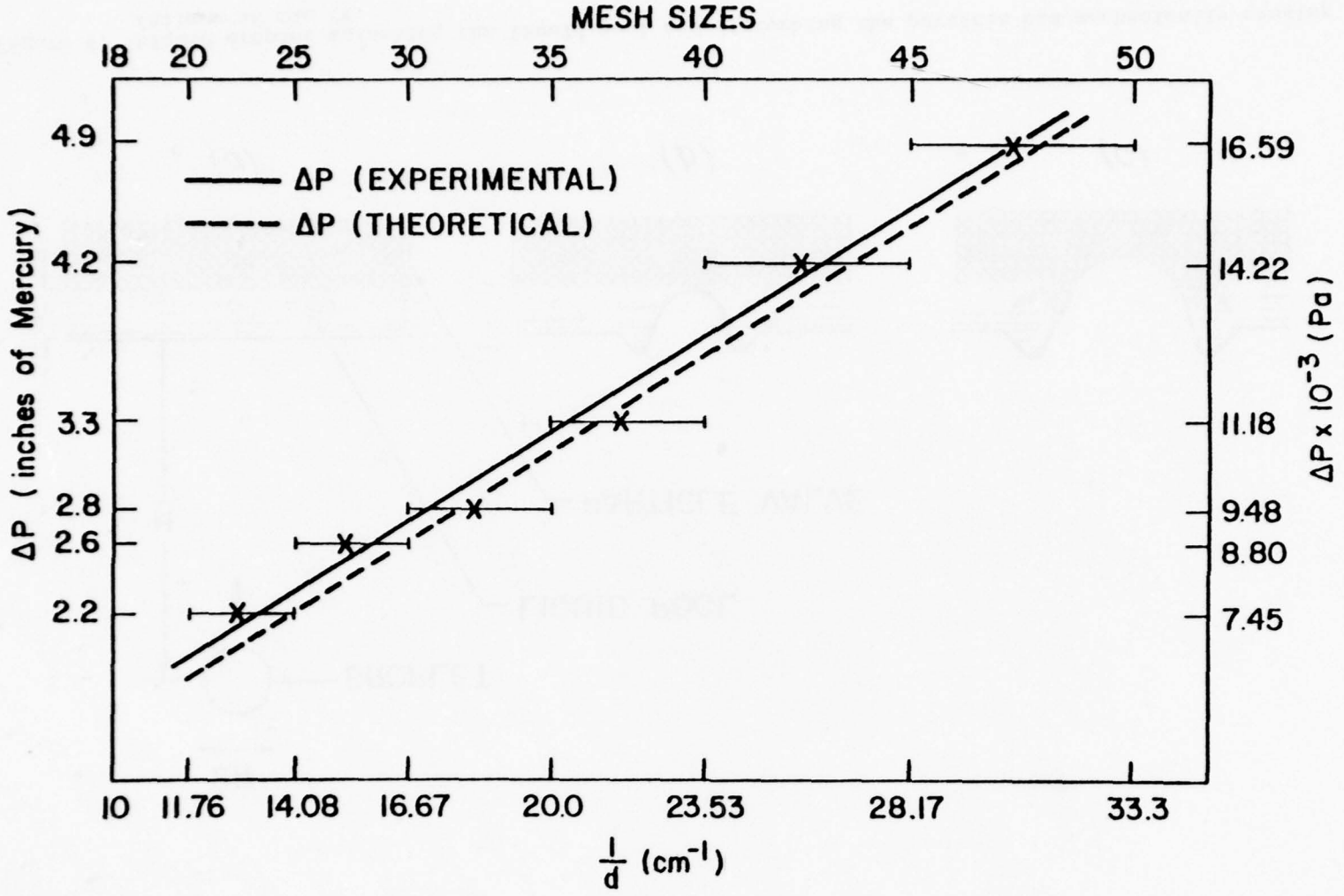

Figure 7. Theoretical and experimental breakthrough pressure for the Hg/Al_2O_3 PV system.

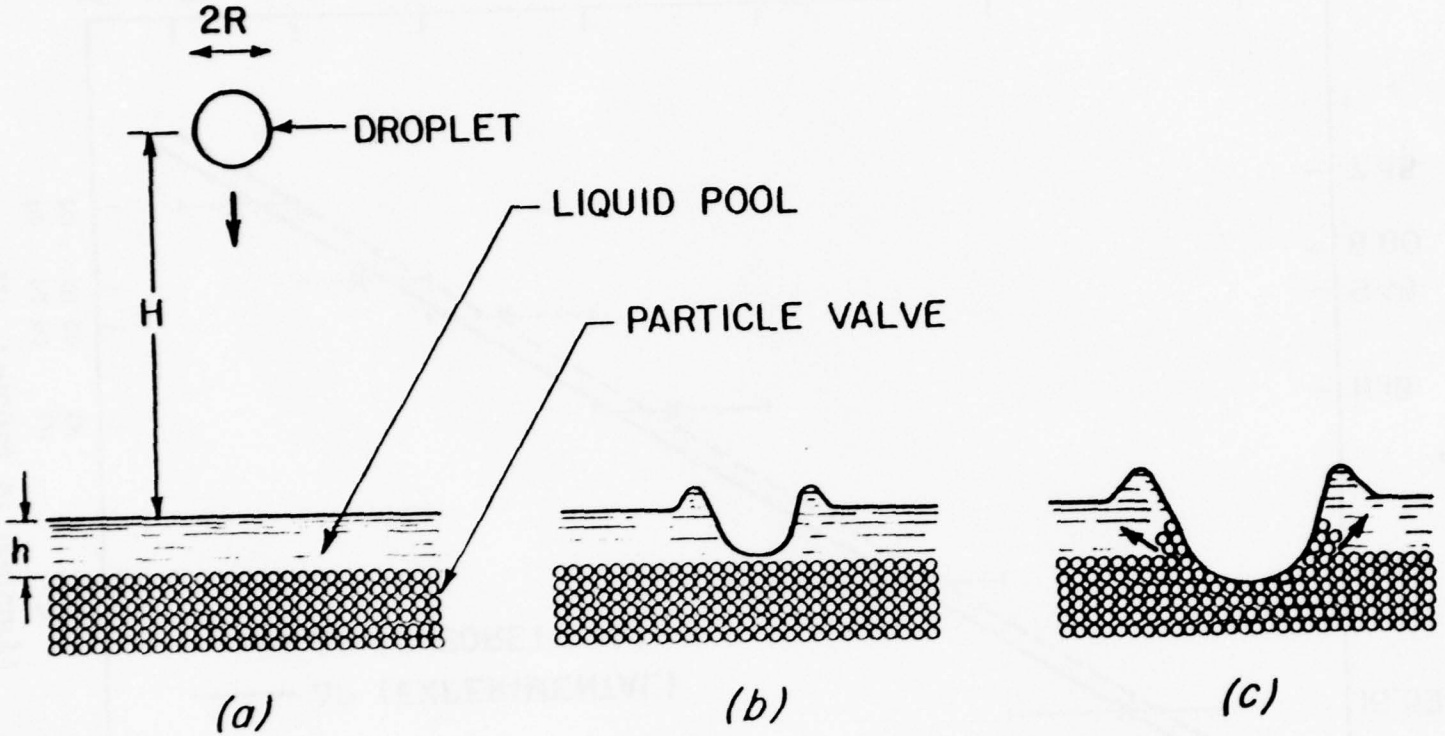

Figure 8. Liquid droplet splashing the liquid pool and disturbing the particle bed mechanically causing failure of the PV.

APPENDIX III-A. PARTICLE SIZE REQUIREMENT TO AVOID FAILURE OF THE PV BY BUOYANCY FORCES

Consider a particle which is resting above three other particles as shown in Fig. A1. Following infiltration of the liquid phase through the PV, the forces acting on this individual particle are the buoyant force, B, and the resultant downward vertical force, F_i, resulting from the applied infiltration pressure, P_i.

The buoyant force is given by

$$B = \frac{4}{3}\pi r^3 \quad \Delta\rho \quad g \tag{A1}$$

where $\Delta\rho$ = density differential between the liquid phase and the particles.

r = radius of the particles.

The downward force, F_i is given by

$$F_i = P_i \cdot A_p \tag{A2}$$

where P_i = applied infiltration pressure

A_p = projected area of the spherical cap not in contact with the liquid phase - see Fig. A2.

To express the applied infiltration pressure, P_i, as a function of the particle size of the beads and the required breakthrough pressure, one must first calculate the pertinent radii of curvature. Fig. A2 shows the assumed geometry of the liquid meniscus at each particle contact point. From geometrical considerations, the principal radii of curvature, R_1 and R_2, can be expressed as a function of α, the half angle sustained by the unwetted portion of the particles:

$$R_1 = r\left(\frac{1}{\cos \alpha} - 1\right) \tag{A3}$$

$$R_2 = r \sin \alpha \tag{A4}$$

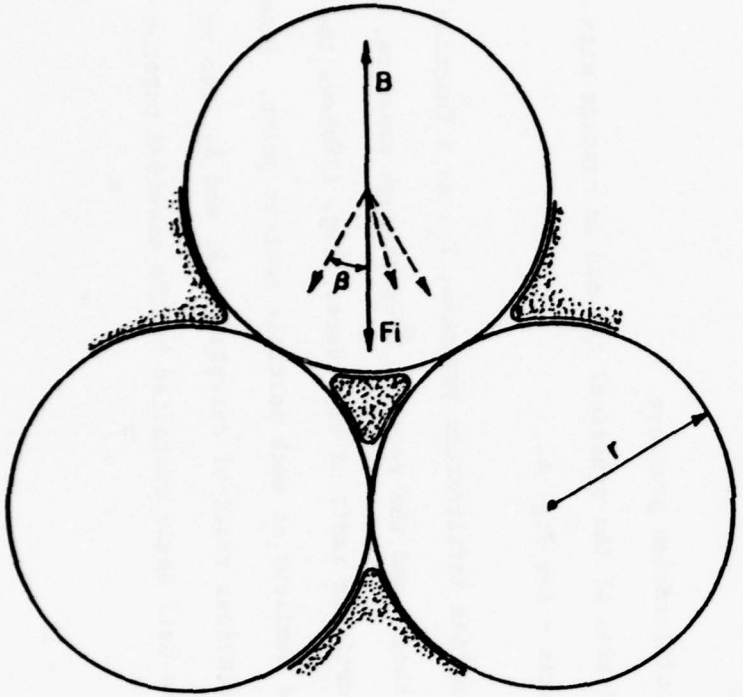

Figure A1. Forces acting on a particle after the liquid has infiltrated the PV. The top particle is resting on three other particles though only two are shown.

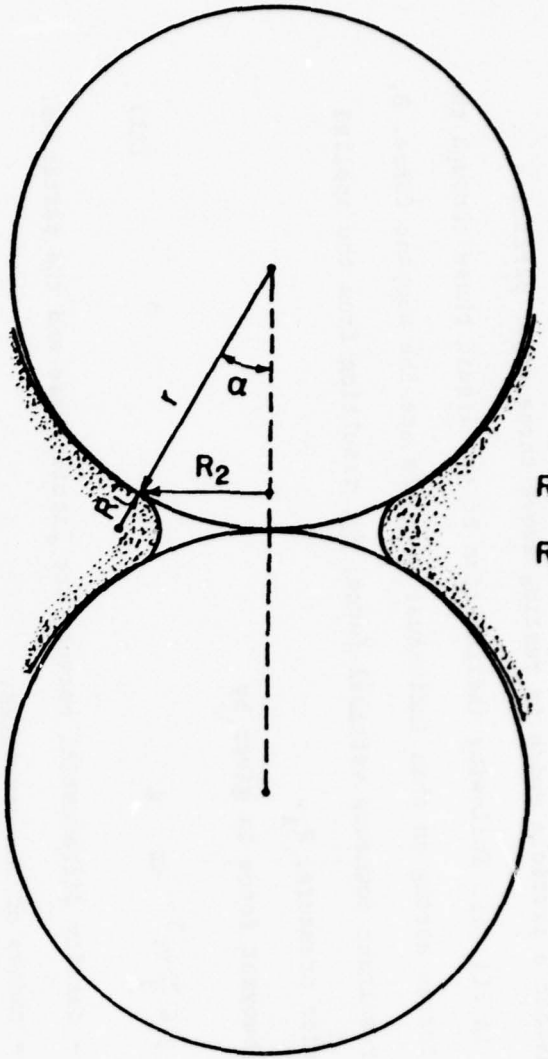

Figure A2. Geometry and radii of curvature of liquid, around two particles, following infiltration.

The applied infiltration pressure P_i, is:

$$P_i = \gamma_{LV} \left[\frac{1}{r \sin \alpha} - \frac{1}{r\left(\frac{1}{\cos \alpha} - 1\right)}\right] \cos \theta'_A \qquad (A5)$$

for cases when $\theta'_A = 180°$, Eq. (A5) simplifies to:

$$P_i = \frac{\gamma_{LV}}{r} \left[\frac{\cos \alpha}{1 - \cos \alpha} - \frac{1}{\sin \alpha}\right] \qquad (A6)$$

For the same infiltration pressure, and when θ'_A is less than 180° the liquid meniscus will penetrate further, i.e. α will decrease. On the other hand, the theoretical breakthrough pressure, P_{BR}, as a function of the bed particle size is

$$P_{BR} = \frac{11\ \gamma_{LV}}{2r} \qquad (A7)$$

The applied infiltration pressure can now be expressed as some multiple N of the required theoretical pressure

$$P_i = N \cdot P_{BR} \qquad (A8)$$

The use of the Eqs. (A6) and (A7) yields N as a function of the half angle α:

$$N = \frac{\frac{\cos \alpha}{1 - \cos \alpha} - \frac{1}{\sin \alpha}}{5.5} \qquad (A9)$$

The projected area, A_p, of the spherical cap not in contact with the liquid phase on the horizontal plane is given by $\pi R_2^2 \cos \beta$, where $\cos \beta$ is the direction cosine - see Fig. A1. The downward resultant force, F_i, can now be expressed:

$$F_i = N \left(\frac{5.5\ \gamma_{LV}}{r}\right)(3 \cos \beta)\ \pi r^2 \sin^2 \alpha. \qquad (A10)$$

For this particular case, β is approximately 35°, thus:

$$F_i = 13.53\ N\ \pi\ \gamma_{LV}\ r\ \sin^2\alpha \qquad \text{(A11)}$$

To avoid failure by flotation of the beads, the net downward force, F_i must be greater than the upward buoyancy force, B. Use of Eqs. (A1) and (A11) yields the imposed criterion:

$$r \leq \left[\frac{10.15\ \gamma_{LV}\ N\ \sin^2\alpha}{\Delta\rho\ g}\right]^{1/2} \qquad \text{(A12)}$$

When N equals unity, then P_i equals P_{BR}, and the angle α equals 27.8° - Eq. (A9). Subsequently, for values of N greater than unity the angle α will be less than 27.8°.

Alternatively, we can define a variable n, the ratio of particle radius, r, to the one principal radius, R_1:

$$n = \frac{r}{R_1} = \left(\frac{1}{\cos\alpha} - 1\right)^{-1} \qquad \text{(A13)}$$

(when N equals unity, α is equal to 27.8° and thus n equals 7.66).

The working relations are:

$$n = \frac{r}{R_1} \qquad \text{(A14)}$$

$$\alpha = \cos^{-1}\left(\frac{n}{n+1}\right) \qquad \text{(A15)}$$

$$N = \frac{\left(\frac{\cos\alpha}{1-\cos\alpha} - \frac{1}{\sin\alpha}\right)}{5.5} \quad \text{and} \qquad \text{(A16)}$$

$$r \leq \left[\frac{10.15\ \gamma_{LV}\ N\ \sin^2\alpha}{\Delta\rho\ g}\right]^{1/2} \qquad \text{(A17)}$$

IV. PROVISION OF CONTROLLED QUALITY LOW-CARBON STEEL SHOT AND CONSTRUCTION OF THE RESEARCH SD CASTING FURNACE - TASK 3

C. Lall
D. Apelian
G. Langford
H. Sreshta
M. Paliwal

SUMMARY

Apparatus for the gas atomization of liquid metals, SD casting of steels and decarburization of impure steel shot has been designed and constructed. The operation and main features of each unit are briefly described. Steel particles obtained in a preliminary run of the gas atomization unit are shown. Also, a section through a steel casting made by the diffusional solidification (SD) technique is shown.

TABLE OF CONTENTS: Section IV. Provision of Controlled Quality Low-Carbon Steel Shot and Construction of the Research SD Casting Furnace - Task 3.

IV.A Introduction 158

IV.B Gas Atomization of Liquid Metals 159

IV.C Decarburization of Steel Powders 161

IV.D SD Casting Furnace 162

References 163

Figures 164

Appendix IV-A: Degassing of Melts by Bubbling with Argon 172

Appendix IV-B: Thermodynamics and Kinetics of Decarburization 176

IV.A INTRODUCTION

Several phases of the present research program require high quality spheroidal metal particles as the starting raw material. The ability to produce the shot at Drexel University offers many advantages. The most important reason is that the metal particles must be of a consistently high quality which mandates that the manufacturing process be rigorously controlled and monitored. In SD castings it is important to minimize the total amount of oxygen as the ductility of the casting decreases with increasing content of oxides[1]. A further reason for having our own facility is that it offers much more flexibility; virtually any metal or alloy may be atomized and the chemical composition of the shot may be modified as required. The ability to make alloy additions is also required since both the liquid and the shot will be prealloyed when making tool steels or high strength low alloy steels. There are many techniques for producing metal powders as described in recent reviews (e.g. Dixon[2] and Lawley[3]). The method being developed at Drexel University involves the atomization of a liquid metal stream by a cross-current stream of inert gas and is described below in section IV.B.

Alternatively, methods by which high quality particles can be derived from commercially available impure shot have also been investigated. As described in section IV.C, a decarburization apparatus has been built in which impure shot is heated under a suitable atmosphere to decarburize or deoxidize and thus produce good quality shot.

Various process logics have been porposed for rapid cycle casting of steels[1]. An apparatus to make the SD castings under laboratory conditions has been designed and constructed and is described in section IV.D.

IV.B GAS ATOMIZATION OF LIQUID METALS

Overall views of the gas atomization unit are shown in Figs. 1 and 2. The apparatus consists of two chambers (Fig. 2); an upper one to melt the charge and a lower one to break up the liquid stream and cool the atomized particles. A more detailed sketch of the melting furnace in the dome or upper chamber assembly is shown in Fig. 3.

The first step in the atomization process is to completely evacuate the whole system and back fill with inert gas. This is done twice to minimize the residual air in the system. A continuous, low, flow-rate of inert gas is maintained thereafter to keep the inside pressure greater than atmospheric.

The assembly inside the dome is heated by two induction coils which couple to the graphite susceptor (#5, Fig. 3). The heat is transferred to the alumina crucible, and thereby the melt, by radiation and gaseous conduction. When the crucible temperature is near 1600°C the charge, consisting of a half inch (13 mm) diameter rod, is lowered through a teflon gland into the crucible. As the tip of the rod is melted off, more and more charge is introduced until a sufficient amount of melt is obtained.

The melt is accumulated above the particle valve (#6, Fig. 3), which consists of carefully graded alumina particles. This valve has two layers: 0.5 in (13mm) depth of coarse particles on top of which is 1.0 in (25 mm) of fine particles. The size of the fine particles must be carefully chosen so as to sustain the pressure of the molten metal head but not so fine as to need excessive pressure to force liquid through to the orifice. Recent work at Drexel University, as reported in Section III (Task 2), gives the required breakthrough pressures for different particle sizes. The size of the coarse particles is not critical but should be less than seven times the diameter of the small particles so that the latter will not filter through. Preliminary tests on

the atomization unit indicate that a 6 inch (150 mm) head of 1018 steel may be safely supported by -30,+35 mesh (500μm < x < 600μm) tabular alumina particles. The coarser layer consisted of -16, +18 mesh (1000μm < x < 1180μm) particles. The top of the particle valve is protected by a loose-fitting alumina disc, and the orifice is protected by an alumina baffle to prevent blockage by the coarse particles. A pressure of 15 psi (110 kPa) above the melt is more than adequate to push the liquid through the alumina bed.

When a sufficient amount of melt has been obtained, the steel may be deoxidized by bubbling with high purity argon, which also ensures vigorous mixing of the melt. Details of the deoxidation process and practice are given in Appendix IV-A. At this stage any necessary alloy additions may also be made; FeO or CO may be added to control inclusion content.

The temperature variation along the length of the crucible has to be carefully controlled. To monitor the temperature, several thermocouples are inserted through the graphite susceptor and touch the outside of the crucible tube at various positions along its length. Another thermocouple is located below the orifice disc, in the graphite susceptor base. A potential problem is the precipitation of alumina in the orifice during atomization, since the liquid steel dissolves the crucible material. This may be overcome by keeping the steel slightly undersaturated with respect to alumina at the orifice, which is achieved by simply keeping the orifice slightly warmer than the melt. This leads to another problem which is encountered in the continuous casting of steels - orifice erosion (Singh[4]). However, in the present application the orifice diameter is not a crucial parameter so that the same orifice may be used for several runs, as long as the orifice temperature is maintained as low as possible during atomization.

Once the correct temperatures have been obtained the melt is ready to be pushed through the particle valve for subsequent atomization. This is achieved by collecting high pressure inert gas in an accumulator and opening it to the dome (rapid pressurization prevents "dribbling" at the orifice). The pressure differential between the dome and the lower chamber forces the liquid steel through the particle valve, the orifice and into the lower chambar. Inert gas at high pressure is emitted through radially positioned nozzles to break up the stream of liquid steel. Most of the metal particles solidify during their free fall and bounce their way to the bottom, cooling off as they do so. The cooling rate of the steel particles may be altered by using gases of different conductivities (e.g. argon, nitrogen or helium) in the lower chamber. Excess gas is expelled through a large check valve (#20, Fig. 2).

A stainless steel baffle is used to prevent the shot or unatomized liquid from falling directly into the stainless steel container (catcher) at the bottom (Fig. 2). The latter is filled with inert gas, a fluidized bed with water-to-gas heat exchanger, or cooled with liquid nitrogen in order to cool the shot to room temperature. Representative steel shot produced via the above described atomization process are shown in Fig. 4.

IV.C DECARBURIZATION OF STEEL POWDERS

As an alternative to the gas atomization process, high quality steel particles can be made from less pure forms which are readily available commercially. The high levels of carbon and/or oxygen present in the commercial material must be removed before it is useful for SD casting. This may be achieved by use of a decarburization furnace, which has been completed and is shown schematically in Fig. 5. A suitable ratio of gases ($CO/CO_2/N_2$) is premixed and forced through a bed of iron particles which serves

to preheat the incoming gas mixture. The mixture passes through a tube and then into the region where the impure shot is contained. The unit is designed to allow analysis of both the incoming and the outgoing gases. Appendix IV-B gives the reactions involved in the decarburization process and presents calculations on the thermodynamics and kinetics of the process.

IV.D SD CASTING FURNACE

A sketch of the modular SD casting furnace as recently completed is shown in Fig. 6. The peripheral gas lines and other auxiliary equipment of both the atomization and the SD casting furnace are similar so that the melting section of the atomization unit can also be used as a casting furnace.

The dome assembly (Fig. 6) is completely evacuated and backfilled with high purity argon prior to heating. As the assembly is heated by the induction coils, the system is kept under a dynamic vacuum. This allows a chance for the charge (both the cast iron and the low carbon steel shot) to be degassed. Even when the cast iron is molten gases may still evolve from the shot so an alumina vent tube is placed just above the shot for this purpose. The melt may be purified by bubbling with Argon by means of the central alumina tube. When the melt and shot are at the selected temperatures, the dome is pressurized within a fraction of a second by opening the chamber to the accumulator (Fig. 6) transferring the melt into the particle bed of steel shot; melt transfer pressures of up to 150 psi (1.034×10^3 Pa) are possible.

The SD casting portion of the atomization unit is arranged so that the bottom of the mold may be kept open to vacuum while the top is pressurized, preventing entrapment of residual gases in the bottom of the mold by the advancing liquid during infiltration of the casting. The other unit (Fig. 6) has a solid bottom; castings made in this unit must have a permeable mold or alternative outgassing means (see Langford and Cunningham[5]).

The SD casting furnaces will be used to provide samples of SD castings for tests and evaluations both in-house and by DoD agencies. Two such castings have already been made during shakedown runs. A macrophotograph of one of these castings is shown in Fig. 7. Note that the structure is homogeneous (in spite of the lack of sufficient infiltration pressure) and that the infiltration takes place in an orderly (pseudo-plane front) fashion.

REFERENCES

1. D. Apelian and G. Langford: Rapid Cycle Steel Casting, Proposal submitted to ARPA, January 24, 1977.

2. C. F. Dixon: Can. Met. Quart. (1973), 12, 309.

3. A. Lawley: Int. J. Powder Met. and Powder Tech. (1977), 13, 169.

4. S. N. Singh: Met. Trans. (1974), 5B, 2165.

5. G. Langford and R. E. Cunningham: Met. Trans. B (1977), 9B, 5.

6. J. F. Elliot, M. Gleiser, V. Ramakrishna: "Thermochemistry for Steelmaking" (1963) Addison-Wesley, U.S.A.

7. D. R. Gaskell: "Introduction to Metallurgical Thermodynamics", McGraw-Hill, New York (1973) 497.

8. S. Ban-ya, J. F. Elliot, J. Chapman: Met. Trans. (1970), 1, 1313.

9. W. Jost: "Diffusion in Solids, Liquids, Gases", Academic Press, New York (1960), p. 45.

FIGURES

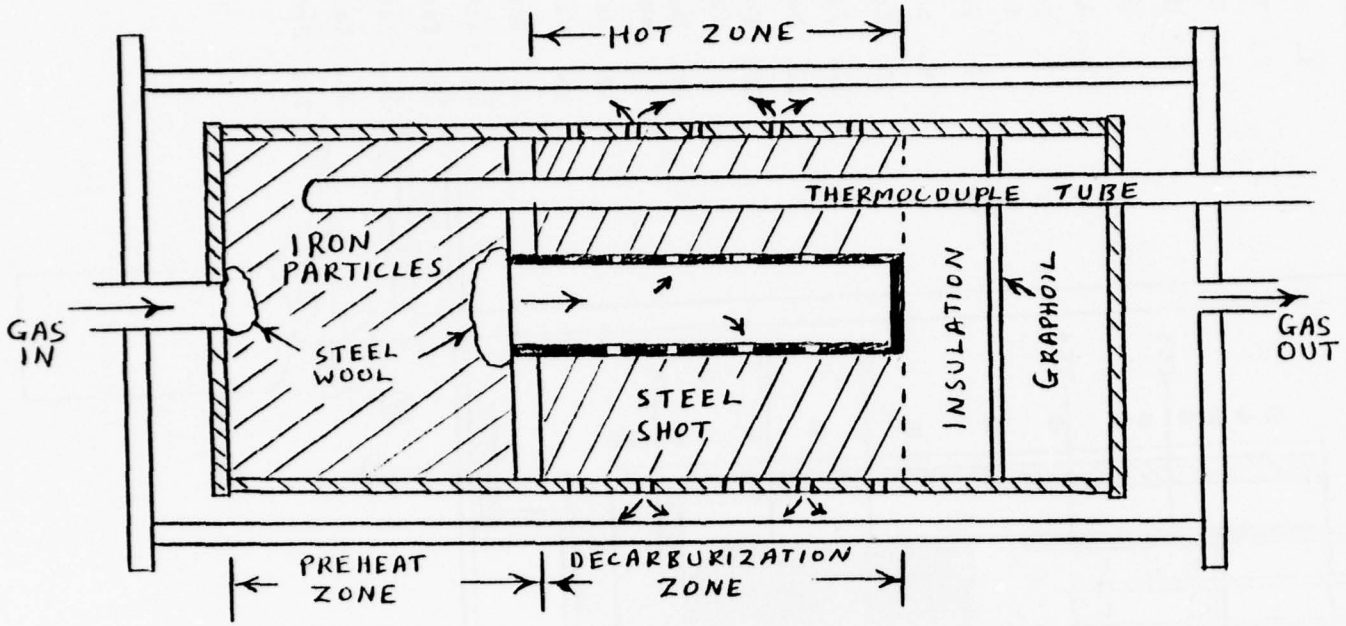

Figure 5. Schematic diagram of the decarburization furnace.

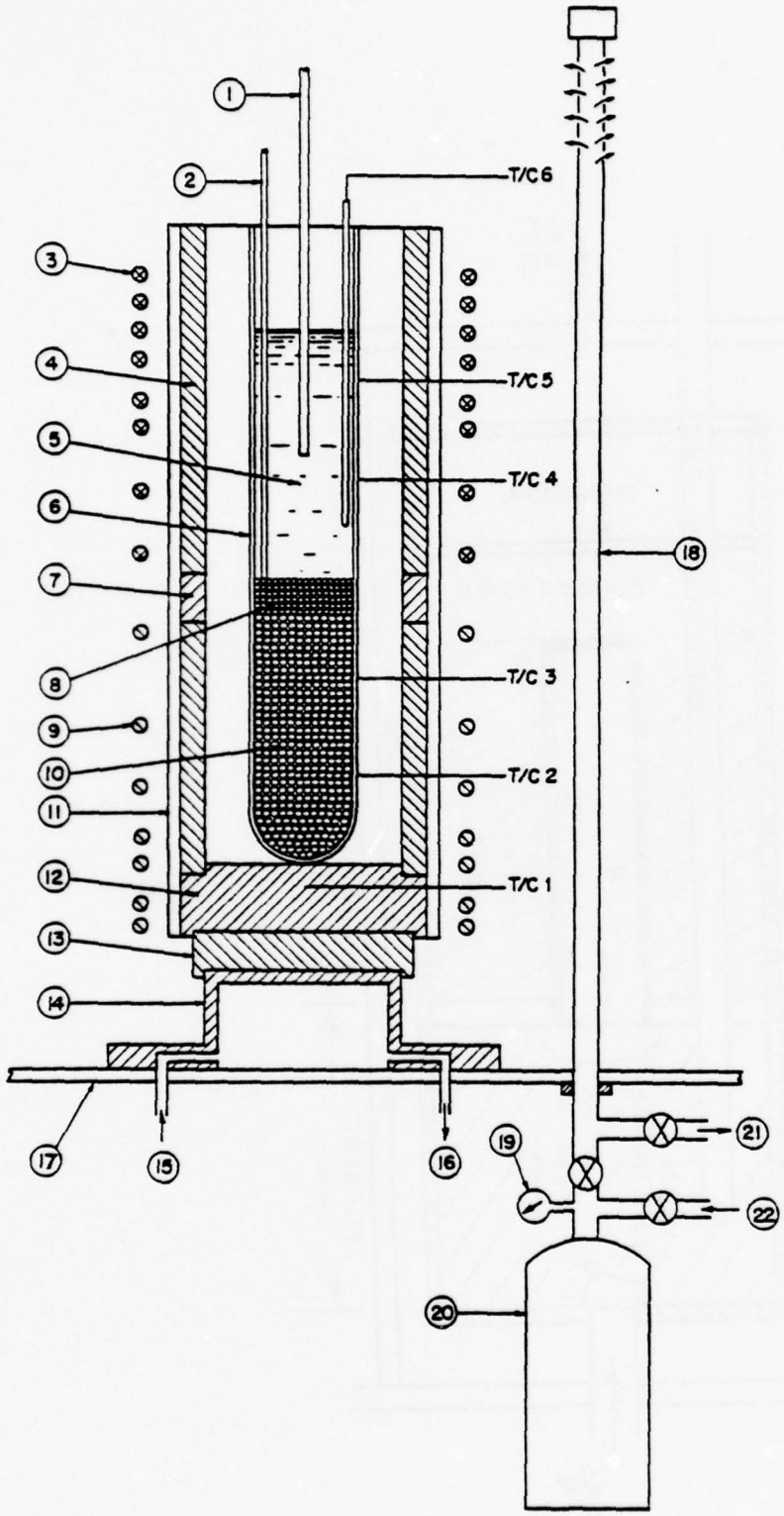

KEY to Figure 6:

1. Alumina bubble tube.
2. Thermocouple.
3. Upper induction coils.
4. Main Graphite Susceptor.
5. High carbon steel melt.
6. Alumina crucible.
7. Pyrolytic graphite insulator.
8. Particle valve.
9. Lower induction coils.
10. Low carbon steel shot.
11. Fiberfrax insulation.
12. Base graphite susceptor.
13. Pyrolytic graphite insulator.
14. Water-cooled pedestal base.
15. Water inlet.
16. Water outlet.
17. Dome base.
18. Stand pipe.
19. Pressure gauge.
20. Accumulator.
21. Vacuum line.
22. Pressure line.

Figure 6. Schematic diagram of the assembly in the dome of the diffusional solidification (SD) furnace.

T, °C	T, °K	K	P_{CO} (atm)
1450	1723	0.04234	0.36
1500	1773	0.16104	0.71
1550	1823	0.56924	1.33
1600	1873	1.88096	2.42
1650	1923	5.84077	4.27
1700	1973	17.12453	7.32

Activities are taken from Elliot et al[6], assuming 0.1 w/o Si, 0.05 w/o C, balance Fe and $a_{SiO_2} = 1$.

b) Alumina

$$Al_2O_{3(s)} = 2Al_{(\ell)} + \frac{3}{2} O_{2(g)} \quad \Delta G_6^\circ = 402{,}300 - 77.83\ T \tag{6}$$

$$3(C_{(s)} + \frac{1}{2} O_{2(g)} = CO_{(g)}) \quad 3\Delta G_7^\circ = 3(-26{,}760 - 20.98\ T) \tag{7}$$

$$Al_2O_{3(s)} + 3C_{(s)} = 2Al_{(\ell)} + 3CO_{(g)} \quad \Delta G_8^\circ = \Delta G_6^\circ + 3\Delta G_7^\circ = 322{,}020 - 140.77\ T \tag{8}$$

$$K = \exp\left(-\frac{\Delta G_8^\circ}{RT}\right)$$

$$= \exp\left(-\frac{322{,}020}{1.987\ T} + \frac{140.77\ T}{1.987\ T}\right)$$

$$= \exp\left(-\frac{162{,}047}{T} + 70.84\right)$$

Also, for reaction 8,

$$K = \frac{(a_{Al})^2 (P_{CO})^3}{(a_C)^3} = \frac{(19 \times 10^{-6})^2 (P_{CO})^3}{(2.5 \times 10^{-3})^3}$$

(Assume $a_{Al_2O_3} = 1$)

Therefore $$P_{CO}^3 = \frac{(2.5 \times 10^{-3})^3}{(19 \times 10^{-6})^2} \left[\exp\left(-\frac{162{,}047}{T} + 70.84\right)\right]$$

$$P_{CO} = \left[\frac{(2.5 \times 10^{-3})^3}{(19 \times 10^{-6})^2} \cdot (K)\right]^{1/3}$$

$$= 3.511\ \sqrt[3]{K}$$

T,°C	T,°K	Eq. Const., K	$K^{1/3}$	P_{CO}(atm)
1450	1723	8.32×10^{-11}	4.366×10^{-4}	1.53×10^{-3}
1500	1773	1.18×10^{-9}	1.057×10^{-3}	3.71×10^{-3}
1550	1823	1.44×10^{-8}	2.438×10^{-3}	8.56×10^{-3}
1600	1873	1.55×10^{-7}	5.376×10^{-3}	1.88×10^{-2}
1650	1923	1.47×10^{-6}	1.138×10^{-2}	4.00×10^{-2}
1700	1973	1.24×10^{-5}	2.319×10^{-2}	8.14×10^{-2}

These calculations assume 0.01 w/o Al, 0.05 w/o C, balance Fe and $a_{Al_2O_3} = 1$. Activities are taken from Elliot et al. [6].

These calculations indicate that SiO_2 and other oxides (MnO, FeO, etc.) of lesser stability are easily reduced by the carbon present in the melt; inert gas bubbling merely improves the kinetics of the process by eliminating the necessity of nucleating CO bubbles in the melt itself, which is not an easy process. More stable oxides such as the Al_2O_3 used as an example here require flushing of the melt with sufficient inert gas to maintain an open system; the inert gas must have an oxidizing potential less than the partial pressures of CO above an oxide-saturated melt.

As a practical matter, less stable oxides than Al_2O_3 are reduced by carbon with the inert gas bubbles acting as a kinetic aid; Al_2O_3 is removed mainly by precipitation followed by flotation, agglomeration, and (slow) reduction by dissolved carbon; the inert gas acts to stir the melt and provide an infinite sink for the CO generated. Bubbling rates of about 1 ℓ/min are currently being used; excessive bubbling is likely to lead to excessive disolution of the Al_2O_3 crucible and particle valve, especially at very high temperatures (1600°C and above for steels). This latter effect is troublesome during recharging of

the melt, during which temperatures of 1680°C are reached; the melt must subsequently be carefully cooled to 1500-1550°C to ensure that precipitation of dissolved Al_2O_3 is complete enough to minimize deposition of Al_2O_3 in the orifice during atomization.

APPENDIX IV-B: THERMODYNAMICS AND KINETICS OF DECARBURIZATION

a) Carbon Content

The decarburization reaction is

$$C_{(s)} + CO_{2(g)} = 2CO_{(g)} \qquad (1)$$

The free energy (ΔG_1°) for this reaction may be derived from the free energies of the following reactions (From Gaskell[7]).

$$C_{(s)} + \tfrac{1}{2} O_{2(g)} = CO_{(g)} \qquad \Delta G_2^\circ = -26,700 - 20.95\ T \qquad (2)$$

$$C_{(s)} + O_{2(g)} = CO_{2(g)} \qquad \Delta G_3^\circ = -94,200 - 0.2\ T \qquad (3)$$

$$\Delta G_1^\circ = 2\Delta G_2^\circ - \Delta G_3^\circ$$

$$= -53,400 - 41.90T + 94,200 + 0.2\ T$$

$$\underline{\Delta G_1^\circ = 40,800 - 41.70\ T.}$$

For a decarburization temperature of 1000°C (1273°K) the partition coefficient, K_p, is given by

$$K_p = \exp\left[-\frac{\Delta G^\circ}{RT}\right]$$

$$= \exp\left[\frac{-(40,800 - 41.70 \times 1273)}{1.987 \times 1273}\right]$$

$$\underline{K_p = 124.56}$$

Since, for reaction (1), $K_p = \dfrac{P_{CO}^2}{P_{CO_2}\, a_C}$

and

$$P_{CO} + P_{CO_2} = 1$$

$$K_p = \frac{(1 - P_{CO_2})^2}{P_{CO_2} a_C} = 124.56$$

Where a_C is the activity of carbon, in the γ-Fe field, and is given by (Ban-ya et al.[8]) as:

$$\log_e a_C = \frac{3770}{T} + 2.72 \log_e T - 10.525 + \frac{3860\ Y_C}{T} + \log_e\left(\frac{Y_C}{1-Y_C}\right) \qquad (4)$$

where Y_C is the atomic ratio of carbon to iron; $\frac{n_C}{n_{Fe}}$.

The P_{CO}/P_{CO_2} ratio at which oxidation of the iron will occur sets a lower limit on the carbon content that can be achieved by decarburization.

$$Fe_{(s)} + CO_{(g)} = FeO_{(s)} + CO_{(g)} \qquad \Delta G^\circ_5 = 5450 - 5.80\ T \qquad (5)$$

$$K_p = \frac{P_{CO}}{P_{CO_2} a_{Fe}} = \exp - \frac{(5450 - 5.80 \times 1273)}{1.987 \times 1273} = 2.13$$

The activity of iron in the austenite phase field is given by:

$$\log_e a^{\gamma}_{Fe} = - \frac{(1970)\ Y_C^2}{T} + \log_e(1 - Y_C) \qquad (6)$$

Using this equation it was found that the percentage of CO_2 in the gas should not exceed 32% to prevent oxidation of iron. Therefore, if we use 30% CO_2 in the gas mixture we can estimate the carbon content of the shot after decarburization. If the total gas pressure is 1 atmosphere and

P_{CO_2} = 0.3 atmospheres

P_{CO} = 1 - P_{CO_2} = 0.7 atmospheres.

For reaction (1), $K_p = \frac{P_{CO}^2}{P_{CO_2} a_C}$

$$a_C = \frac{P_{CO}^2}{P_{CO_2} \times K_p}$$

$$= \frac{0.7^2}{0.3 \times 124.54}$$

$$a_C = 0.01311$$

From equation (4)

$$\log_e 0.01311 = \frac{3770}{1273} + 2.72 \log_e 1273 - 10.525 + \frac{3860\ Y_C}{T} + \log_e \left(\frac{Y_C}{1-Y_C}\right)$$

$$-1.8824 = 2.9615 + 8.4451 - 10.525 + 3.0322\ Y_C + \log_e \left(\frac{Y_C}{1-Y_C}\right)$$

$$3.032\ Y_C + \log_e \left(\frac{Y_C}{1-Y_C}\right) = -2.764$$

Substituting values for Y_C of 0.0020 and 0.0015, the left hand side of this equation works out to be -2.692 and 2.817, respectively. Therefore, taking $Y_C = 0.002$,

$$0.002 = \frac{n_C}{n_{Fe}}$$

$$= \frac{n_C}{(1-n_C)}$$

$$n_C = 0.002\ (1-n_C)$$

$$n_C = 0.002 - 0.002\ n_C$$

$$n_C = \frac{0.002}{1.002} = 0.001996$$

Therefore, weight fraction $C = \frac{n_C \times 12}{(1-n_C)\ 55.85 + n_C \times 12}$

Therefore, carbon content attainable by this method of decarburizing is estimated to be 0.04295 wt. %.

b) Decarburization Time

Diffusion out of a sphere of radius r_o is given by the following equation (from Jost[9]):

$$\frac{\bar{C} - C_f}{C_i - C_f} = \frac{6}{\pi^2} \exp\left[-t\,\pi^2 \frac{D}{r_o^2}\right] \qquad (6)$$

$$0.5 = \frac{6}{\pi^2} \exp\left[-t\,\pi^2 \frac{D}{r_o^2}\right]$$

$$\exp\left[-t\,\pi^2 \frac{D}{r_o^2}\right] = \frac{1}{2} \times \frac{\pi^2}{6} = \frac{9.8696}{12} = 0.82247$$

$$-t\pi^2 \frac{D}{r_o^2} = \log_e 0.82247 = -0.19545$$

$$t = \frac{0.19545}{\pi^2 D} \times r_o^2$$

$$t = \frac{1.9803 \times 10^{-2}}{D}\ r_o^2 \text{ secs.}$$

Using different experimental data (from Elliot et al.[6]), values of the diffusion coefficient for C in γ-Fe near 1000°C lie in the range 2.24×10^{-7} to 3.11×10^{-7} $cm^2 sec^{-1}$. The decarburization times calculated from these values of D and various particle sizes are given in Table IV-BI.

TABLE IV-BI: Decarburization of Fe-C Shot at 1000°C; calculated range of times for decarburization.

r_o, cm	r_o^2, cm^2	t,* s	t',** s
1.0	1	8.84×10^{4}	6.37×10^{4}
0.1	0.01	8.84×10^{2}	6.37×10^{2}
0.05	0.0025	$2.21 \times 10^{+2}$	1.59×10^{2}
0.01	0.0001	8.84	6.37
0.005	0.000025	2.21	1.59
0.001	0.000001	8.84×10^{-2}	6.37×10^{-2}

* Value of diffusion coefficient used

$D = 2.24 \times 10^{-7}$ cm^2/s

** Value of diffusion coefficient used

$D = 3.11 \times 10^{-7}$ cm^2/s

V. WORK IN PROGRESS:

MOLD PERMEABILITY

INFILTRATION KINETICS

SD METALLURGY

SPECIFIC ALLOYS

H. Sreshta
M. Paliwal
D. Apelian
G. Langford

V. WORK IN PROGRESS

SUMMARY

Several tasks in progress are reported in this section. They include evaluating investment molds, relating the infiltration variables to each other, understanding the physical metallurgy of the SD cast product and advantageously applying this unique metallurgy to other specific alloys.

We are investigating the feasibility of using investment molds as non-permanent molds for the SD casting process. Investment mold technology is already well established and offers the advantages of high productivity and low cost. The critical requirement is that the mold be permeable to the deoxidation products and that it also be impermeable to the high pressure gas used in forced infiltration. Fifty-five conventional and glazed investment molds have been prepared and will be tested shortly in the SD casting furnace.

We are modelling the kinetics of infiltration of liquid iron through the packed bed of low carbon steel shot, so as to obtain the governing equation. We are building apparatus to measure the movement of the liquid front within the low carbon porous medium by monitoring the voltage drop across the latter as a function of time. An understanding of the process control variables for infiltration is required for a rational design of a rapid cycle casting machine.

Mechanical property evaluations for differently solidified SD castings are underway. We are investigating the effects of infiltration pressure, alloying elements and the role of impurities in the shot.

We are studying two other specific alloy systems besides plain carbon steels. Ultra-high carbon high speed steel cutting tools cast to net shape and heat treated from much lower than normal temperatures offer substantial critical material and energy savings, and aluminum-lithium alloy castings with high lithium content may enable improved stiffness in structural components due to the higher elastic moduli of such alloys and integrated, material-saving casting design.

TABLE OF CONTENTS: SECTION V. WORK IN PROGRESS

V.A Introduction 184

V.B Use of Investment Molds for SD Process 186

1. Introduction 187
2. Investment Shells for Experimental Study..... 187
3. Theoretical Considerations for Using Permeable Molds for SD Process..... 187
4. Theoretical Considerations for Using a Permeable Mold Coated with a Glaze 190
5. Experimental Evaluation of Permeable Molds 191

Table 194

Appendix VB-I: Estimation of the Amount of Gas Entering a Permeable Mold and Estimation of the Glaze Penetration Distance for a Specific SD Casting 196

References for Section V.B and Appendix VB-I 199

V.C Experimental Verification of the Infiltration Equation (Mass, Momentum and Heat Transfer During Infiltration).. 200

V.D Control of Properties Through SD Casting Practice and Alloy Composition 209

1. Introduction 210
2. Effect of Infiltration Pressure 211
3. Study of Fracture Surfaces 212
4. Effects of Alloying Elements 212
5. Large Size Casting 214

References 214

V.E Application of SD Casting to Specific Alloys 215

References 217

V.A INTRODUCTION

In addition to the more-or-less complete tasks reported above, several other tasks* are incomplete but sufficiently developed to be reported now. These tasks include:

- Application and development of the technology for nonpermanent, investment-type molds for the SD process.
- Verification and study of the mechanics and kinetics of infiltration of high carbon melt into low carbon preheated shot.
- Development of the metallurgical practices which best take advantage of the SD casting process.
- Application of the SD process to specific alloy types.

Several other tasks have not yet been begun; these include:

- Measurement of the tensile properties of partially frozen SD castings.
- Establishing the specifications and method of manufacture of permanent molds, and vacuum bonded molds.

The high temperature tensile tests to be done on SD castings at the moment of infiltration require a well-developed SD casting technology, especially with respect to the mold material. This technology is now sufficiently well developed that design and construction of the necessary apparatus during the second contract year is practical. A complementary proposal for fundamental research on SD iron based alloys[2] has been prepared by one of us (GL). The high-temperature casting/testing apparatus is essential to that work, which

---

* listed in the Statement of Work to be Done in the original proposal[1] (reproduced in the Introduction to this report, page 2)

proposes to use partially solidified SD castings as models of the structure of solid-liquid mixtures for basic studies of their mechanical properties.

Similarly, we will now begin the study of the manufacture and suitability of permanent SD casting molds so that we will have sufficient engineering and economic information to consider seriously a "die casting" machine for SD casting during the third contract year.

References

1. D. Apelian and G. Langford: Rapid Cycle Steel Casting. Proposal for Research Written for the Advanced Research Projects Agency, 1977.

2. G. Langford: Diffusion Solidification Iron Based Alloys. Proposal for Research Written for the Army Research Office, 1977.

V.B. USE OF INVESTMENT MOLDS FOR SD PROCESS

H. Sreshta
G. Langford
D. Apelian

V.B. Use of Investment Molds for SD Process

1. Introduction

The investment mold (lost wax pattern) manufacturing process has been described in the original proposal.[1] Investment molds fall under the category of permeable molds. The critical experiments to be done for adapting permeable molds to the SD casting process are discussed in Ref. (1).

2. Investment Shells for Experimental Study

A number of investment shells have been made* using the procedure outlined in Ref. (2). The prime coat and backup coat slurries were similar to those recommended in (2). The prime stucco coat was 75μm zircon (zirconium silicate) sand. The backup stucco was 850μm to 300μm alumina-silicate sand. In some cases, <45μm alumina powder was used as the stuccoing grain with the aim of reducing the mold permeability to gas. The coating schedule for different shells made is listed in Table V.BI. Except in shells 1 and 3 all were able to withstand an external pressure of 100 psig (790 kPa) during the dewaxing operation. The function of the backup coat is to strengthen the shell. Since only one backup coat was given to shells 1 and 3; those molds did not have sufficient strength to withstand external pressure during the dewaxing operation. The molds were not fired as in the conventional process. The mold will be fired during the heating of the SD components to casting temperatures.

3. Theoretical Considerations for Using Permeable Molds for SD Process

The SD casting process for steels[3] involves the infiltration of liquid cast iron past low carbon steel powder (porous solid) at casting temperatures. The application of pressure results in the flow of liquid cast

* We wish to thank Mr. T. Micola, President of Delvest, Inc., for permitting us to use the raw materials and equipment for making the molds.

iron into the porous solid and also flow of the pressurization gas into the porous solid through the permeable mold. The following assumptions are made in this analysis:

- The furnace chamber is evacuated prior to infiltration.
- The amount of gas entering the mold is small, i.e., the driving force for fluid flow is not affected by back pressure in the porous solid.
- The liquid metal wets the porous solid iron.

Using the first and second assumptions, the pressure driving force for gas and liquid flow is given by Eq. [1]*

$$\Delta P_G = \Delta P_L = P_A \qquad [1]$$

The infiltration kinetics for liquid cast iron through a packed bed of spherical low carbon iron particles has been analyzed by Langford and Cunningham[3] and can be expressed by Eqs. [2] and [3].

$$v = \frac{1}{(60 \times \rho \times \varepsilon^2)^{1/2}} \times \left(\frac{\Delta P_L \, dp}{\ell}\right)^{1/2} = C_1 \left(\frac{P_A dp}{\ell}\right)^{1/2} \qquad [2]$$

$$t = \frac{2}{3} \times \frac{1}{C_1} \left(\frac{\ell^3}{dpP_A}\right)^{1/2} \qquad [3]$$

The flow of gas entering the porous solid through the mold wall obeys D'Arcy's law[4] and is given by Eq. [4]

$$\frac{dQ}{dt} = KA \left(\frac{\Delta P_G}{t_H}\right) = KA \, \frac{P_A}{t_H} \qquad [4]$$

The available area for gas flow decreases with time, as the liquid filled region of the porous solid can be considered impermeable to gas flow. Considering a

* A list of notations is given at the end of this section of the report.

cylindrical casting, the available area at any time during the infiltration is given by Eq. [5]

$$A = 2\pi R[L - \ell] \qquad [5]$$

Combining Eqs. [3] and [5] the available area can be expressed as a function of time

$$A = 2\pi R \left[L - \left(\frac{9}{4} C_1^2 t^2 dp P_A\right)^{1/3}\right] \qquad [6]$$

Combining Eqs. [4] and [6] and integrating Eq. [4] between the limits:

$t = 0, \quad L = 0, \quad Q = 0$

$t = t_I, \quad L = L, \quad Q = Q,$

the amount of pressurization gas entering the mold can be determined

$$Q = \frac{KP_A 2\pi R}{t_H} \left(L - \frac{3}{5}\left(\frac{9}{4} G^2 \, dp \, P_A\right)^{1/3} t_I^{2/3}\right) \qquad [7]$$

Substituting for t_I in Eq. [7] using Eq. [3] gives Eq. [8]

$$Q = \frac{8\pi KR}{15 C_1 t_H} \left(\frac{L^5 P_A}{dp}\right)^{1/2} \qquad [8]$$

The volume of gas entering the mold during infiltration can be estimated using Eq. [8]. Appendix V-B.I gives the quantitative analysis for a specific SD casting. We find that the amount of gas entering a conventional investment mold is 2.9 times the mold volume. The result violates the second assumption above and hence the gas pressure will build up in the mold, preventing the porous solid from being infiltrated with liquid.

The volume of gas entering the mold can be reduced to 5 percent of the casting volume if the mold permeability to gas is decreased by a factor of 170 (Appendix V-B.I). By using <45μm alumina powder for stuccoing some of the investment molds we may have been successful in decreasing the conventional mold permeability by a factor of 10 to 15. To decrease the mold permeability by a

factor of 170 will require the stuccoing grain size to be 0.75μm or 1/100 times the grain size used for manufacturing conventional molds.

The most effective way for reducing the amount of gas entering the mold is to decrease the casting height without changing the infiltration pressure. Reducing the casting height from 100mm to 20mm decreases the quantity of gas entering the mold by a factor of 170 (Appendix V-B.I); alternatively, the bottom half of a cylindrical mold could be made impermeable as discussed in the next section.

4. Theoretical Considerations of Using a Permeable Mold Coated with a Glaze

The glaze is applied to the mold in powdered form either by dipping the mold in a glaze powder suspension or by using spraying techniques. Coating the entire permeable mold with a glaze may restrict the passage of gases formed in the porous solid due to deoxidation after the cast iron charge has melted. It is desirable to coat the mold only up to the center of the particle valve thereby leaving a small passage for the gases evolved in the porous solid to escape.

At casting temperatures, the glaze will form a viscous layer around the mold making it impermeable to the pressurization gas. The gas can enter the mold only through the unglazed region between the cast iron and particle valve. However, the viscous glaze layer under the influence of the external gas pressure may penetrate the mold and enter the iron shot, an undesirable situation from the viewpoint of product quality.

The rate of glaze penetration into the mold is governed by Hagen-Poiseuille's Equation [4][4]

$$\frac{dx}{dt} = v = C\frac{\Delta P}{\mu X} = \frac{CP_A}{\mu X} \qquad [9]$$

The penetration distance (distance moved by glaze into mold) can be found by

integrating Eq. [9] between the limits:

$$t = 0, \quad X = 0$$

$$t = t_I, \quad X = \ell'$$

$$\ell' = \frac{2C\ P_A\ t_I}{\mu X} \qquad [10]$$

Substituting for t_I in Eq. [10] using Eq. [3], the penetration distance is given by Eq. [11]

$$\ell' = \left(\frac{4C}{3C_1\mu}\right)^{1/2} \left(\frac{L^3 P_A}{dp}\right)^{1/4} \qquad [11]$$

The penetration distance can be determined using Eq. [11]. A quantitative estimation for a specific example is given in Appendix V-B.I. The glaze penetration distance is very small during the infiltration period and the quantity of gas entering the mold is only 0.16 percent of the casting volume. Therefore, the glaze serves as an effective method for eliminating the gas-liquid race problems encountered while using permeable molds for manufacturing SD castings.

5. Experimental Evaluation of Permeable Molds

Each experimental run will involve making three SD castings using the following molds:

(1) investment mold as made by the coating schedule given in Table V-B.I

(2) investment mold coated with a glaze

(3) impermeable mullite mold.

The macroporosity resulting from the pressurization gas will be estimated as a function of the casting length by:

(a) measuring the casting density at different locations

(b) using metallography techniques

(c) evaluating the mechanical properties of the casting.

The permeability of the fired investment molds will be measured using a technique similar to that used by Rusher[5] for evaluating air-mold permeability of conventional investment molds. The glaze viscosity at casting temperature will be measured using a Brookfield viscometer.[6]

After evaluating the above properties of the casting molds and glazes, the criteria for adapting permeable molds to the SD process will be established.

Notations Used:

ΔP_G	pressure driving force for gas flow
ΔP_L	pressure driving force for liquid flow
P_A	infiltration pressure
v	velocity of liquid front
ρ	density of liquid
ε	void fraction of porous solid
dp	particle diameter of porous solid
ℓ	distance moved by the liquid front in a time, t
t_I	infiltration time for a casting of length, L
dQ/dt	volumetric flow rate of gas
A	area available for gas flow
K	gas mold permeability
t_H	thickness of mold
R	radius of mold
C	Hagen-Poiseville's equation constant
μ	viscosity
ℓ'	glaze penetration into mold during the infiltration time, t_I
V_c	casting volume
Q	quantity of pressurization gas entering the mold during infiltration

Table V-B.I Coating Schedule for Investment Shells

Shell Number	Coating Schedule
1, 3	C1S1, C1S1, C1S1, C2S2, C2
4, 5, 6	C1S1, C1S1, C1S1, C2S2, C2S1, C1
7, 8, 9	C1S1, C1S1, C1S1, C2S2, C1S2, C1S2, C1
10, 11, 12	C1S1, C1S1, C1S1, C2S2, C1S1, C1
13, 15	C1S1, C1S1, C2S2, C1S2, C1S2, C1S2, C1
16, 17, 18	C1S1, C1S1, C2S2, C2S2, C1S1, C1S2, C1
19, 20, 21	C1S1, C1S1, C1S1, C2S2, C1S1, C1S2, C1S2, C1
22, 24	C1S1, C1S1, C1S2, C1S2, C1S2, C2S2, C2S2, C1
25	C1S1, C1S1, C2S2, C1S1, C1S1, C2S2, C1S2, C1
26, 27, 28	C1S1, C1S1, C2S2, C2S2, C2S2, C2
29, 30, 31	C1S1, C1S1, C1S1, C2S2, C2S2, C2S2, C2
32, 33, 34	C1S1, C1S1, C2S2, C1S1, C2S2, C1S1, C2S2, C2
35, 36, 37	C1S1, C1S1, C1S3, C2S3, C2S2, C2S2, C2S2, C2
38, 39, 40	C1S1, C1S1, C2S3, C2S3, C2S3, C2S3, C2S2, C2S2, C2
41, 42, 43	C1S1, C1S1, C1S3, C1S3, C1S3, C2S2, C2S2, C2S2, C2
44, 45, 46	C1S1, C1S3, C1S3, C2S1, C2S1, C2S2, C2S2, C2
47, 48, 49	C1S1, C1S3, C1S3, C2S3, C2S3, C2S1, C2S2, C2
50, 51, 52	C1S1, C1S3, C2S3, C2S1, C2S2, C2S2, C2S2, C2
53, 54, 55	C1S1, C1S3, C2S3, C2S1, C2S2, C2S1, C2S2, C2

Notations Used in Coating Schedule

C1. Primary slurry coat

C2. Backup slurry coat

S1. Stucco coat with 75μm zircon sand

S2. Stucco coat with 850μm to 300μm alumino-silicate sand

S3. Stucco coat with <45μm mesh alumina powder

APPENDIX V-B.I: ESTIMATION OF THE AMOUNT OF GAS ENTERING A PERMEABLE MOLD AND ESTIMATION OF THE GLAZE PENETRATION DISTANCE FOR A SPECIFIC SD CASTING

Process Parameters

- Casting Size

  Diameter = 50 mm

  Length, L = 100 mm

- Infiltration Gas

  Nitrogen

  Pressure, P_A = 790 kPa (100 psig)

- Mold

  Thickness, t_H = 4 mm

  Radius, R = 29 mm

  Mold Permeability, $K = 20 \times 10^{-10}\ m^2 \cdot (Pa \cdot S)^{-1}$

The value of mold permeability was chosen from the air-mold permeability range for conventional investment molds estimated by Rusher.[5]

Hagen-Poiseville's equation constant C is estimated by comparing Hagen-Poiseville's and D'Arcy's equations. The constant C is given by the relationship:

$$C = K\mu$$

$$\mu_{Air} = 1.8 \times 10^{-5}\ Pa \cdot S \text{ (at room temperature)}$$

$$\therefore\ C = 3.6 \times 10^{-14} m^2$$

· Glaze

The viscosity of the glaze at casting temperatures is a function of the glaze composition. Glaze viscosities are expected to be in the range of 10 to 40 Pa·S at SD casting temperatures.[7]

· Shot

Diameter, dp = 1 mm

Volume of Gas Entering a Conventional Investment Mold for the Casting Parameters Cited Above

$$Q = \frac{8}{15} \frac{\pi K R}{C_1 t_H} \left(\frac{L^5 P_A}{dp}\right)^{1/2}$$

$$C_1 = (60\ \rho \varepsilon^2)^{-1/2}$$

$$= (60 \times 7.87 \times 10^3 \times 0.38^2)^{-1/2} = .0038\ (m^3/kg)^{1/2}$$

$$Q = \frac{8}{15} \times \frac{\pi \times 20 \times 10^{-10} \times 0.029}{.0038 \times .004} \left(\frac{0.1^5 \times 7.9 \times 10^5}{.001}\right)^{1/2}$$

$$= 5.68 \times 10^{-4} m^3$$

$$V_C = \frac{\pi}{4} (0.05)^2 (0.01) = 1.96 \times 10^{-4} m^3$$

$$\frac{Q}{V_C} = 2.89$$

Desired Mold Permeability for Reducing the Amount of Gas Entering the Mold to Five Percent of the Casting Volume - The Process Conditions are Same as Above

$$Q = 0.5\ V_C$$

$$K = 20 \times 10^{-10} \times \frac{0.05 \times V_C}{2.89 \times V_C}$$

$$= 3.46 \times 10^{-11}\ m^2\ (Pa \cdot S)^{-1}$$

The permeability of mold should be reduced by a factor of 170 to restrict the amount of gas entering the mold to 5 percent of the casting volume.

Maximum Casting Height Using Conventional Molds for Reducing the Amount of Gas to Five Percent of the Casting Volume - The Process Conditions are Same as Above

$$L = 0.10 \times \left(\frac{V_C \times 0.05}{V_C \times 2.98}\right)^{2/5} = 19.5 \text{ mm}$$

Penetration of Glaze into Mold Wall

$$\ell' = \left(\frac{4C}{3C_1\mu}\right)^{1/2} \left(\frac{L^3 P_A}{dp}\right)^{1/4}$$

$$= \left(\frac{4 \times 3.6 \times 10^{-14}}{3 \times .0038 \times 10}\right)^{1/2} \left(\frac{0.1^3 \times 7.9 \times 10^5}{.001}\right)$$

$$= 0.034 \text{ mm}$$

Quantity of Gas Entering the Porous Solid When the Mold is Coated with a Glaze

If we assume that the particle value height is 10 mm for manufacturing the SD casting, then the effective casting length exposed to the pressurization gas during infiltration is 5 mm

$$\therefore L = 5 \text{ mm}$$

Again, for the same process conditions except that L = 5 mm, the quantity of gas entering the mold can be determined using Eq. [8] of the text (Section V.B)

$$Q = 2.89\ V_C \left(\frac{5}{100}\right)^{5/2} = 1.6 \times 10^{-3}\ V_C$$

$$\frac{Q}{V_C} = 0.16 \text{ percent.}$$

References for Section V.B and Appendix V-B.I

1. D. Apelian and G. Langford: Rapid Cycle Casting of Steels. Proposal for Research Written for the Advanced Research Projects Agency, 1977.

2. "Ceramic Shell Investment Casting with DuPont Ludox", E. I. duPont de Nemours & Co., Wilmington, DE.

3. G. Langford and R. Cunningham: Met. Trans. B, 1978, Volume 9B, pp. 5-19.

4. P. C. Carman: Transactions - Inst. of Chem. Engg., Volume 15, 1937, p. 150.

5. R. L. Rusher: Foundry, July 1972.

6. "Brookfield Syncho-Lectric Viscometer Instruction Manual", Brookfield Engineering Laboratories, Stoughton, Mass.

7. C. W. Parmelee: Ceramic Glazes, J. J. Svec. ed., Cahners Publishing Company, 1973, pp. 183-184.

V.C EXPERIMENTAL VERIFICATION OF THE INFILTRATION EQUATION (MASS,MOMENTUM, AND HEAT TRANSFER DURING INFILTRATION)

H. Sreshta
G. Langford
D. Apelian

V.C: MECHANICS OF FORCED INFILTRATION OF HIGH CARBON LIQUID INTO A LOW CARBON POROUS SOLID

1. Introduction

The SD casting process[1] involves the infiltration of iron-saturated liquid past low carbon steel particles contained in a packed bed. This is a complex phenomenon characterized by simultaneous mass, momentum and heat transfer. It is necessary to have a quantitative understanding of the infiltration process so that we can predict the infiltration kinetics for SD castings under practical conditions.

2. Existing Equations

Langford and Cunningham[1] have developed the infiltration kinetics for the SD process by considering the mass transfer and fluid flow aspects individually and then combining the two phenomena by using a linear constraint to avoid macrosegregation. The infiltration pressure for the Langford-Cunningham (LC) analysis is given by Eq. [1]*

$$P = P_{\ell} + P_{\gamma} = 25 \times 10^{6}\ \rho k^{4} \varepsilon^{2}\ \left(\frac{D}{\alpha}\right)^{2}\ \frac{L^{3}}{d^{5}} + 20\ \frac{\gamma}{d} \qquad [1]$$

The Burke-Plummer (BP) equation for turbulent flow in porous media[2] could also be used to describe the infiltration mechanics of the SD process. Using the same approach as Langford and Cunningham for combining fluid flow and mass transfer aspects, the infiltration pressure is given by Eq. [2]

$$P = 1.2 \times 10^{6}\ \left[\rho k^{4}\ \frac{(1-\varepsilon)}{\varepsilon^{3}}\right]\ \left(\frac{D}{\alpha}\right)^{2}\ \frac{L^{5}}{d^{5}} + \frac{20\gamma}{d} \qquad [2]$$

---

* The notations used are given at the end of this section of the report.

a. Comparison Between LC and BP Equations

- The BP equation is based on the superficial velocity whereas the LC equation is based on the interstitial velocity.

- The pressure drop is evaluated using the hydraulic mean radius in the BP equation. The LC equation calculates the pressure drop based on the orifice area.

- The friction factor for the BP equation has been evaluated from experimental data. The LC equation estimates the friction factor from first principles.

- The infiltration pressure as a function of the SD casting variables (d, ℓ, k, D and α) is the same for both equations.

b. Limitations

- The velocity given by both equations approaches infinity when ℓ equals 0.

- Both equations are valid for turbulent flow, i.e. $Re = \frac{d\rho V_o}{\mu(1-\epsilon)} > 1000$ [2]. However, at infiltration pressures of 100 psig (790 kPa) and a shot size of 0.125 mm, the flow is in the turbulent regime for penetration distances given by Eq. [3]

$$\begin{aligned} &\text{LC:} \quad \ell \leq 9.2 \text{ mm} \\ &\text{BP:} \quad \ell \leq 28 \text{ mm} \end{aligned} \qquad [3]$$

At greater distances than that specified by Eq. [3], the flow is in the intermittent region (the laminar-turbulent transition region) and viscous effects must also be considered. To avoid

the mathematical effects of fluid flow behavior during infiltration it is desirable to use the Ergun's equation which is valid for all flow regimes.[2] Using the Ergun's equation, the infiltration time must be estimated by numerical techniques.

- The infiltration kinetics developed by Langford and Cunningham for the SD process neglect the thermal and mechanical effects resulting from solidification occurring during infiltration.

3. Theoretical Consideration of Infiltration During the SD Process

Since mass, momentum and heat transfer occur simultaneously during infiltration, the penetration distance is a function of the variables given in Eq. [4]

$$\ell = f_n (d_{PB}, d, D, k, \rho, \rho_s, \mu, \epsilon, M, V, P, \gamma, K, C_p) \qquad [4]$$

Most of the variables given in Eq. [4] are time dependent. If the variables do not change significantly with time, then an empirical relation for the infiltration distance as a function of dimensionless groups formed by combining the variables can be developed.

From the process development viewpoint, it is desirable to know the infiltration time, t_p, as a function of the following system variables:

- diameter of packed bed, d_{PB}
- diameter of shot, d
- casting temperature, T_C
- applied pressure, P
- casting height, L

The infiltration time as a function of the system variables is given by Eq. [5]

$$tp = k_o P_A^{\ a} d_{PB}^{\ b} d^c T_C^{\ d} L^e \qquad [5]$$

where, k_o, a, b, c, d, and e are constants. To evaluate the above constants in Eq. [5] it is essential to measure the infiltration distance as a function of time for different applied pressures, packed bed diameters, shot diameters and casting temperatures. If the critical time to avoid macrosegregation is determined experimentally, then Eq. [5] can be used to determine the infiltration pressure for a given casting length.

4. Experimental Setup

The experimental setup is shown in Fig. V-C1. The liquid front movement is measured in terms of the voltage drop across the porous low carbon steel solid as a function of time. The voltage drop across the porous solid is recorded by a visicorder.* A thermocouple is placed at the bottom of the packed bed to indicate the time taken by the liquid front to penetrate a packed bed length, L. The movement of the liquid front in terms of the measured voltage is derived in Appendix V-CI.

5. Experiments to be Done

- establishment of an empirical SD infiltration equation for monodisperse shot sizes for comparison with various theories and for practical applications.
- investigation of less ideal infiltration systems, that is, when substantial freezing accompanies infiltration as a result of thermal, mechanical, or shot-size distribution effects.
- comparison of SD infiltration kinetics to the infiltration kinetics of non-interactive (inert) packed bed in order to establish the applicable fluid flow equation.

* Honeywell, model number 906-C.

LEGEND

1. Electrical contact in melt
2. Melt
3. Particle Valve
4. Shot
5. Crucible
6. Steel Wool
7. Alumina powder (<45μm)
8. Standard resistance
9. Constant voltage cell
10. Visicorder
11. Recorder
12. Thermocouple
13. Electrical contact with packed bed

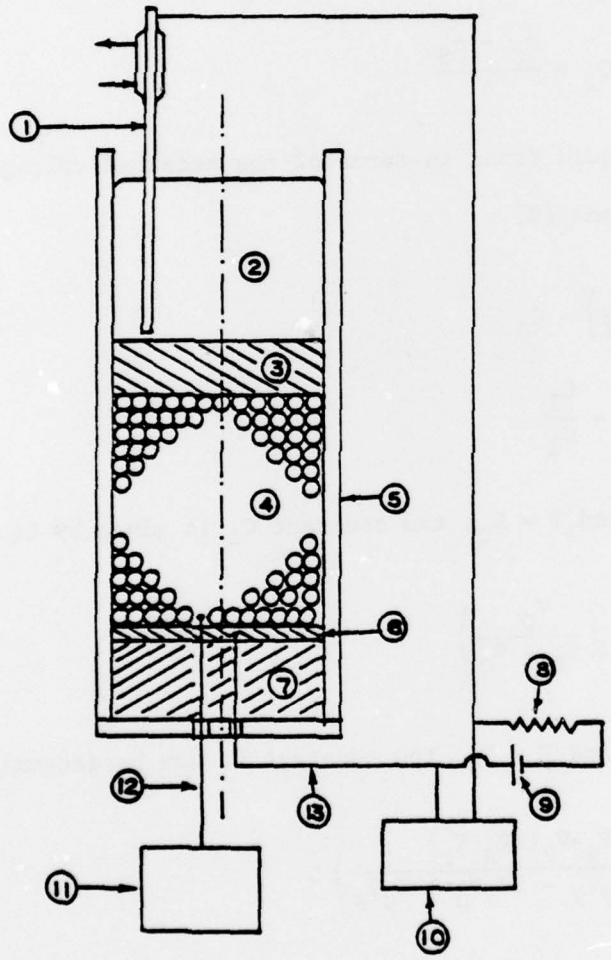

Figure V-C1. Apparatus for measuring the liquid front movement in an interacting porous medium.

APPENDIX V-C.I CORRELATION BETWEEN LIQUID FRONT MOVEMENT AND MEASURED VOLTAGE

The measured voltage across the packed bed is given by Eq. [1]

$$V = \left(\frac{V_S}{R_S + R}\right) R \qquad [1]$$

The resistance of porous solid, R, during infiltration is given by Eq. [2]

$$R = C_1 + C_2 \ell \qquad [2]$$

where, $C_1 = \frac{\rho_S L}{A}$ and $C_2 = \frac{\rho_C - \rho_S}{A}$

The movement of the liquid front in terms of the measured voltage is obtained by combining Eqs. [1] and [2].

$$\ell = C_3\left(\frac{V}{V_S - V}\right) - C_4 \qquad [3]$$

where, $C_3 = \frac{R_S}{C_2}$ and $C_4 = \frac{C_1}{C_2}$

At time, $t = 0$, $\ell = 0$ and $V = V_0$, the constant C_4 is given by Eq. [4]

$$\therefore \quad C_4 = C_3\left(\frac{V_0}{V_S - V_0}\right) \qquad [4]$$

At time, $t = t_p$, $\ell = L$ and $V = V_P$, the constant C_3 can be determined

$$\therefore \quad C_3 = \left(\frac{(V_S - V_P)(V_S - V_0)}{V_P V_S - 2V_P V_0 + V_0 V_S}\right) L \qquad [5]$$

Combining Eqs. [3], [4] and [5], the infiltration length as a function of the measured voltage is given by Eq. [6]

$$\frac{\ell}{L} = \left[\frac{(V_S - V_P)(V_S - V_0)}{V_P V_S - 2V_P V_0 + V_0 V_S}\right] \cdot \left(\frac{V}{V_S - V}\right) - \frac{V_0(V_S - V_P)}{V_P V_S - 2V_P V_0 + V_0 V_S} \qquad [6]$$

Notations Used

P	applied pressure
P_γ	pressure to overcome surface tension forces
P_ℓ	pressure for fluid flow through porous solid
ρ	density of fluid (melt)
k	distribution coefficient
ϵ	void fraction of porous solid
α	constant
D	diffusivity of carbon in austenite
L	casting height
d	shot diameter
γ	surface tension of liquid
ℓ	distance moved by the liquid front in the porous solid
d_{PB}	diameter of casting
ρ_S	density of solid
μ	viscosity of liquid
Re	Reynolds number
M	surface roughness factor for particles
U	velocity of liquid front
K	thermal conductivity of infiltrated solid
C_p	heat capacity of infiltrated solid
V	voltage drop across porous solid during infiltration
R_S	resistance of external resistor
V_S	DC source voltage
ρ_S	resistivity of porous solid
ρ_C	resistivity of porous solid infiltrated with liquid
t_p	time to infiltrate a casting height, L
V_O	voltage drop across porous solid when the liquid front makes contact with the porous solid.

REFERENCES FOR TEXT AND APPENDIX TO SECTION V-C

1. G. Langford and R. Cunningham: Met. Trans. B, 1978, Volume 9B, pp. 5-19.

2. R. B. Bird, W. E. Stewart and E. N. Lightfoot: Transport Phenomena, John Wiley and Sons, Inc., 1960, pp. 196-200.

V.D. CONTROL OF PROPERTIES THROUGH SD

CASTING PRACTICE AND ALLOY COMPOSITION

M. Paliwal
D. Apelian
G. Langford

V.D. Control of Properties Through SD Casting Practice and Alloy Composition

1. Introduction

Some mechanical properties of steels, such as reduction-of-area ductility, are controlled by preexisting pores or weak interfaces with second-phase particles whereas others, such as yield strength or temper embrittlement, are controlled by alloying and residual impurities. Cast, wrought, powder-metallurgy, welded, etc., steels are all processed differently to develop their unique characteristic properties.

We therefore intend to develop processing and compositional practices which will optimize the properties of SD castings. Specific features of SD casting which will be emphasized are:

- The ability to juxtapose shot and melt of different compositions and to put different shot alloys in different parts of the casting.
- The ability to control shrinkage cavitation (microporosity) by control of shot and melt quality.
- The ability to start with at least 62% solid pre-frozen at a high cooling rate.
- The inevitability of microsegregation of individual substitutional alloying elements.
- The ability to choose between individual or common melts.

Langford and Cunningham[1] have studied the grosser effects of processing parameters such as infiltration pressure, casting temperature (and temperature differences between shot and melt), oxygen content, and deoxidation practice (especially solid state vacuum carbon deoxidation (SSVCD) of cheap and/or internally oxidized shot). These variables and others warrant further study

as our knowledge of SD casting increases.

2. Effect of Infiltration Pressure

The infiltration pressure affects not only carbon macrosegregation but also the resulting porosity and, hence, the resulting mechanical properties such as yield strength and ductility. In these experiments the minimum infiltration pressure required for a given size particle will first be found and then the effect of using higher infiltration pressures on the resulting mechanical properties and porosities will be studied. The porosity in an SD casting is due to:

- Evolution of gases when the melt solidifies.
- Shrinkage cavity formed because of solidifying melt trapped in the closed interstices between solid particles.
- Trapped gases in the pore interstices.

Porosity caused due to evolution of gases when the melt solidifies can be reduced by

Starting with melt and shot low in O, or high in C content.

Use of high infiltration pressures.

Killing the melt with Al or Si.

The size of the shrinkage cavity formed due to solidifying melt can simply be reduced by use of smaller size particles (thus smaller pore sizes) however this will required higher infiltration pressures. Alternatively and importantly, this mode of cavitation can also be controlled by eliminating the nucleation sites for cavitation (oxide inclusions) by reducing the total oxygen content of the casting (see Langford and Cunningham[1]).

Trapped gases in the pore interstices are important. If a mold impermeable to gases is used for casting, it is necessary that the mold be evacuated prior to infiltration; otherwise the movement of the liquid front will be stopped when the back pressure of the trapped gases equals the applied infiltration pressure. Even if heating is done after evacuation of mold there will be entrapped gases if SSVCD is used as a method of reducing the oxides on the shot. Hence, porosity due to entrapped gases will influence major design considerations like mold permeability, use of SSVCD, and allowable gas pressure in the mold prior to infiltration.

3. Study of Fracture Surfaces

In an SD casting fracture can originate at one of the following sites:

- At second phase particles such as oxides inside the original shot or melt.
- At the shot-liquid interface.
- At shrinkage cavities.
- At interfaces developed during freezing or subsequent heat treatment. For example, see the SD weld made by Langford and Cunningham[1].

Depending on where the fracture actually starts, the parameters that need to be more carefully controlled to get a sound casting can be isolated. The relative effectiveness of various ways that can be used to reduce and distribute the porosity more uniformly will be studied in these experiments.

4. Effect of Alloying Elements

Alloying elements for increased hardenability, strength, or toughness of a casting can be added or altered in four ways:

- Shot (low C), melt (C + alloying element)

- Shot (alloying element + low C), melt (plain C).
- Alloying elements in both shot and melt.
- Surface or volume treatment of the shot during/after manufacture of the shot.

Using shot of different compositions, a casting with varying alloy contents and hence different properties in different areas can be made easily. This is important, since highly alloyed shot need only be used in the critical parts of a casting, the rest being cheaper plain C shot.

It is important to know how the common alloying elements like Cr, Mo, Mn, Si, etc. behave when they are present in the melt because:

- Alloying elements affect the activity of C in the melt.
- Segregation of alloying elements in the solidified melt needs to be known, since alloying controls the attainable hardenability and other properties.
- If homogenization with respect to these alloying elements is to be accomplished (since homogenization times will increase drastically with the scale of segregation), the size of the shot will play an important role.

Segregation of these alloying elements might be an advantage. Substitutional alloying elements usually segregate strongly, and a suitable one which is a strong carbide former can be chosen so that the area around the last solidifying melt where shrinkage cavity occurs could be strengthened preferentially. This will be important if pores are the regions where fracture originates. An inversely segregating alloying element could make the area around the pore more ductile than the rest of the matrix. Combinations of elements can have opposing

effects; for example, Si and Mn respectively increase and decrease the activity of C in austenite so that the correct ratio of Si to Mn prevents carbon microsegregation due to the microsegregation of Si and Mn in conventional castings. Surface or volume treatment of the shot can have important effects; SSVCD greatly improves the utility of castings made from heavily oxidized (i.e., cheap) shot,[1] high carbon (i.e., cheap) shot can be decarburized after manufacture (see Section III), or the shot could be chemically treated during the atomization process (where the melt has a large relative surface area for rapid mass transport), for example by preferentially oxidizing an element (like Si, Cr, V, or Nb) to form a surface oxide on each droplet subsequently to be removed, protecting the immediate surface of the shot.

5. Large Size Castings

After the above mentioned experiments have been carried out successfully a suitable alloy composition and casting practice for the commercial size SD casting will be proposed. Different heat treatment temperatures and time will be used to find the best resulting mechanical properties like yield strength, fatigue behavior, ductile to brittle transition temperatures.

References

1. G. Langford and R. E. Cunningham, Met. Trans. B, 1978, vol. 9B, p. 5.

V.E. APPLICATION OF SD CASTING TO SPECIFIC ALLOYS

G. Langford
D. Apelian

V.E. Application of SD Casting to Specific Alloys

There are many types of steel which could be made by SD casting; however, the economics and quality of such castings will actually be made by SD casting. Therefore, SD casting will first be applied where the economics or quality forces are strongest.

The bulk of the present work in this ARPA program will be concentrated on two very broad areas (plain high carbon and low carbon steels) which cover steels for massive dies and the entire category of high strength low alloy steels. Some alloying elements will be used to study the physical and mechanical metallurgy of hardenable and solid-solution strengthened steels (as already discussed in Section V.D.).

However, two additional specific alloy systems show great promise for early application of rapid cycle steel casting technology. These are:

- Ultra high carbon high speed steel made by liquid infiltration[1].
- Aluminum-lithium SD casting.

The first offers a material-and energy-saving way of making higher quality high speed steel pieces cast to near net shape. High speed steels made from atomized high speed steel shot and eutectic-composition "high speed" steel liquid have ultra high carbon content and can be hardened from much lower austenitization temperatures than conventional high speed steel (1050°C vs. 1250°C). They are sufficiently shock resistant to be compared better with wrought high speed steels than cast ones.

The second area ventures away from steel metallurgy and the extremely favorable kinetics of the diffusion of interstitial carbon in face centered cubic austenite. Ordinarily, substitutional alloy systems have such low diffusivities that sintering of the necessarily much finer low-alloy solid shot[2] may take place before the shot can be successfully infiltrated by

high-alloy liquid. However, the aluminum-lithium system is probably the best candidate of the substitutional systems because

- Aluminum is notoriously slow to sinter.
- Lithium is a much lighter element than aluminum and so should diffuse in aluminum much faster than aluminum.
- The system already shows great promise in commercial application because of the greater elastic stiffness provided by lithium.[3]

SD casting of Al-Li alloys would enable greater Li contents to be used, just as steel casting by SD produces higher-carbon steels (especially high speed steel as described above).

Proposals are being prepared in each of these areas to do additional work over and above the provision of samples of SD castings. If additional funding becomes available as a result, then the present work may perhaps find more timely application.

References

1. G. Langford, Materials Science and Eng., 1977, vol. 28, p. 275.
2. G. Langford and R. E. Cunningham, Met. Trans. B., 1978, vol. 9B, p. 5.
3. T. H. Sanders and E. S. Balmouth, Metal Progress, March 1978, p. 32.